Studying Coherence in Ultra-Cold Atomic Gases

by

Daniel E. Miller

Submitted to the Department of Physics
in partial fulfillment of the requirements for the degree of

Doctor of Philosophy

at the

MASSACHUSETTS INSTITUTE OF TECHNOLOGY

August 2006

Author .....
Department of Physics
August 10, 2007

Certified by .....
Wolfgang Ketterle
John D. MacArthur Professor of Physics
Thesis Supervisor

Accepted by .....
Thomas J. Greytak
Professor of Physics, Associate Department Head for Education

Studying Coherence in Ultra-Cold Atomic Gases

by

Daniel E. Miller

Submitted to the Department of Physics
on August 10, 2007, in partial fulfillment of the
requirements for the degree of
Doctor of Philosophy

Abstract

This thesis will discuss the study of coherence properties of ultra-cold atomic gases. The atomic systems investigated include a thermal cloud of atoms, a Bose-Einstein condensate and a fermion pair condensate. In each case, a different type of measurement is performed. However, all of the experiments share a common tool: an optical lattice which is used to probe these atomic gases.

In the first case, we use an auto-correlation technique to study the interference pattern produced by a gas of atoms, slightly above the Bose-Einstein condensate transition temperature. A moving optical lattice is used to split and recombine the single particle atomic wavefunction. Analogous to a Young's double slit experiment, we observe high contrast interference which is well described by the model which we develop. When we address only a velocity subset of the thermal sample, however, the contrast is enhanced and deviates from this model.

In a second experiment we measure the coherence of a diatomic molecular gas, as well as the atomic Bose-Einstein condensate from which it was created. We use Bragg spectroscopy, in which atoms exchange photons with a moving optical lattice, transferring momentum to the atoms. This process can reveal the velocity distribution of the sample as energy and momentum are conserved only for a specific velocity class. Based on this measurement, we find that the atomic coherence is transferred directly to the molecular gas. We also discuss similar preliminary measurements performed on a fermion pair condensate in the BEC-BCS crossover.

In a third experiment we study a fermion pair condensate into a 3D optical lattice. Such a system shares many similarities with electrons in solid materials which exhibit superconductivity, and can offer insight into mechanism which result in this behavior. We infer coherence from the sharp interference pattern observed in the expanding gas, after release.

Finally, we study the abrupt onset of dissipation observed in a fermion pair condensate, as a function of velocity, in a moving optical lattice. We equate this threshold with the Landau critical velocity, and take measurements throughout the BEC-BCS crossover. The critical velocity is found to be maximum near unitarity, where the loss mechanism is predicted to crossover from phonon-like excitations to pair breaking.

Thesis Supervisor: Wolfgang Ketterle
Title: John D. MacArthur Professor of Physics

to our future

Acknowledgments

It would be disingenuous of me to dedicate my thesis to any one person or group of people. One does not endeavor to spend five years in a dark lab out of love or friendship. Along the way, however, relationships endure and grow stronger. My wife Ariana deserves a great deal of credit for her patience as she has sacrificed the most for the production of this thesis. I look forward to a long life of paying her back.

It is difficult to spend time at MIT without developing a sincere appreciation for the opportunity of being a part of something truly exceptional. Many graduates will reflect upon the Institute as a place where they consistently faced the most challenging problems, were exposed to the most novel ideas and got to play with the most cutting edge toys. My most fond memories, however, will certainly be of the people I met here. MIT attracts the brightest people from all corners of the globe and all walks of life. More often than not, they are engaging and stimulating people at a truly human level, defying the stereotype that accompanies the fields of science and technology. But, even the weirdest of weirdos are fascinating to observe in their natural habitat.

I was welcomed into the New Lab by the tough love of Jamil Abo-Shaeer. The first time I slipped up, I was told that I was so wet behind the ears that it made him sick. He delivered the line with a straight face, but he was laughing all the way. Jamil was relentlessly inclusive, and his sense of humor and fun created bonds among coworkers who would have otherwise rarely spoken. I hope it is not presumptuous to think that he passed the torch on to me, and that I have honored him by doing more than just standing around, holding my torch. Aaron Leanhardt is a man who excepts no excuses. Whether he is working in the lab or catching a Hail Mary pass, he gets the job done while making it look effortless. Together, Aaron and Jamil defined the work hard play hard culture of the group.

In the New Lab we encountered all the joys and struggles of a family. It has been a real pleasure to have worked with Jit Kee Chin for so much of my time here. Our skills are perfect complements, which is to say that I have the machine shop and Google Earth under control, while she handles the rest. As a show of my appreciation, I have even spelled her name incorrectly, the way she likes it. Yingmei Liu has been a great person to know, and I will always heed her fashion advice when choosing the color of my hat. Widagdo Setiawan possesses an exceptional raw talent. He has been a real challenge to know, and I

don't mean that pejoratively. I am glad to have become acquainted with Christian Sanner, because otherwise I would have thought that he had nothing to say. In fact, quite the opposite is true. His curious insight into all matters stands in defiance of the anesthetic properties of our dark noisy lab. Aviv Keshet has a great sense of humor, even when the joke is on him. I'm glad I have not been able to corrupt his naïve idealism, if only because it is the source of so much amusement. I have not spent much time with the newly arrived Ed Su, but enough to tell that he will fit in well and contribute much.

Our lab has also been fortunate to include two adopted members. We sought out Claudiu Stan for his unrivaled expertise in design, and could not have refurbished our machine without him. Marko Cetina we found in the hallway, like a stray cat. When looking for an audience at 4 a.m. to discuss his most recent discovery, he knew he could always come scratching at out door. His fascination helped temper our tunnel vision.

Beyond the lab itself, our corridor has always felt like a community, which continues to grow with the addition of new research groups. Tom Pasquini was the first friend I made in the group. We met at our first group meeting together, and soon our acquaintance became closer than I had anticipated. I have enjoyed watching our lives follow parallel but distinct trajectories. When Gretchen Campbell graduated and left me her squalid desk, I was glad for the mess. She earned it. Gretchen had spent her graduate career cheerfully cleaning up after others. I would like to offer her eternal reassurance that whatever inconsequential email she is frantically hesitant to send, will not be construed as offensive, inappropriate, or otherwise detrimental to her career or friendships. Micah Boyd was the most reliable source of one-liners in the lab. Since his graduation, I have often found myself asking What Would Micah Say? with a smirk on my face.

Martin Zwierlein could have gone on to practically any university he wished. The advice I offered him, to stay at M.I.T., was of purely selfish motivation, and I hope he will not hold it against me. Andre Schirotzek and I appear to be at loggerheads when it comes to Middle East policy. However, we have been able to share a number of lighter interests from music to snowsports, as well as some laughs along the way. When I first heard Christian Schunck play the harp I wondered how such beautiful music could come from such a dark and brooding individual. All joking aside, Christian is truly one of the most uplifting people to be around, and I will always miss our romantic breakfasts together in Varenna. Yong-Il Shin has somehow managed to partake in the lab antics while maintaining complete dignity,

and our younger members will learn a great deal from him. I have appreciated Jae Choi's loyalty as a fan of Dan Miller and the Dan Millers. He may hold the distinction of being the only group member to have put on a significant quantity of weight since joining the group ... at least in the form of muscle. If I have succeeded in teaching Caleb Christiansen one thing, it to not believe a thing I say. Caleb, you have been a terrible officemate.

Sebastian Will was one of those few German diploma students who got away. It was our loss, as his gregarious personality was sure to energize any party. Peter Zarth returned to Germany as well. I am sure he is happier in a land which values good bread and is more permissive of nudity. Andrew Grier seems like such a nice guy, until he takes your legs out trying to pull some hot dog skiing maneuver. Jon Simon has demonstrated that he has what it takes when brought all the dignity of a frat party to my thesis defense.

Wolfgang Ketterle has been an inspiring advisor who has always been able to find the silver lining. Carol Breen has always kept our hallway well fed, and provided a sort of non-physicist oasis at numerous physics gatherings. David Pritchard is a fascinating individual who refuses to constrain his curiosity to matters of physics.

I have neither the time nor the space to thank everyone appropriately. Please accept my apologies and my appreciation.

Contents

List of Figures

Chapter 1

Introduction

Much of what attracted me to atomic physics resides in the the clarity with which ultra-cold atomic gases exemplify the quantum mechanical nature of matter. Matter-wave interference, for example, offers striking affirmation of the precepts with which we first became acquainted in the classroom. The degree to which these systems are amenable to fairly simple theoretical description is encouraging to the experimentalist. The Bose-Einstein condensate behaves very much like a single particle wave-packet. The interaction of an atom with light is well modeled by the two level system. Verifying one's own calculation in the laboratory is an empowering experience, and a frequent one in the field of atomic physics.

When I first joined this group, Bose-Einstein condensates dominated the research agenda. A reliable and robust superfluid, this state of matter came to symbolize the precision and control which are characteristic of this field. Throughout my graduate career, however, the study of degenerate Fermi gases has been in the ascendency. These systems provided a new perspective on phenomena which have puzzled physicists for decades. Our understanding of strongly correlated electron systems stands to benefit from our study of atomic Fermi gases, which exhibit the same physics but offer numerous degrees of freedom unavailable in solid state materials. While anti-ferromagnetism and d-wave superfluidity currently lie at the periphery of our comprehension, atomic physics is well poised to shed light on these phenomena.

The properties of ultra-cold gases which most interest us all rely on coherence. Coherence is, in some sense, a measure of how a group of atoms will act in a coordi-

nated fashion, so as to exhibit a number of elegant wave-like properties. By studying coherence and its breakdown we gain further insight into the mechanisms at work and the limits of their applicability. In this thesis I will discuss a number of experiments, all of which have sought to probe the coherence properties of an atomic gas, in one way or another.

Chapter 2

Quantum Degenerate Gases

Introduction

In this chapter, we discuss the properties of quantum degenerate gases. The statistics of identical particles differentiates a quantum gas from its classical counterpart. This distinction is only meaningful when the gas approaches degeneracy, which is to say at low temperatures and high densities where the occupation probability of the lowest lying quantum states approaches unity. A number of good review articles [66, 29, 44] and textbooks [70, 91, 13] can be found which thoroughly cover the basics of quantum gases. Here, we will cover the most relevant concepts.

Identical Particles

The difference between bosons and fermions arises from a distinction in their symmetry. The wavefunction describing a collection of identical bosons is symmetric under the exchange of any two particles, and anti-symmetric in the case of fermions. The consequences of this subtlety are significant enough that these two types of particle must be treated as entirely different entities at low temperatures.

The Pauli exclusion principle follows from the anti-symmetry of fermions under exchange. Two identical fermions can not occupy the same state. Our earliest exposure to this rule comes in high-school chemistry class, when we learn how electrons fill up energy levels in an atom, producing the periodic table of the elements.

Bosons, on the other hand, can occupy the same state. In fact, a great deal of effort has been expended in order to make them do so, by the tens of millions at a time, in the

form of a Bose-Einstein condensate (BEC). A BEC is often described, colloquially, as a *giant matter-wave*. In fact, BECs exhibit a number of striking wave-like phenomena which exemplify what it means to be quantum mechanical. In addition, weakly interacting alkali BECs are amenable to fairly simple theoretical treatment, bearing much resemblance to the single particle wavefunction of an introductory quantum mechanics course. This has made the BEC an exciting and popular object of study over the past 12 or so years [4].

The atomic bosons which we condense are, just as all mass carrying bosons are [48], composite bosons: a bound state of an even number of fermionic subatomic particles. Similarly, we can create composite bosons, molecules for example, out of two fermionic atoms. Recently, quite a bit of excitement within the atomic physics community has been directed towards the so-called BEC-BCS crossover: the continuous transition between the physics of atomic fermions and diatomic bosons, which is achieved through the magnetic tuning of interactions. We will elaborate on this phenomena in Section 2.4. Suffice it to say that the union of two previously distinct physical regimes has been warmly received.

2.1 Bosons

Generally, the physics of many particles is far more complicated than that of the single or two interacting particles. This is why in thermodynamics we look at bulk properties rather than keep track of every particle. In many-body physics, interactions between particles create correlations which require some fairly sophisticated mathematics to keep track of [88, 118]. In contrast to liquid ^{4}He, Bose-Einstein condensates of alkali gases are extremely dilute, and the interactions are extremely weak. This allows us to make a number of approximations which greatly simplify the theoretical treatment.

2.1.1 s-wave Interactions

The interatomic potential is in general fairly complicated. Much of the detail, however, can be swept under the rug at the low temperatures which we achieve. The two-body collision process can be described in terms of *partial waves* [99, 25]. In short, the relative motion of the two particles is treated as a plane wave incident on some scattering potential. The scattering off this potential can be expressed in partial wave components (s-wave, p-wave, d-wave ...) which reflect a decomposition of the angular distribution into spherical harmonics. In the limit of zero relative velocity, which we approach at ultracold temperatures, only the lowest order s-wave component contributes, which is spherically symmetric. In other words, at very long wavelengths, the incident plane wave can't resolve any of the structure of the scattering potential.

The long and the short of it is that we treat the interaction as a delta function pseudo-potential

$$V(\vec{r}_1, \vec{r}_2) = \frac{4\pi\hbar^2 a}{m}\,\delta(\vec{r}_1 - \vec{r}_2) \tag{2.1}$$

which is parameterized by a single quantity, the *s-wave scattering length* a. This assumption is valid as long as a remains less than the average inter-particle spacing. The sign of a corresponds to the nature of the interaction; a is positive for repulsive interactions and negative for attractive interactions.

Symmetry of interactions

It should be noted that identical fermions can not experience s-wave scattering. As we discussed earlier, the fermionic wavefunction must have odd symmetry, which means only

odd partial waves (p,f,...) can be involved. This has serious implications in the field of ultra-cold gases, in which collisions are required for the cooling process. Identical fermions essentially do not collide at low temperatures, meaning we must either use a mixture of spin states or cool them sympathetically through interactions with another species, such as ^{23}Na. Similarly, bosons only experience scattering with even symmetry (s,d,...).

2.1.2 Gross-Pitaevskii Equation

The aim of *mean-field theory* is to replace all the interactions amongst a group of particles with an average or effective interaction, thus reducing a many-body problem into an effective one-body problem. Adopting the pseudo-potential of Equation 2.1, the condensate wavefunction can be described by a nonlinear Schrödinger equation, known as the Gross-Pitaevskii equation (GP equation)

$$\left[-\frac{\hbar^2}{2m}\nabla^2 + V_{ext}(\vec{r}) + \frac{4\pi\hbar^2 a}{m}\,|\psi(\vec{r})|^2\right]\psi(\vec{r}) = \mu\,\psi(\vec{r}), \tag{2.2}$$

where the chemical potential $\mu = \frac{4\pi\hbar^2 a}{m}\,n_0$, can be expressed as the interaction energy at the peak density n_0.

2.1.3 Thomas-Fermi Approximation

For a BEC, we can usually neglect the kinetic energy term in Equation 2.2, with respect to the interaction energy $U_{int} = 4\pi\hbar^2 na/m$. It then follows that a BEC in a harmonic trap has the characteristic parabolic density profile.

$$n(\vec{r}) = |\psi(\vec{r})|^2 = \frac{m}{4\pi\hbar^2 a}\,\left(\mu - V_{ext}(\vec{r})\right) \tag{2.3}$$

This approximation, however, fails at the very edges of the cloud, as the density approaches zero.

2.1.4 Healing Length

Spatial variations in the density of size ξ carry a cost in kinetic energy $\hbar^2/2m\,\xi^2$. Equating this energy with the interaction energy, we arrive at the natural length scale associated with

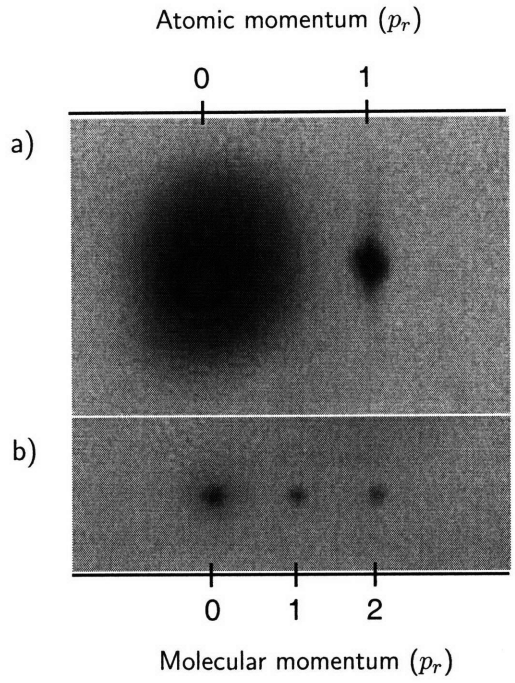

Figure 2-1: Matter-wave Sum Frequency Generation: just one example of the many phenomena which arise due to a nonlinear wave equation and which have direct analogs in nonlinear optics. a) Atoms are prepared in momentum states $|0\rangle$ and $|1\rangle$ using Bragg diffraction. b) The atom-molecule coupling produces molecules with momentum $|0\rangle$, $|1\rangle$ and $|2\rangle$, analogous to optical sum frequency generation. The time of flight is 17 ms.

U_{int}.

$$\xi = \frac{1}{\sqrt{8\pi n a}} \tag{2.4}$$

ξ is referred to as the *healing length.* It sets the distance, for example, over which the condensate density can change from its bulk value to zero, or equivalently, the size of a vortex core.

2.1.5 A nonlinear wave equation

Equation 2.2 is a nonlinear wave equation. As a consequence, we can describe a number of BEC phenomena in a manner completely analogous to that of nonlinear optics [76]. The mean field interaction acts as a third order nonlinear susceptibility $\chi^{(3)}$, which can drive processes such as four-wave mixing [33], soliton generation [34] and optical parametric generation [17]. The coupling to the molecular channel, which we describe in Section 2.3, is analogous to frequency doubling. In our lab [1], we demonstrated the sum frequency generation of matter waves by combining atoms with different momentum (and therefore, wavelength $\lambda = h/p$) into diatomic molecules, as shown in Figure 2-1.

2.1.6 Bogoliubov Excitation Spectrum

N. N. Bogoliubov first derived the spectrum of elementary excitations for a BEC [11]. Rather than elaborating upon the derivation, I will simply state the main result. The dispersion relation for elementary excitations is given by

$$E_p = \sqrt{\frac{p^2}{2m}\left(\frac{p^2}{2m} + 2mc^2\right)} \tag{2.5}$$

where the speed of sound c is given by the relation

$$mc^2 = \mu = \frac{\hbar^2}{2m\xi^2}\,. \tag{2.6}$$

We can identify two regimes of the spectrum, as illustrated in Figure 2-2. At low momentum, the excitations are sound-like, with linear dispersion $E_p \simeq pc$. At high momentum the excitations become free particle-like, where $E_p \simeq \frac{p^2}{2m} + \mu$. In addition to the kinetic energy, this excitation requires that we *pay* the chemical potential μ to kick an atom out of the condensate. This is a consequence of exchange symmetry: a distinguishable (ther-

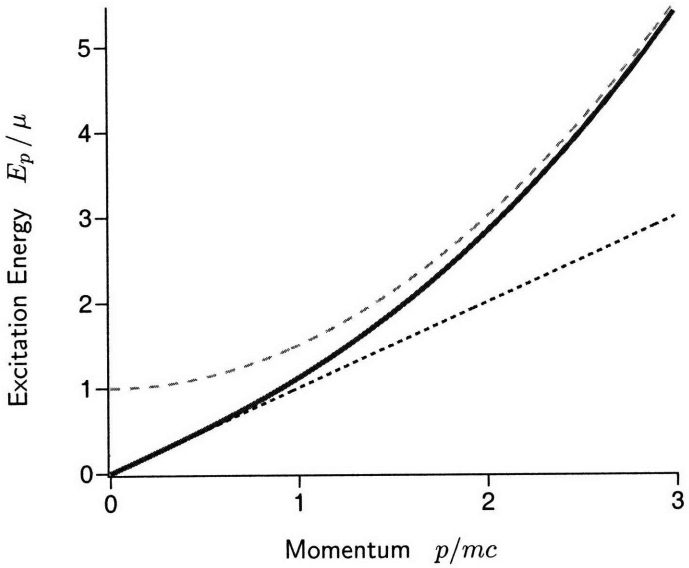

Figure 2-2: The Bogoliubov excitation spectrum (solid line). The elementary excitations of a BEC are phonon-like as low momentum, following a linear dispersion relation (dotted line). At high momentum, the excitations are free particle like. The excitation energy reflects the quadratic kinetic energy, offset by the mean field shift μ (dashed line).

mal) particle interacts with the condensate with twice the strength of an indistinguishable (condensate) atom.

The transition between these two regimes happens where the wavelength of the excitation $\lambda = h/p$ is on the order of the healing length ξ. In other words, the condensate can not support collective modes with a spatial variation λ shorter than the healing length.

2.2 The Non-interacting Fermi Gas

In the case of a degenerate Bose gas, we were primarily concerned with nature of the ground state, since we could pack an arbitrary number of particles into that state, in the form of a BEC. What concerns us most, in the case of a degenerate Fermi gas, is also the state of lowest energy to which we can add a particle. According to the Pauli exclusion principle, however, this state will sit on top of a filled *Fermi sea* of occupied energy levels. The energy of this state[1] is referred to as the Fermi energy E_F, and sets the energy scale for many properties of the system [7, 69]. We frequently work with harmonically trapped gases, for which the energies are quantized at the harmonic oscillator spacing. The Fermi energy for N non-interacting fermions[2] in a 3D harmonic oscillator is

$$E_F = h\bar{\nu}\,(6N)^{1/3} \tag{2.7}$$

where $\bar{\nu} = (\nu_x\,\nu_y\,\nu_z)^{1/3}$ is the geometric mean trapping frequency [15]. At zero temperature, the chemical potential μ is just the Fermi energy. Similarly, we can define the Fermi temperature $T_F = E_F/k_B$, which sets the relevant temperature scale of the system. A Fermi gas becomes quantum degenerate for temperatures $T/T_F \leq 1$, which is to say that at such temperatures states with energy below E_F begin to fill up, and the behavior deviates significantly from that of a classical gas.

2.2.1 The local density approximation

We can gain a fair amount of insight into the properties of a trapped degenerate Fermi gas by assuming that, locally, it behaves as a homogeneous gas. In other words, on a length scale short compared to the variation of the external potential, V_{ext} acts only as an offset. The local energy $\varepsilon(n)$ is determined by the sum of the kinetic and interaction energies, which depend only on the local density $n(\vec{r})$. The total energy is then

$$E = \int d\vec{r}\;[\,\varepsilon(n) + V_{ext}(\vec{r})\,n(\vec{r})\,] \tag{2.8}$$

[1] or equivalently, for large numbers, the energy of the highest occupied state, at zero temperature.

[2] The number N and density n in this thesis will always refer to the number of fermions in a single internal state. Many solid state textbooks, however, will refer to the total number, making the assumption of an unpolarized system of electrons, with two spin states. Be aware of this factor of 2.

This is known as the local density approximation (LDA), and is valid if the chemical potential is large compared to the quantization, that is, the harmonic oscillator spacing $\hbar\omega$ in the trap.

In a non-interacting Fermi gas, the local Fermi energy ε_F reflects only the local kinetic energy, through the local density of k-states. In other words, this is just the Fermi energy for a homogeneous gas of density n.

$$\varepsilon_F = \frac{\hbar^2}{2m}\left(6\pi^2 n\right)^{2/3} \tag{2.9}$$

In the same manner, we can define a local Fermi wavevector $k_F = (6\pi^2 n)^{1/3}$.

2.2.2 Density Profile

The chemical potential, $\mu = \varepsilon_F(r) + V(r)$, is of course flat across the sample. If it were not, the atoms would redistribute themselves. Wherever the potential is zero, which for a harmonic trap is at the trap center, we get $\varepsilon_F = \mu = E_F$. Inverting Equation 2.9 gives us the peak density

$$n_0 = \frac{1}{6\pi^2}\left(\frac{2m\mu}{\hbar^2}\right)^{3/2} . \tag{2.10}$$

The density profile is then

$$n(r) = n_0\left(1 - \frac{r^2}{R_F^2}\right)^{3/2} \tag{2.11}$$

where the Fermi radius is $R_F = \sqrt{\frac{2\mu}{m\omega^2}}$.

2.3 The Feshbach Resonance

One of the developments which has fueled the recent progress in the field of degenerate Fermi gases has been the identification and manipulation of Feshbach resonances [59]. Colloquially, a Feshbach resonance is a *magic knob* which allows us to tune the scattering length, and thus the interactions, of an atomic gas. More physically, it is a scattering resonance [99] which occurs when the state of two free colliding particles is degenerate with a bound state (see Figure 2-3). There is some coupling between states, from the hyperfine interaction, for example. If the states have different magnetic moments, we can tune their energies relative to one another with an externally applied magnetic field. The s-wave scattering length then

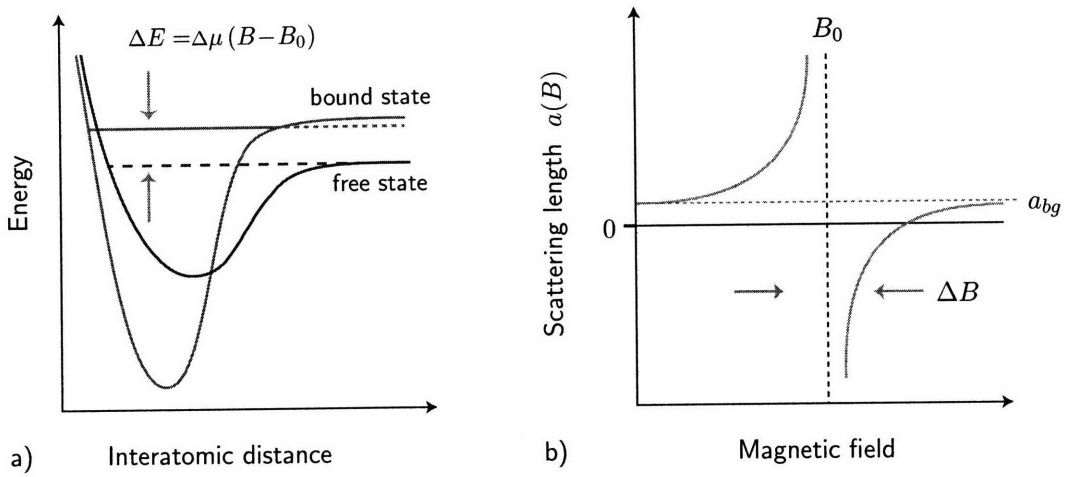

Figure 2-3: The Feshbach resonance. a) Interatomic potentials for different spin configurations have a difference in magnetic moment $\Delta\mu$, and thus tune differently with magnetic field. A free atomic state (red line) becomes degenerate with a bound molecular state (blue line) at a magnetic field B_0. b) Due to a coupling between these two states, two-body scattering is resonantly enhanced near this field. The s-wave scattering length a diverges on resonance, and can be tuned in both magnitude and sign in the region ΔB around resonance. The general form for $a(B)$ is found in Equation 2.12.

has the general magnetic field dependence

$$a(B) = a_{bg}\left(1 - \frac{\Delta B}{B - B_0}\right) \tag{2.12}$$

where a_{bg} is the background scattering length, B_0 is the location of the resonance, and ΔB its width.

This remarkable degree of control is limited only by our technical ability to regulate the magnetic field. Broad Feshbach resonances, such as in ^{6}Li [8], are more forgiving with respect to field stability. On the other hand, narrow resonances, such as those in ^{40}K [77] and ^{23}Na [106], make it easy to quickly jump around the resonance.

A Feshbach resonance allows one to vary not only the strength of interactions, but the sign as well. Studies with bosons are usually performed with repulsive ($a > 0$) interactions. A trapped BEC with attractive interactions is stable only at very small numbers. Above a critical density, the attractive interaction overpowers the repulsion due to finite size kinetic energy. Nevertheless, there are interesting aspects of such instabilities [43, 22]. Attractive interactions, however, are more interesting in the case of fermions, as they give rise to BCS physics, which we will discuss in Section 2.4.1.

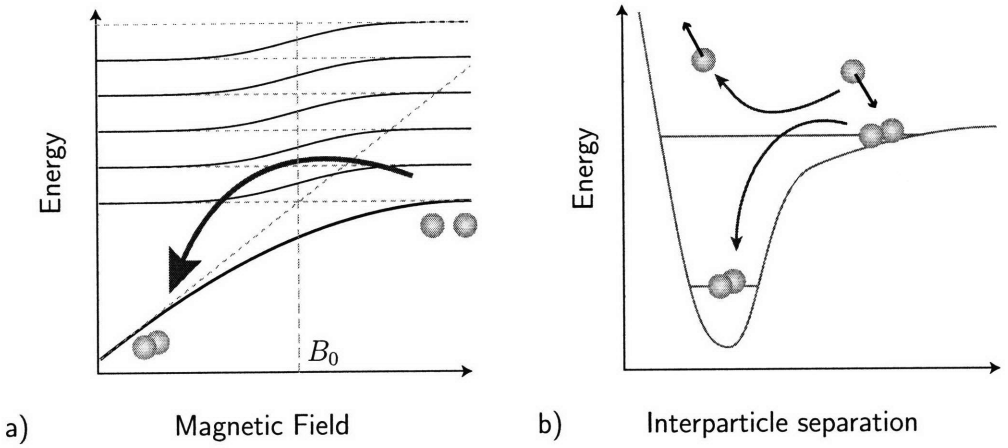

Figure 2-4: Feshbach Molecules. a) The atom-molecule coupling near a Feshbach resonance creates an avoided crossing between the free atom continuum and a bound molecular state. Atoms can be adiabatically converted to molecules by sweeping the magnetic field across the resonance. b) Three body collisions can transfer weakly bound molecules into a more deeply bound state, while a third body carries of the difference in binding energy as kinetic energy.

While the s-wave resonances for ^{40}K and ^{6}Li, in particular, have been the workhorses of the field, there are other more exotic Feshbach resonances. Ordinarily, ultra-cold identical fermions do interact, since s-wave collisions are disallowed by symmetry and other partial waves are frozen out. However, p-wave resonances have been found [100, 94] which allow one to circumvent this "rule". Feshbach resonances between different atomic species have also been identified [104, 60, 40]. And, while we usually associate Feshbach resonances with magnetic tunability, the Innsbruck group has induced a Feshbach resonance optically [110].

2.3.1 Feshbach Molecules

As we mentioned, a Feshbach resonance involves the coupling of the free atomic state to a molecular bound state. This coupling is coherent, as evidenced by the atom-molecule oscillations [36] it can produce. It also gives rise to an avoided crossing, which allows for the adiabatic conversion of atoms into molecules, as depicted in Figure 2-4a. Basic scattering theory [99] tells us that a bound state exists for $a > 0$, and the binding energy is

$$E_b = -\frac{\hbar^2}{2m_r\, a^2}\ , \tag{2.13}$$

where m_r is the reduced mass of the system, which is just half the atomic mass, in the case of a homonuclear molecule.

Our lab was one of the first to produce diatomic molecules from a BEC, by sweeping across a Feshbach resonance. This technique has been implemented in the production of "bosonic" dimers[3] of several species, including $^{133}Cs_2$ [54], $^{87}Rb_2$ [38] and $^{23}Na_2$ [116]. These bosonic dimers, however, have been of limited utility so far. While the binding energy of this molecular state is very small, the overlap (Frank-Condon factor) with more deeply bound states is significantly greater than that of two free atoms. As a consequence, three-body collisions, as illustrated in Figure 2-4b, occurs at a prohibitively high rate, limiting the lifetimes of these samples to tens of milliseconds. Although Bragg spectroscopy has shown that these dimers can be created with very high phase-space density [1], these samples do not have enough time to thermalize, and thus can not be considered a BEC.

Fermions, however, do not suffer the same fate. The Pauli exclusion principle suppresses three-body recombination, allowing "fermionic" dimers such as $^{40}K_2$ [95] and $^{6}Li_2$ [27, 63, 108] not only to Bose-Einstein condense [47, 64, 120], but to survive in this state for tens of seconds. These long lived molecular BECs are most exciting, however, in the context of the BEC-BCS crossover, which we discuss in Section 2.4.1.

2.4 The Strongly Interacting Fermi Gas

In Section 2.2, we discussed the physics of non-interacting fermions. This was not as idealized as it may sound, since identical fermions at low temperatures simply do not interact. It was, however, rather boring. Most of the exciting physics comes from the interactions. In order to add interactions to our Fermi gas we incorporate more than one spin state. This spin mixture, however, must be an incoherent mixture. Fermions in the same coherent superposition of spin states are still identical [122]. Fortunately, decoherence is easy to come by.

Nevertheless, with two spin states, fermions can collide in s-wave. The two-particle wave function must, of course, remain anti-symmetric under exchange. This just means that the spin component of the wavefunction will be in the singlet configuration.

[3] bosonic here refers to the constituent atoms. All homonuclear dimers are bosons, whether they are formed from bosons or fermions.

2.4.1 The BEC-BCS Crossover

As we discussed in Section 2.3, a Feshbach resonance allows one to control not only the strength of interactions, but the sign as well. This has some profound ramifications for a two-component Fermi gas. Until quite recently, two distinct types of superfluidity have existed in separate, almost parallel worlds. On the one hand there are bosons, such as ^{4}He, which for repulsive interactions ($a > 0$) can form a BEC, which exhibits superfluid properties. On the other hand, there are fermions, such as ^{3}He and electrons, which at very low temperatures (T/T_F) and in the presence of attractive interactions ($a < 0$), form Cooper pairs and can be described by the superfluid BCS state. The atomic Feshbach resonance acts as a bridge between these two regimes. The nature of the interactions can be continuously tuned from repulsive, on the BEC-side of the resonance, to attractive, on the BCS-side. The region in between is known as the BEC-BCS crossover, and has been the subject of intense theoretical and experimental research lately [44].

2.4.2 Unitarity

The divergence in Equation 2.12 seems to imply that interactions can be made arbitrarily large in magnitude, but the s-wave scattering length does not tell the whole story. The scattering cross section σ is given by

$$\sigma = \frac{4\pi^2 a^2}{1 + k^2 a^2} \tag{2.14}$$

where the wavevector k of the relative motion is typically given by the local Fermi wavevector k_F.

In the typical case for dilute atomic gases, $a \ll 1/k_F$, and we get the intuitive result that $\sigma \simeq 4\pi^2 a^2$. The atoms look like hard spheres of radius a. For strong interactions $a \gg 1/k_F$, however, the cross section has a different limiting behavior.

$$\lim_{a \to \pm\infty} \sigma = \frac{4\pi^2}{k_F^2} \tag{2.15}$$

In other words, the effective scattering length is cut off at the mean interparticle spacing $n^{-1/3}$, which, by no coincidence, is the inverse Fermi wavevector $1/k_F$.

The region for which $|k_F a| > 1$ is usually referred to as the strongly interacting, or

unitarity, regime. It is interesting to note that, in this limit, the collisional behavior does not depend on either the magnitude or the sign of the scattering length.

2.4.3 Universality

It turns out we can incorporate interactions into the non-interacting equation of state (Section 2.2) without much difficulty. As a consequence of unitarity limited interactions, length scales other than $1/k_F$ fall out of the picture. The interaction energy can only by given by the local Fermi energy ε_F, times some constant β. So, we can write the local[4] chemical potential μ_{loc} as

$$\begin{aligned} \mu_{loc} &= \varepsilon_F + U_{int} \\ &= (1+\beta)\ \varepsilon_F \\ &= (1+\beta)\ \frac{\hbar^2}{2m}\left(6\pi^2 n\right)^{2/3} . \end{aligned} \tag{2.16}$$

The behavior becomes *universal* in the sense that specific details of the atomic potential are no longer relevant [55]. The value of the universal parameter β has been of great theoretical and experimental interest [44]. A number of measurements and calculations are consistent with $\beta \simeq -0.58$. The fact that β is negative indicates that universal interactions are intrinsically attractive.

Since the inclusion of unitarity limited interactions has not changed the functional form of equation of state ($\mu_{loc} \propto n^{2/3}$), we expect the shape of a zero-temperature trapped Fermi gas at unitarity to be the same as that of a non-interacting gas (Equation 2.11). The overall size R and peak density n_p, however, will change in response to the interactions. In a harmonic trap, $R \propto \mu^{1/2}$. Including interactions we find $R_{int} \propto \sqrt{1+\beta}\, n_p^{1/3}$, according to Equation 2.16. The product $n \times R^3$ remains invariant under the inclusion of interactions. This simply reflects conservation of number. This allows us to express the peak density n_p of a harmonically trapped Fermi gas with universal interactions in terms of that of a non-interacting Fermi Gas n_0.

$$n_p = (1+\beta)^{-3/4}\ n_o \tag{2.17}$$

[4]The global chemical potential is the sum of the local chemical potential and the external potential $\mu = \mu_{loc}(r) + V_{ext}(r)$

Equivalently, the size of the interacting gas becomes

$$R_{int} = (1+\beta)^{1/4}\, R_F\,. \tag{2.18}$$

Given the peak density, we can express the local Fermi energy ε_F at the trap center in terms of the non-interacting Fermi energy E_F.

$$\varepsilon_F\Big|_{r=0} = (1+\beta)^{-1/2}\, E_F \tag{2.19}$$

Effective Mass

There is another route to understanding the effect of universal interactions on the size and density of a trapped Fermi gas [49]. We can interpret the interactions as providing an effective mass m^*,

$$m^* = \frac{m}{1+\beta} \tag{2.20}$$

which, in turn, scales the trap frequency to $\omega_{eff} = \sqrt{1+\beta}\,\omega$. The global chemical potential, still given by the Fermi energy, becomes

$$\mu = \hbar\bar{\omega}_{eff}\,(6N)^{1/3} = \sqrt{1+\beta}\,E_F\,, \tag{2.21}$$

from which Equations 2.17 and 2.18 follow.

Personally, I find this approach unappealing, as it is not immediately obvious where m^* is applicable. For example, the dipolar oscillation frequencies are **not** rescaled by $\sqrt{m/m^*}$, even though we have defined an effective trap frequency ω_{eff} for the purpose of rescaling the Fermi energy. The effective mass for an optical lattice (Equation 3.25), in contrast, is more consistent in its applicability, and does in fact modify the oscillation frequency [74, 39].

Chapter 3

Optical forces and lattices

3.1 The optical dipole force

In this section we will discuss the energy shift produced by an off-resonant light field, known as the AC-Stark effect, and the optical dipole force which results when this shift has spatial dependence. We will use a classical description in order to establish intuition, followed by a quantum mechanical treatment.

3.1.1 A classical dipole

An atom in an electric field will acquire an induced a dipole moment, as the electron cloud is pulled in one direction and the nucleus in another. The energy of a dipole in an external electric field is $E = -\vec{\mu_e} \cdot \vec{\mathcal{E}}$. It follows that if the field is non-uniform, a dipole which is aligned with the field will get pulled into the region of stronger $\mathcal{E}$ field. In the case of an A.C. electric field, such as a light wave, the atomic dipole responds as a driven harmonic oscillator. The dipole has a natural oscillation frequency ω_0, and is damped, as an oscillating dipole will radiate, scattering photons. We know that the phase of such an oscillator, with respect to the drive field, varies with frequency [80]. Far below resonance, in the case of *red detuning*, the dipole can follow the field oscillation. The atom will then be pulled into regions of higher intensity. If the light is far *blue detuned*, the dipole will be π out of phase, and thus antiparallel to the electric field. Atoms will then be repelled from intensity maxima.

3.1.2 The AC Stark shift

Quantum mechanically, of course, the internal states of an atom are discretized, and we can usually model the physics as a two-level problem. We consider a ground state $|g\rangle$ and an excited state $|e\rangle$, separated by an energy $\hbar\omega_0$. The light field $\vec{\mathcal{E}}(t) = \mathcal{E}_0 \cos\omega t\,\hat{\epsilon}$ introduces a coupling

$$W_{eg}(t) = \left\langle e \left| -\vec{\mu}\cdot\vec{\mathcal{E}}(t) \right| g \right\rangle = \frac{\hbar\Omega}{2}\left(e^{i\omega t} + e^{-i\omega t}\right) \tag{3.1}$$

where the Rabi frequency is

$$\Omega = -\frac{e\,\mathcal{E}_0}{\hbar}\,\langle e|\,\vec{r}\cdot\hat{\epsilon}\,|g\rangle \tag{3.2}$$

The polarization $\hat{\epsilon}$ of the light dictates which internal states can be coupled through selection rules.

The time dependence can be eliminated by transforming to the appropriate rotating frame, and the Hamiltonian becomes

$$\tilde{H} = \frac{\hbar}{2}\begin{bmatrix} -\delta & \Omega \\ \Omega^* & \delta \end{bmatrix} \tag{3.3}$$

where we have introduced the *detuning* $\delta \equiv \omega - \omega_0$. The result of the coupling is that real eigenstates are some admixture of excited and ground state. The eigenenergies in this frame are

$$E_{e,g} = \mp\frac{\hbar}{2}\sqrt{\delta^2 + \Omega^2} \tag{3.4}$$

For $\Omega \ll |\delta|$, we can Taylor expand this, and we find that the coupling Ω shifts the energies.

$$\Delta E_{e,g} = \mp\frac{\hbar\Omega^2}{4\delta} \tag{3.5}$$

This is what we refer to as the AC Stark shift.

An intuitive way of looking at this system is to consider the atom plus the light field. If the atom is excited, it takes a photon of energy $\hbar\omega$ out of the field (see Figure 3-1). So the state $|g;\,n\rangle$ (i.e., atom in ground state and n photons in the laser field) is nearly degenerate with $|e;\,n-1\rangle$. We know from perturbation theory that coupled states repel, and this insight explains how the sign of the shift corresponds to the sign of δ.

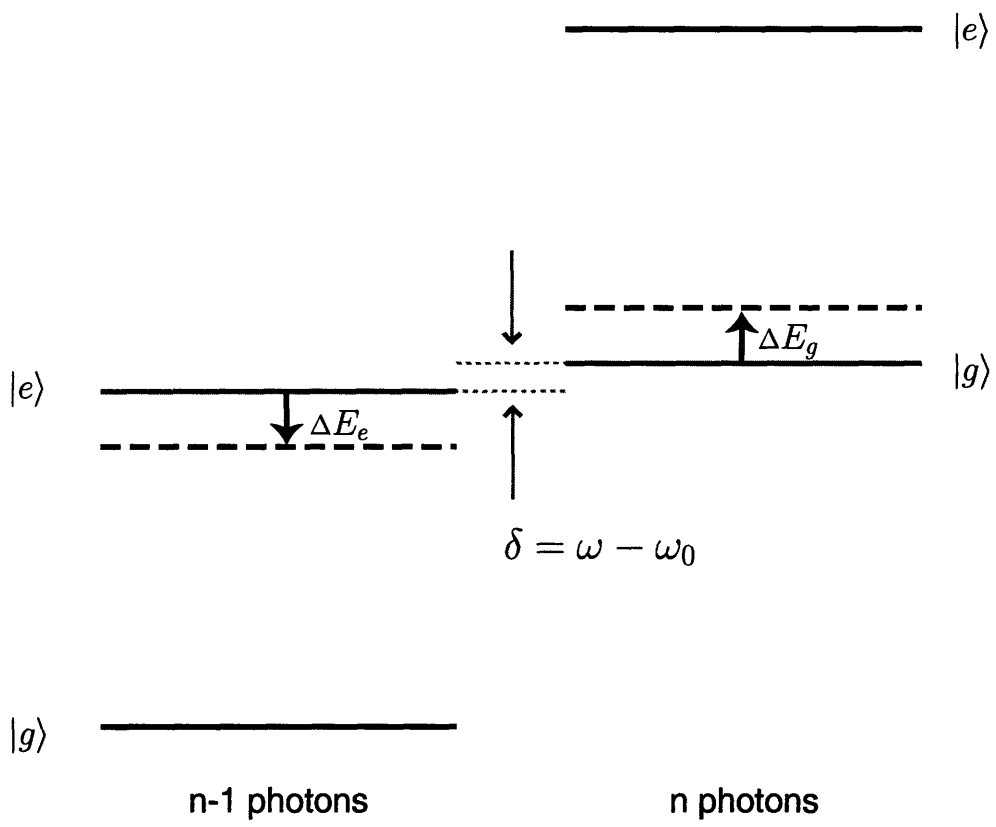

Figure 3-1: The AC Stark Shift. Energy level diagram for a photon plus two-level atom system. The bare atom has excited and ground states $\{|e\rangle, |g\rangle\}$ separated by an energy $\hbar\omega_0$. A light field of frequency ω couples the two states. Because the transition from the ground to excited state is accompanied by the removal of a photon with energy $\hbar\omega$, the two states are nearly degenerate. The coupling causes the states to repel, giving rise to the AC stark shift $\Delta E_{e,g}$ of Equation 3.6. The digram is shown for a blue-detuned light field ($\delta > 0$).

Perturbation Theory

In fact, we could have also used perturbation theory to solve for the AC Stark shift. The perturbation to the ground state energy is second order.

$$\Delta E^{(2)} = \frac{\hbar\Omega^2}{4}\left(\frac{1}{\omega-\omega_0}+\frac{1}{\omega+\omega_0}\right) \tag{3.6}$$

$$= \frac{\hbar\Omega^2}{4\delta} + \underbrace{\frac{\hbar\Omega^2}{4(2\omega-\delta)}}_{\text{Bloch Siegert shift}} \tag{3.7}$$

This approach, however, gives us an additional term which we did not find in Equation 3.5. This term is referred to as the Bloch Siegert shift [9], and comes from the *counter rotating* term which we ignored in order to arrive at the simple Hamiltonian in Equation 3.3. This term is indeed significant for many of our applications in which we use a far-detuned laser, in the infrared, for example.

3.2 The optical dipole trap (ODT)

Given what we know about the AC stark shift, its pretty straightforward to calculate the trapping force produced by red detuned laser beam. A Gaussian laser beam of total power P focused down to a spot size[1] of w_0 has a peak intensity $I_0 = 2P/\pi w_0^2$. The intensity profile is given by

$$I(r,z) = \frac{2P}{\pi w^2(z)} e^{-2\left(\frac{r}{w(z)}\right)^2} \tag{3.8}$$

where the e^{-2} radius varies along the axis as $w(z) = w_0\sqrt{1+z^2/z_0^2}$. The Rayleigh range is defined as $z_0 = \pi w_0^2/\lambda$, where λ is the wavelength of the light. In an harmonic approximation, the potential $V(\vec{r})$ becomes

$$V(r,z) \simeq -V_0\left(1-2\left(\frac{r}{w_0}\right)^2-\left(\frac{z}{z_0}\right)^2\right) \tag{3.9}$$

where, according to Equation 3.6, the trap depth V_0 is given by

$$V_0 = \frac{\hbar\gamma_0^2}{8}\frac{I_0}{I_{sat}}\left(\frac{1}{\omega-\omega_0}+\frac{1}{\omega+\omega_0}\right) \tag{3.10}$$

[1]The beam waist is conventionally the e^{-1} radius of the $\mathcal{E}$ field, and thus the e^{-2} radius of the intensity.

	λ (nm)	$\gamma_0/2\pi$ (MHz)	I_{sat} (mW/cm^2)
^{6}Li	670.96	5.92	2.56
^{23}Na	589.16	10.01	6.40
^{40}K	766.70	6.09	1.77
^{87}Rb	780.24	5.98	1.64

Table 3.1: Transition wavelength λ, natural linewidth γ_0 and saturation intensity I_{sat} for some popular alkali atoms, from [82].

which we have expressed in terms of the natural linewidth γ_0 and the saturation intensity I_{sat}. We list these experimentally convenient parameters for some commonly used alkali atoms in Table 3.1. The resulting trap frequencies are

$$\omega_r = \sqrt{\frac{4\,V_0}{m\,w_0^2}}\,, \quad \omega_z = \sqrt{\frac{2\,V_0}{m\,z_0^2}} \tag{3.11}$$

The weakly bound diatomic molecules and BCS-type pairs we work with essentially have twice the polarizability of a single atom, and will experience twice the trap depth. They will, however, experience the same trap frequencies as the unpaired atoms, since they also have twice the mass. This is analogous to two identical pendulums which oscillate at the same frequency whether or not they are attached to each other.

Scattering

While the AC Stark shift ΔE can become very strong near resonance, one must then contend with the scattering of photons, which is generally counterproductive in a cold atom experiment. From the photon scattering rate

$$\Gamma_s = \frac{\gamma_0}{2}\,\frac{I/I_{sat}}{1 + I/I_{sat} + (2\delta/\gamma_0)^2} \tag{3.12}$$

we see that at large detuning, $\Gamma_s/\Delta E \sim \gamma_0/\delta$, for a given laser intensity. Therefore, we usually stand to gain by using far-detuned light, and compensating with more power. Infrared lasers at 1064 nm are readily available at sufficient powers, and induce negligible scattering.

3.3 Optical Lattices

In the previous sections, we discussed the interaction of light with an atom int the context of internal degrees of freedom. We neglected the atoms external degrees of freedom, that is to say its spatial wavefunction $\psi(\vec{r})$. The absorption of a photon, for example, must be accompanied by the absorption of that photon's momentum $\hbar k$. This is reflected in the the fact that a spatially varying phase acts as an operator, connecting different momentum states.

$$e^{ikz} = \sum_p |p\rangle\langle p + \hbar k| \tag{3.13}$$

Much of our understanding of atoms in a periodic potential derives from the more mature field of condensed matter physics, which describes the behavior of electrons under the influence of an ionic crystal lattice. However, as is often the case in quantum mechanics, there exist a multitude of ways to understand a particular phenomena. In this Chapter we discuss a number of frameworks, each which offers its own particular insight into optical lattice phenomena. The review paper, Ref. [85] can offer further illumination.

3.3.1 Two-Photon Transitions

The treatment of an atom interacting with two light fields is not any more complicated than that for a single light field, under certain conditions. Let us consider, for example, two counter propagating beams. The beams are derived from the same laser, so they have the same wavevector $\vec{k}_1 = -\vec{k}_2 = k\,\hat{z}$, although we may introduce some small frequency difference δ between them with, say, an AOM. Both beams couple the same internal states, $|g\rangle$ and $|e\rangle$, but different momentum states, since they face different directions. For clarity, we'll say that beam 1 couples the state $|g,p\rangle$ to the state $|e,p+\hbar k\rangle$, while beam 2 couples $|g,p\rangle$ to $|e,p-\hbar k\rangle$. If we constrain our attention to the dynamics of an atom initially in a single momentum state, say $p = 0$, we only need to consider a total of three states

$$\left\{ |g,\, p=0\rangle\,,\ |g,\, p=2\hbar k\rangle\,,\ |e,\, p=\hbar k\rangle \right\}$$

as depicted in Figure 3-2.

In fact, the situation is even more simple than that. What we have is a typical lambda system, in which two states are coupled though an intermediate state of higher energy. The

dynamics are well described by a Raman process in which one photon is simultaneously absorbed from one beam and another is stimulatedly emitted into the other beam. Our case differs slightly from the traditional Raman, in that we are changing momentum states rather then internal states, but that is a semantic distinction. If the beams are far detuned from the intermediate state ($|e, \hbar k\rangle$), it can be eliminated, and we are effectively left with a two-level system. In the appropriate rotating frame, the Hamiltonian becomes

$$H = \begin{bmatrix} \hbar\delta/2 & \hbar\frac{\Omega_1\Omega_2^*}{4\Delta} \\ \hbar\frac{\Omega_1^*\Omega_2}{4\Delta} & 4\frac{\hbar^2k^2}{2m} - \hbar\delta/2 \end{bmatrix} \tag{3.14}$$

where $\Omega_{1,2}$ is the Rabi frequency for beams 1 and 2, and $\Delta \sim \delta_1 \sim \delta_2$ is the single photon detuning. This looks just like the Hamiltonian from Equation 3.3, where $\Omega^{(2)} \equiv \frac{\Omega_1\Omega_2^*}{2\Delta}$ is the *two photon Rabi frequency*, and the effective detuning is

$$\delta_{eff} \equiv \delta - 4\frac{\hbar^2k^2}{2m} \tag{3.15}$$

This effective detuning reflects conservation of energy: the difference between the energies of the photon absorbed and emitted accounts for the change in the atom's kinetic energy.

3.3.2 Bragg Diffraction in the Two Photon picture

We can perform a coherent population transfer between two momentum states [72] by abruptly turning on the two coupling beams. This process is known as Bragg diffraction, in analogy with the scattering of x-rays off of crystals (upon which we will elaborate later in this Chapter). It is a resonant process which can achieve complete transfer when $\delta_{eff} = 0$. This is known as the Bragg condition

$$\hbar(\omega_1 - \omega_2) = \frac{q^2}{2m} + \vec{v}\cdot\vec{q} \tag{3.16}$$

which we have generalized[2] for beams of arbitrary pointing $\vec{k}_{1,2}$ which impart a momentum $\vec{q} = \hbar(\vec{k}_1 - \vec{k}_2)$, as well as an initial atomic velocity $\vec{v}$. Of course, one can always find a reference frame in which the atom is initially at rest, as in Figure 3-2a. Rather than representing kinetic energy, the $\vec{v}\cdot\vec{q}$ term in Equation 3.16 becomes the Doppler shift

[2]For continuity, we will continue to treat the case of counter-propagating beams ($|\vec{q}| = 2\hbar k$)

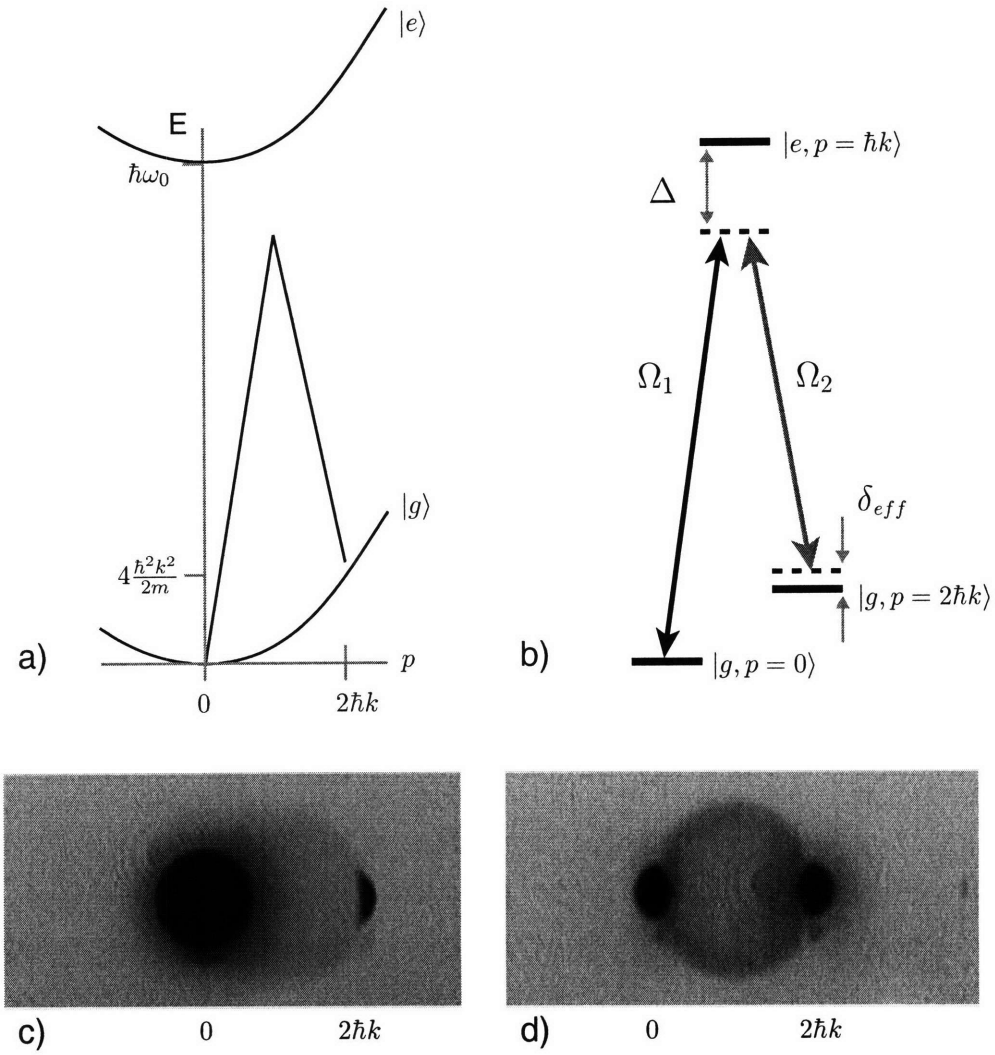

Figure 3-2: The two photon process. a) Energy vs momentum for the excited and ground states of an atom. A two photon process transfers momentum $2\hbar k$ to the atom. This process conserves energy when the two photon detuning is equal to the kinetic energy imparted to the atom. Diagram is not to scale ($\hbar\omega_0 \gg 4\frac{\hbar^2k^2}{2m}$). b) The same process drawn as a lambda system, showing the equivalence to a Raman transfer. c) Time of flight image of a Na BEC for which a small fraction of the population has been transferred. d) A BEC which has been divided equally into two momentum states by a $\pi/2$ Bragg pulse. A *scattering halo* results from collisions between momentum states as they spatially separate.

incurred in going to that frame.

The population of the two momentum states evolve as a Rabi oscillation, and can therefore be controlled by the duration of the Bragg pulse τ. We typically refer to the pulse duration in terms of its product with the Rabi frequency $\Omega^{(2)}\tau$. A π-pulse ($\Omega^{(2)}\tau = \pi$), for example, transfers the population completely. We emphasize that this is a coherent process. This language is also appealing in the Bloch sphere picture, where a π pulse corresponds to a rotation of the Bloch vector by 180°. A $\pi/2$ pulse puts each atom into an equal superposition of both momentum states. It is not until we make a measurement, such as taking the absorption image shown in Figure 3-2d, that this becomes a statistical distribution.

Two-Photon Linewidth

In our treatment of the two level atom of Chapter 3.1.2, we were able to ignore kinetic energy imparted to the atom from the photon. This *recoil energy*

$$E_r = \frac{\hbar^2 k^2}{2m} \tag{3.17}$$

is typically on the order of 10 khz (depending on the photon wavelength and atomic mass, of course). The natural linewidth γ_0 of an atomic transition is typically ~10 MHz (see Table 3.1), making the recoil rather insignificant. The linewidth of a two photon transition, however, is smaller by a factor of $\sim \Omega^{(2)}/\Delta$, since the occupation of the excited state is minuscule. Resolution on a scale small compared to the recoil energy is attainable. While these parameters can vary greatly, for one experiment [1], values of

$$\Omega^{(2)}/2\pi \sim \text{khz}$$

$$\Delta/2\pi \sim \text{thz} \qquad (\delta\lambda \sim 1nm)$$

were typical. This high resolution allows, for example, the detection of small shifts in the narrow velocity distribution of a BEC, which we will discuss further in Section 3.4.

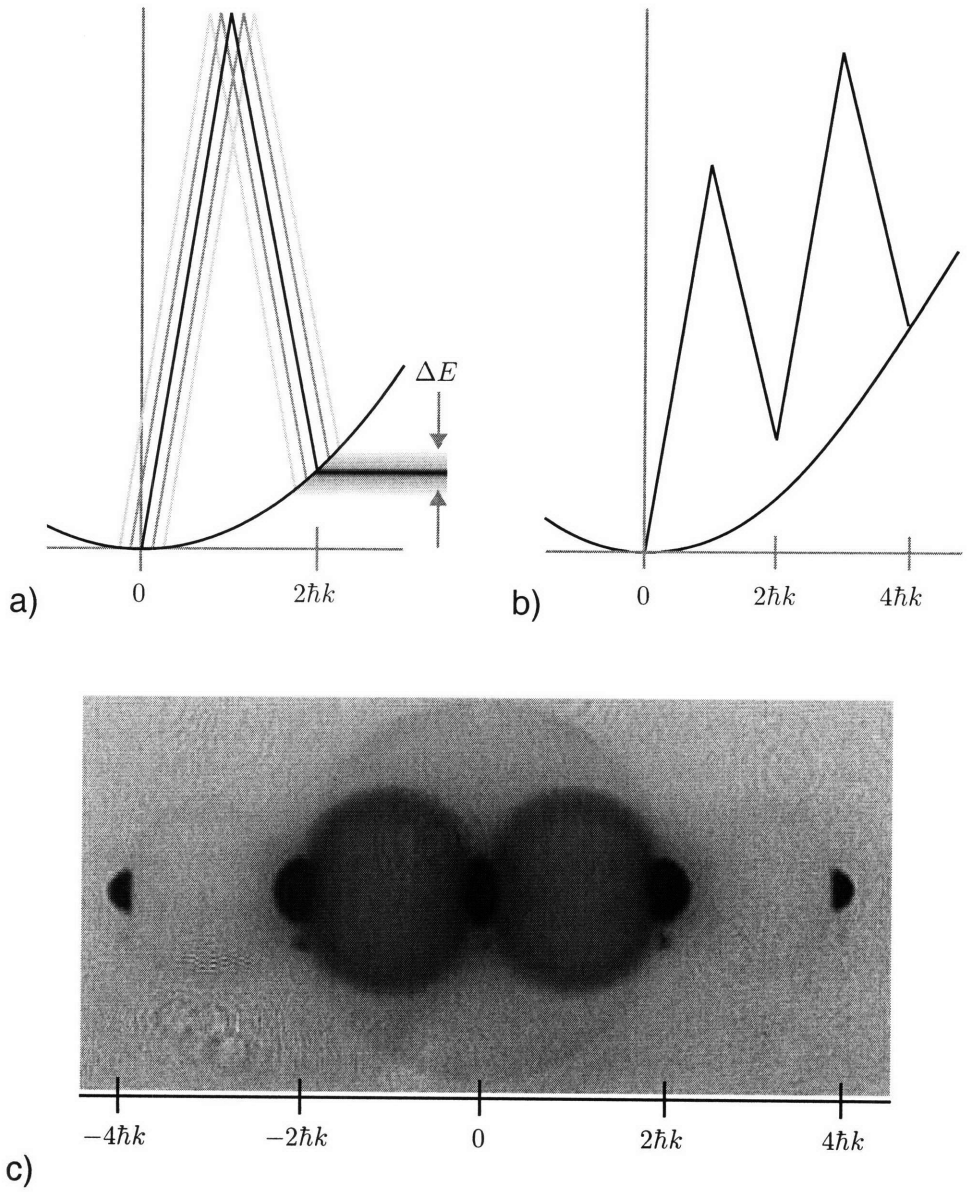

Figure 3-3: Kapitza-Dirac scattering. a) The two-photon Bragg process, which transfers a quantity $q = 2\hbar k$ of momentum to an atom can only conserve energy for a particular velocity class. This is the Bragg condition given by Equation 3.16. The finite duration Δt of the Bragg pulse implies an energy uncertainty ΔE in the two-photon process, through the Heisenberg relation. This allows a spread of initial velocities to be out-coupled. b) Higher order processes, such as this four-photon process, are possible. Because the dispersion relation is quadratic, the Bragg condition for a four-photon process is met for a different detuning $(\omega_1 - \omega_2)$ than that for a two-photon process. c) An absorption image of a BEC in expansion, which has been subjected to a Kapitza-Dirac pulse. For short enough pulse duration, the energy uncertainty can cover multiple Bragg processes. Multiple s-wave collision halos are visible.

Energy Uncertainty

The resolution of the Bragg process is effected by the finite duration of the Bragg pulse, through the energy time uncertainty relation. In other words, a Bragg pulse contains a spread of Fourier components. This has some obvious implications. The (single particle) dispersion relation is quadratic, therefore the Bragg condition (Equation 3.16) is satisfied for only one particular velocity class. This effect can be exploited as a way of measuring the velocity distribution of an atomic sample spectroscopically. Even a BEC has a velocity spread, due to its finite size, which can be resolved [107]. As Figure 3-3 illustrates, a shorter pulse with greater energy uncertainty can accommodate a larger spread of velocities.

Higher Order Processes

The same approach we took in eliminating the intermediate state of a two photon process can be built upon to describe higher order processes. Figure 3-3b shows, for example, a four photon process. The dynamics would evolve at a four photon Rabi frequency, and the Bragg condition must reflect the kinetic energy of transferring a momentum of $4\hbar k$.

3.3.3 Kapitza-Dirac Scattering

For very short Bragg pulses, the energy uncertainty can become large enough that the Bragg condition can be satisfied for multiple Bragg processes. This process is known as Kapitza-Dirac scattering, and takes place for

$$\tau \ll \frac{\hbar}{E_r} \tag{3.18}$$

Figure 3-3c illustrates the effect of a Kapitza-Dirac pulse on a BEC. For two beams of the same frequency ($\delta = 0$), a condensate initially at rest is distributed symmetrically amongst momentum states of integer values of $2\hbar k$.

3.3.4 A light grating

In this section we offer a complimentary picture of the interaction of an atom with two laser fields. Two intersecting laser beams will interfere to create a spatially modulated intensity profile, as illustrated in Figure 3-4. This interference pattern can be treated as a spatially

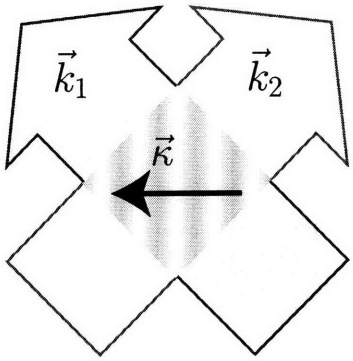

Figure 3-4: Laser beams with wavevectors $\vec{k}_1$ and $\vec{k}_2$ intersect to produce an interference pattern with wavevector $\vec{\kappa} = \vec{k}_1 - \vec{k}_2$.

varying AC Stark shift

$$V(\vec{r}) = 4\,V_0\,\cos^2\tfrac{1}{2}\,(\vec{\kappa}\cdot\vec{r} - \delta t) \tag{3.19}$$

where $\vec{\kappa} = \vec{k}_1 - \vec{k}_2$, and V_0 is the AC Stark shift produced by a single beam (Equation 3.6). A frequency difference δ between the beams sets this lattice in motion. For the time being, we assume that the two beams have the same intensity, and neglect the spatial profile of that intensity. The spatial period of the lattice is

$$\lambda_{latt} = \frac{\lambda_{laser}}{2\,\sin\theta/2} \tag{3.20}$$

where θ is the angle between the lattice beams.

Diffraction from a grating

Bragg diffraction gets its name from the early experiments which involved scattering x-rays off of crystals [12]. The diffraction of light from a periodic structure is ubiquitous in our everyday lives (assuming you are in a laser lab everyday). One need not look any further than the gratings used to stabilize our diode lasers and the acousto-optic modulators we use to frequency shift our light.

We are of course interested in the Bragg diffraction of matter-waves. This, also, was first accomplished quite some time ago, with electrons diffracted off of a crystal of nickel [30]. A little closer to home, Dave Pritchard's lab diffracted a thermal beam of Na atoms off of a periodic optical potential [79].

The principle of diffraction is that a wave which is scattered off multiple sources, like the crystal lattice in Figure 3-5, will interfere constructively in some directions and decon-

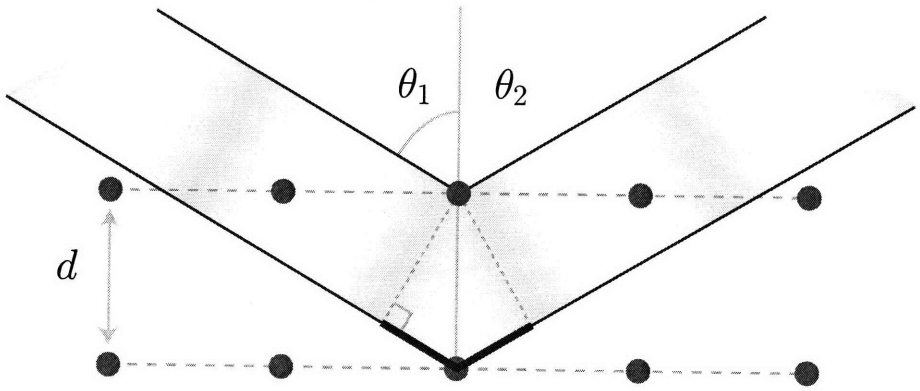

Figure 3-5: X-ray diffraction. The angle of diffraction of a wave off a lattice of point scatterers is given by the Bragg condition, Equation 3.21. This describes the condition for constructive interference of the various scattered components.

structively in others. The Bragg condition is satisfied when different path lengths differ by some integer number of wavelengths. For a crystal of lattice spacing d, interference is constructive when the angles $\theta_{1,2}$ of incident and outgoing x-rays satisfy

$$d\,(\sin\theta_1 + \sin\theta_2) = n\,\lambda \tag{3.21}$$

or, in other words, the *extra phase* accrued by the longer path is an integer multiple of 2π.

Bragg diffraction : Atoms scattering off a light grating

Our "atomic physics version" of Bragg diffraction can equally be described in this grating picture. The optical potential of a 1-D lattice acts as set of scattering planes, periodically spaced at $d = h/q$. An atom with incident velocity $\vec{v}$ has a de Broglie wavelength $\lambda = h/mv$. We can rewrite Equation 3.21 as

$$\begin{aligned} 2\,d\,\sin\theta &= \lambda \\ -2\,\frac{h}{q}\,\frac{\vec{v}\cdot\vec{q}}{vq} &= \frac{h}{mv} \\ -\vec{v}\cdot\vec{q} &= \frac{q^2}{2m} \end{aligned} \tag{3.22}$$

This is equivalent to the Bragg condition which we derived on energetic grounds in Section 3.3.2.

3.3.5 Band Structure

An obvious approach to understanding the physics of atoms in a periodic potential would be to solve for the eigenstates of the system, in which the Hamiltonian includes the lattice potential. Fortunately the field of condensed matter physics has done most of the work for us. The eigenstates are called *Bloch states*[3]

The lattice potential is invariant under a translation of the lattice spacing d, i.e., $V_{latt}(z) = V_{latt}(z+d)$. Bloch's Theorem tells us that this implies that the wavefunction, too, has translational symmetry, up to a phase. The Bloch wave functions are

$$\psi_{Qn}(z) = e^{iQz}\, u_{Qn}(z) \tag{3.23}$$

where $u_{Qn}(z)$ is some function with the periodicity of the lattice. n is the band index, and Q is the quasimomentum[4].

The eigenstates are not planes waves Φ_p of a certain momentum p, as they were for the free particle case, but rather a linear combination of momentum states differing by $\hbar\kappa$.

$$\psi_{Qn} = \ldots + c_{-1}\,\Phi_{Q-\hbar\kappa} + c_0\,\Phi_Q + c_1\,\Phi_{Q+\hbar\kappa} + c_2\,\Phi_{Q+2\hbar\kappa} + \ldots \tag{3.24}$$

where the c coefficients depend on n, Q and the lattice strength V_0. The quasimomentum Q is essentially momentum modulo $\hbar\kappa$, and we usually define Q to be in the range $-\hbar\kappa/2$ to $\hbar\kappa/2$, known as the first Brillouin zone.

In Figure 3-6 we shown the energies of the Bloch states for different lattice depth V_0. In the limit of zero lattice, we recover the quadratic free particle dispersion relation. The lattice has the effect of opening up gaps in the energy spectrum. For a very strong lattice, the wave functions become localized on the lattice sites, which look like individual harmonic oscillators. The bands flatten out, and the gap energy approaches the oscillator energy $\hbar\omega$.

3.3.6 Weak Lattice : Effective mass and interaction

Much of the physics of a shallow lattice ($V_0 \leq 1E_r$) can be captured in two phenomenological parameters. Or one, as we can see from Figure 3-6, the lattice changes the dispersion

[3] named after Felix Bloch, not Immanuel Bloch.

[4] Most literature uses "q" as the quasimomentum. I will use "Q" to avoid confusion with the previous use of q as defined in Section 3.3.2

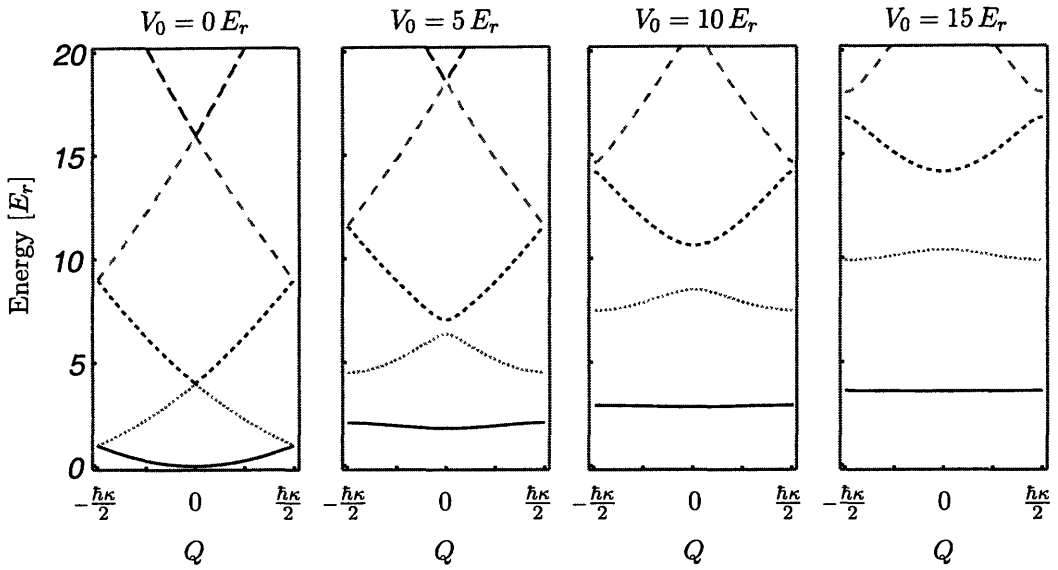

Figure 3-6: Band structure. A lattice potential modifies the free particle dispersion relation. The translational symmetry allows us to describe a state by its quasi-momentum Q and band index n. In the limit of large lattice depth, the bands flatten and become the harmonic oscillator energies for atoms on a single lattice site.

relation. For small changes, we can account for this by using an effective mass

$$\begin{aligned} M_{eff} &= \hbar^2 \left(\frac{\partial^2}{\partial Q^2} E(Q) \right)^{-1} \\ &= M \left[1 - 16\sqrt{2} \frac{\sqrt{32+s^2} - 4\sqrt{2}}{\sqrt{32+s^2}\left(\sqrt{32+s^2}+4\sqrt{2}\right)} \right] \end{aligned} \tag{3.25}$$

where we have expressed the lattice depth s in units of the recoil energy E_r.

The second effect of the lattice is to modify the the density, and therefore the mean-field energy. We can account for this with an effective interaction.

$$U_{eff} = \frac{4\pi\hbar^2 a}{m} \int_V d\vec{x}\, |\psi_0(\vec{x})|^4 \tag{3.26}$$

$$= \frac{4\pi\hbar^2 a}{m} \left[1 + \frac{2\alpha^2 (4+\alpha^2)}{(1+2\alpha^2)^2} \right]^D \tag{3.27}$$

where D is the dimension of the lattice, and

$$\alpha \equiv \frac{s}{4\,(4 + s^2/8)}$$

3.3.7 Bragg Scattering: Bloch State Interpretation

In Section 3.3.2 we introduced Bragg diffraction as the process of imparting momentum to atoms by redistributing photons between two laser beams. We can also describe this process in the context of Bloch states. In the rest frame of the lattice ($\delta = 0$), the Bragg process is resonant for atoms moving with velocity $v = \frac{\hbar\kappa}{2m}$ (Equation 3.16). It is no coincidence that this happens to be the Brillioun zone boundary. This (real) momentum state is an equal superposition of two eigenstates of the system

$$\left|p = \tfrac{\hbar\kappa}{2}\right\rangle = \left|Q = \tfrac{\hbar\kappa}{2};\ n = 0\right\rangle + \left|Q = \tfrac{\hbar\kappa}{2};\ n = 1\right\rangle \tag{3.28}$$

where n is the band index. Turning on the lattice projects the state $\left|p = \frac{\hbar\kappa}{2}\right\rangle$ onto this basis, and the phases of the different components evolve at their eigenfrequencies. When the relative phase becomes π, the population has been completely transferred into the momentum state

$$\left|p = -\tfrac{\hbar\kappa}{2}\right\rangle = \left|Q = \tfrac{\hbar\kappa}{2};\ n = 0\right\rangle - \left|Q = \tfrac{\hbar\kappa}{2};\ n = 1\right\rangle \tag{3.29}$$

We know that the band gap is $2V_0$, so the probability of this transfer evolves as

$$P = \sin^2 \frac{V_0 \tau}{\hbar} \tag{3.30}$$

where it should be no surprise that the frequency of this oscillation is the two photon Rabi frequency

$$\frac{V_0}{\hbar} = \frac{\Omega^2}{4\Delta} = \tfrac{1}{2}\Omega^{(2)} \tag{3.31}$$

3.3.8 Kapitza Dirac : a phase imprint

It is straightforward to to extend this description to include Kapitza-Dirac scattering, which we discussed in Section 3.3.3. The abrupt turn on of the Kapitza-Dirac beams projects onto the Bloch basis. The zero momentum state Φ_0 becomes a superposition of $Q = 0$ states in even bands ($n = 0, 2, 4\ldots$) due to symmetry. The Bloch states accrue a phase, and are then projected back onto the (real) momentum basis when the pulse ends, leaving the atoms distributed over the discrete momentum states.

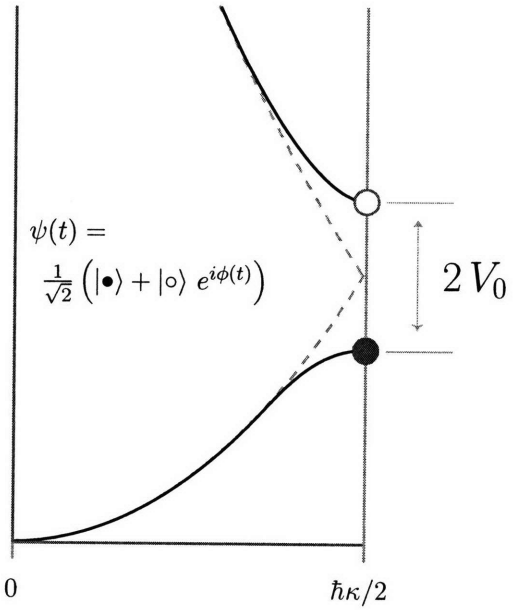

Figure 3-7: Bragg diffraction at the Brillouin zone boundary. The resonance condition for first order Bragg diffraction is satisfied for an atom with momentum $\frac{\hbar\kappa}{2}$, with respect to the lattice, corresponding to the zone boundary. The abrupt turn on of the lattice projects this plane wave state onto the eigenbasis of Bloch states, as an equal superposition of the lowest two bands. The two eigenstates (filled and open circles) accrue a relative phase $\phi = 2\,V_0\,t/\hbar$, corresponding to the band gap. A relative phase of π corresponds to the *real* momentum state -$\frac{\hbar\kappa}{2}$.

In fact, its quite easy to solve for what this distribution will be. Pulsing on the lattice for a very short time can be treated as imprinting a phase on the wavefunction

$$\exp\left[-i\,2\,V_0\,\tau - i\,2\,V_0\,\tau\,\cos\kappa z\right] \tag{3.32}$$

through the AC Stark shift. This sinusoidal phase can be written as a projection operator over discrete momentum states

$$e^{i\theta\,\cos\kappa z} = \sum_{n=-\infty}^{\infty} \mathcal{J}_n(\theta)\ \underbrace{e^{-in\kappa z}}_{|p+n\hbar\kappa\rangle\langle p|} \tag{3.33}$$

where the coefficients $\mathcal{J}_n$ are Bessel functions.

As for the validity of this approach : in order to treat the application of the lattice as a phase imprint, we need to make sure all motion during the length of the pulse τ is negligible compared to the lattice spacing $d = h/q$. Different momentum components move with velocity $v \sim q/m$, which means we want

$$\begin{aligned} v\,\tau &\ll d \\ \tau &\ll \frac{h\,m}{q^2} \end{aligned} \tag{3.34}$$

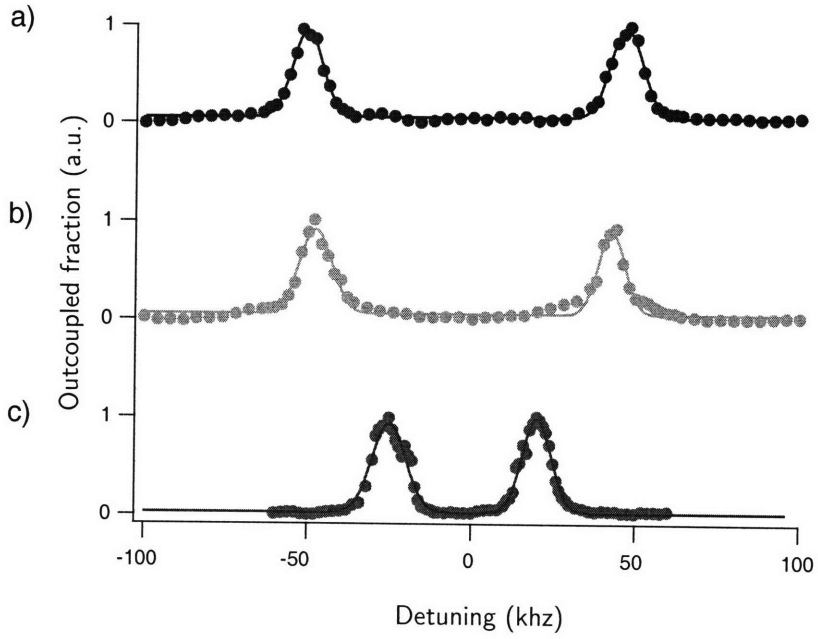

Figure 3-8: Bragg spectroscopy of atoms and molecules. The spectra for a pure atomic sample a) just above and b) below a magnetic Feshbach resonance at 907 G. c) Spectrum of a pure molecular sample just below the Feshbach resonance. Diatomic molecules recoil with half the velocity of single atoms, due to their mass. Figure from [1].

which is equivalent to Equation 3.18.

3.4 Bragg spectroscopy

The need to conserve both energy and momentum makes Bragg diffraction a velocity selective process, as is evident in Equation 3.16. This opens the possibility for its use as a spectroscopic tool which can reveal velocity distribution of an atomic sample. The process involves counting the number of outcoupled atoms as a function of the detuning $\delta\nu$ between the two Bragg beams. For a sample at rest, the signal (see, for example, Figure 3-8) is a peak at $\delta\nu = 4E_r/h$, where the Bragg condition is satisfied. The width of the peak reflects the velocity distribution, but may be broadened and shifted by a number of mechanisms. The finite duration of the Bragg pulse introduces an energy uncertainty in the photons absorbed, as discussed in Section 3.3.2, and limits our resolution. The mean-field interaction

energy results in a shift of the resonance for a BEC. Distinguishable atoms experience twice the mean-field interaction as do atoms in a condensate. This is reflected in the shift of the Bogloliubov excitation spectrum (Equation 2.5), in the free particle limit. The mean-field energy, however, is density dependent. This mean-field shift, then, must be integrated over the density profile, resulting in an inhomogeneous mean-field broadening.

Bragg spectroscopy was first implemented with a BEC in Ref [107], and a more thorough accounting of the shifts and broadening can be found in Jamil Abo-Shaeer's thesis [2]. We used Bragg spectroscopy to study the velocity distribution of a cold sample of $^{23}Na_2$ dimers (See Appendix B). Starting with an atomic BEC, we converted atom pairs into diatomic molecules by sweeping across a Feshbach resonance, as detailed in Section 2.3.1. The lifetime of the molecules was too short to allow for thermalization, and could not necessarily be considered a BEC. However, we were able to show that the velocity distribution of the molecular cloud was consistent with a "temperature" that was well below the critical BEC temperature.

3.5 Dynamical instability

In the previous sections we have discussed Bragg scattering in the context of single particles and photons. Such a lattice can also influence two-body interactions, in a manner which can redistribute momentum and result in dissipation. Ordinarily, two atoms with the same momentum $\hbar k$ can not scatter off each other into different momentum states, say $k + \delta k$ and $k - \delta k$. There is no way to conserve both momentum and energy. However, an optical lattice can change the dispersion relation so as to make such a process possible (see Figure 3-9). This process is analogous to the optical parametric generation of photons [16], in which the lattice provides for phase matching.

The energy spectrum of such excitations can be calculated for a BEC moving in an optical lattice by considering small perturbations to the Gross Pitaevski equation [112, 78, 113]. At a certain velocity, excitations with wavevector $\pm\delta k$ will have a complex energy and grow exponentially. Dynamical, or *modulational*, instabilities do not exist below a velocity of $0.5\, q_B/m$, where $q_B = \hbar\kappa/2$ is the Bragg momentum corresponding to the edge of the Brillouin zone. Above this threshold, however, these modes can be quite destructive [32].

In the photon picture, one can consider the two scattering atoms as sharing a Bragg

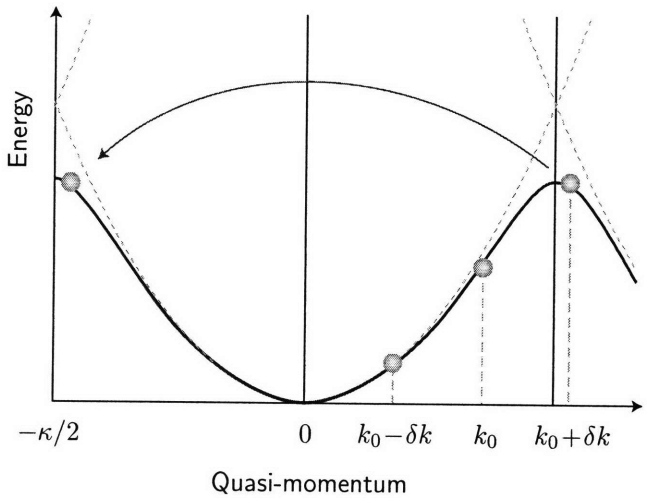

Figure 3-9: Dynamical instability. The scattering of two atoms with momentum k into states with momentum $k \pm \delta k$ does not conserve energy in the free particle dispersion relation. A dynamical instability occurs when an optical lattice modifies the dispersion relation so as to allow such a process.

excitation. At some momentum $\hbar k_0$, a single atom can not satisfy the Bragg condition. Although, together, two atoms can absorb the momentum kick $-\hbar\kappa$. The two recoiling atoms scatter off each other with momentum $\pm\hbar(\kappa - \delta k)$, in order to conserve energy. In this description, both scattered states appear to the *left* of the initial state k_0. This is equivalent to our previous understanding, in which the state $k_0 + \delta k$ lies across the zone boundary, and can be mapped back to the first Brillouin zone (see Figure 3-9).

Chapter 4

Experimental Apparatus

"Another flaw in the human character is that everybody wants to build and nobody wants to do maintenance."

- Kurt Vonnegut, Hocus Pocus

When I first joined the lab, I was fairly intimidated by apparent complexity of the experiment: the jungle of BNC cables, racks of homemade electronics boxes and a forest of optics on the laser table. Over time, I grew not only to understand this mess, but to contribute to it ... appreciably. In the summer of 2004, it was decided that the lab would change course, directing our focus upon fermions in an optical lattice. Shortly after committing to this new endeavor, at the ICAP poster session, we learned that the Zurich group [68] already had a degenerate Fermi gas in a 3-D lattice. Nevertheless, we felt we had a number of advantages. In particular our fermion of choice, ^{6}Li rather than ^{40}K, was much longer lived. Indeed, by May of 2006, we were the first (and still the only) group to have a superfluid Fermi gas in a 3D lattice. The question, of course, remains what to do with it.

This Chapter is intended to give an overview of the machine on which I have worked for the past five years. It is far from a comprehensive owner's manual. The Ph.D. thesis of Dallin Durfee [37] chronicles the original building of this machine, as a ^{23}Na experiment. The retrofitting of the oven as a double species model was done under the guidance and according to the precise specifications of Claudiu Stan [105], the many details of which can be found in his thesis. A number of important modifications to the machine are recorded in the thesis Jit Kee Chin [23], as well. To this extensive body of work, I will add a largely anecdotal account of *things to do* and *things **not** to do.*

4.1 Overview

While there are some variations on the theme, the preparation of a quantum degenerate atomic gas has become fairly standardized. Our experiment begins with a sample of alkali metal, heated in an oven, to produce a gas. A thermal atomic beam escapes through a nozel and traverses the Zeeman slower. Here the atoms are slowed by a counter propagating laser beam which imparts momentum as photons are scattered. As the atoms slow down and fall out of resonance with the light, due to the doppler shift, a spatially varying magnetic field compensates by shifting the energy levels. The slowed beam makes its way into the main vacuum chamber, where the background gas pressure is $\sim 10^{-11}$ Torr. Here, a magnetic quadrupole potential and six intersecting laser beams create a Magneto Optical Trap (MOT) which provides a confining as well as a viscous force.

After collecting atoms in a MOT, the light is shut off, and a Ioffe-Pritchard magnetic trap confines weak field seeking atoms at a magnetic minimum. The sample is cooled further by forced evaporation, in which a radio-frequency (r.f.) field flips the spin of the hottest atoms, expelling them from the trap. The sample rethermalizes, and the r.f. "knife" is brought to a lower temperature over thirty seconds. For ^{23}Na atoms, this results in a BEC. The preparation of a ^{6}Li gas involves a few more steps.

Identical fermions can not be evaporated, as the Pauli exclusion principle prohibits the thermalizing collisions. As a first stage we use sodium as a refrigerant to cool the lithium sympathetically. The cold lithium is then transferred to an optical trap, and the magnetic field is ramped to 820 gauss. At this field we take advantage of a Feshbach resonance between the lowest two hyperfine states, which provides strong interactions and a coupling to a weakly bound molecular state. We make a 50/50 spin mixture of these two spin states and induce evaporation by lowering the optical trapping potential. The atoms pair up and form a BEC of molecules.

In the following Sections we will discuss the components of the experiment in greater detail.

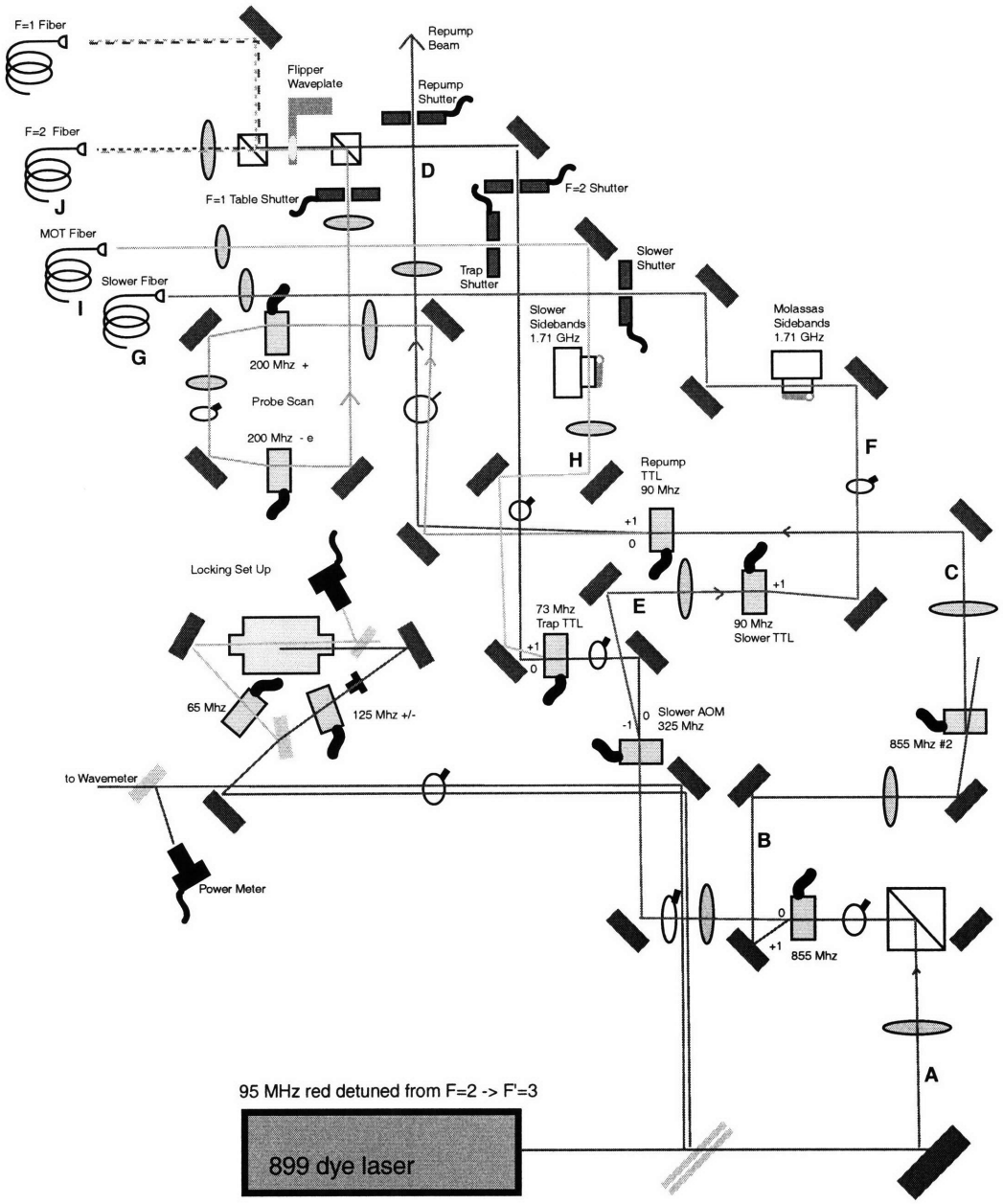

Figure 4-1: The sodium laser table. Letters denote the positions of power measurements as listed in Table 4.1.

4.2 The Sodium laser system

4.2.1 The 899 dye laser

We use a Coherent model 899 dye laser to generate light at 589.160 nm (D2 line). Pumped by 9.5 watts of 532 nm green light from a Spectra Physics Millenia solid state laser, we get 1.6 watts of yellow light. The gain medium is Rhodamine 590G dye, dissolved in ethylene glycol. The dye is prepared in $\sim$ 1.4 liter batches, which typically last 500 working hours. The Rhodamine dye, dissolved in methanol, is added to the ethylene glycol until the absorption of pump light by the dye jet is 90% (as measured at full power). The dye, which is pumped through a high pressure nozzle at 12 bar, must be cooled to 6° C. This maintains a high viscosity which results in the proper profile of the dye jet. The dye jet should be flat at the center. Streaks in the jet may indicate a clogged nozzle, which can be disassembled and cleaned with methanol in the ultrasound bath. Great care must be taken not to nick the edges which form the nozzle opening.

It is not uncommon to find the laser power to have dropped precipitously since the last use. Since the laser is a finely tuned machine, it pays to be prudent in your attempts to get the power back, as not to cause greater harm. Adjustments to the birefringent filter and the pump mirror alignment are the first course of action, and performed several times a day. Additional fiddling should not be necessary more than once a month. Before turning too many knobs, inspect the cavity mirrors for any obvious dust particles. Tweak the output coupler next. This will require that the laser table be realigned. A full cavity tune up, if necessary, should always be followed with a realignment of the reference cavity. There are some less obvious surfaces which can accumulate dust, such as the underside of the birefringent filter, and the fragile polarizer in the optical diode assembly. Wiping the mirrors with lens paper and methanol is a necessary part of maintenance, but should be kept to a minimum. As a Coherent tech once told me *"the two worst things you can do to a laser cavity are, one, to get it dirty and, two, to clean it."*

A less frequent source of trouble is the Millenia pump laser. A perfect Gaussian mode is essential to the efficient pumping of dye jet. The laser can begin to fail in such a way as to put out a slightly distorted mode, usually at high power. I have seen two different units exhibit this behavior. The signature of this failure mode is most evident when ramping the laser power up from zero. The output of the dye laser will climb with increasing pump

Measurement Location		Power	
A	Total Power	28 μA	1.55 W
B	855 mhz #1	1.75 μA	
C	855mhz #2	0.9 μA	
D	Repump TTL	0.7 μA	33 mW
E	Slower AOM	3.75 μA	
F	Slower TTL	3 μA	
G	Slower Fiber	600 mV†	95 mW
H	Trap TTL	9 μA	
I	MOT Fiber	500 mV‡	150 mW
J	Optical Pump	1.2 V	6 mW

Table 4.1: Typical laser powers. Measurement positions are indicated in Figure 4.2. Measurements in μA are taken with the blue Hickok power meter. Measurements in mV are the monitor readings of photodiodes at the fiber output. Actual powers in mW are measured with the Coherent optical power meter.

† The slower is run at $\sim$ 350 mV.
‡ The MOT is stabilized to 425 mV.

power, and then drop abruptly at some threshold. It is possible to run the Millenia just below this threshold, if it results in sufficient power, but one needs to approach this value from below, as there is hysteresis in the system. Obviously the best solution is to put in a service call to Spectra.

There are two dirty tricks which can temporarily boost power, but can not substitute for a proper alignment. One is to add some dye concentrate (Rhodamine in methanol). This only works if the current batch is getting old, and can quickly backfire if one adds too much. A second, and cheaper, trick is to tighten the focus of the pump laser. Over-tightening the pump focus has two drawbacks. The output mode of the laser can change, taking on a "D" shape, resulting in poorer fiber coupling. It will also make the laser less stable, falling out of lock much more frequently. When used in a pinch, however, these techniques can keep things going long enough to get some data.

4.2.2 The laser table

For the most part, the laser table today remains exactly as it was when I first arrived. An absorption cell is used for the locking, based on saturation-absorption spectroscopy. At

times, the lock signal may flicker between the familiar trace and sharp spikey noise. This just means that the thin etalon needs to be adjusted, as the gain profile is not centered on the desired mode. We shift the light by a number of different frequencies using acousto-optical modulators. The basic principle is that an actuator, driven at some radio frequency, sends acoustic waves down a crystal. This periodic density modulation acts like a moving grating, which diffracts the light into multiple orders, which are conveniently spatially separated. As illustrated in Figure 4.2, we will pick off light from the main beam for a particular purpose using an AOM. The zero order usually continues on to serve a different function. It is noteworthy that the AOMs tend to pick out the best part of the mode, diffracting a nearly perfect gaussian beam into the ± 1 order, and leaving something less than ideal in the zero order. As a consequence, redistributing power between paths is not necessarily a conservative process, when fibers are involved. On our table, light from the MOT path has syphoned off for the Slower and Repump paths, and the fiber coupling is optimized for this depleted mode. If we were to take so many milliwatts out of the Slower by turning down the Slower AOM, a disappointing fraction of that would end up coupled through the MOT fiber.

Of all the optical components in the lab, one stands out as being the most valuable: the 855 mhz IntraAction AOM. We purchase our AOMs from IntraAction Corp., whenever possible, since their products have the largest aperture size. Unfortunately, high frequency AOMs can be challenging, and they claim not to be able to reproduce this model anymore. And it would not be without precedent for it to fail. We used to have two in series, until one died. To replace it with with the Brimrose would require that the beam be focused down to accommodate the smaller aperture, thus affecting everything downstream, which is to say *everything.* Unfortunately, a more tightly focused beam, at 2 watts (on a good day) would most likely exceed the damage threshold of the crystal.

4.2.3 The Sodium MOT

For Sodium, we use a dark spot magneto-optical trap [67]. The six intersecting MOT beams have σ^+ polarization, and are tuned 22 mhz below the $|F = 2\rangle \rightarrow |F' = 3\rangle$ transition. A single "repump" beam, tuned to the $|F = 1\rangle \rightarrow |F' = 2\rangle$ transition, pumps atoms out of the F=1 state, which is dark to the MOT light. Only the outer edge of the MOT is illuminated by the repump light. This is accomplished by imaging a dark spot, a blob of black nail

polish on glass, onto the MOT. The glass cell is what most differentiates the New Lab, from the other three BEC machines on the hallway. It affords a superior optical access which is most beneficial when the MOT needs realignment. Our well tuned Na MOT has produced the largest BECs in the world (120 million atoms).

Measurement Location		Power	
A	Total Power	40 μA	400 mW
B	Slower AOM	12 μA	110 mW
C	Repump 228	15 μA	110 mW
D	Repump TTL	10.5 μA	80 mW
E	MOT TTL	11.5 μA	80 mW
F	Slower TTL	10 μA	75 mW
G	Slower Fiber	1.08 V	37 mW
H	MOT Fiber	1.65 V	55 mW
I	Repump Fiber	1.48 V	55 mW

Table 4.2: Typical laser powers. Measurement positions are indicated in Figure 4.3. Measurements in μA are taken with the blue Hickok power meter. Measurements in V are the monitor readings of photodiodes at the fiber output. Actual powers in mW are measured with the Coherent optical power meter.

4.3 The Lithium laser system

We use a Toptica TA100 tapered amplifier laser system to generate the necessary light for manipulating ^{6}Li. Many of the details of this system may be found in Ref. [101]. Prior to obtaining this relatively care free laser, we were able to work with a Coherent 699 dye laser. While the power was more than sufficient, this laser required a significant amount of maintenance. In Figure 4.3, we show the arrangement used for obtaining the numerous different beams required for the experiment.

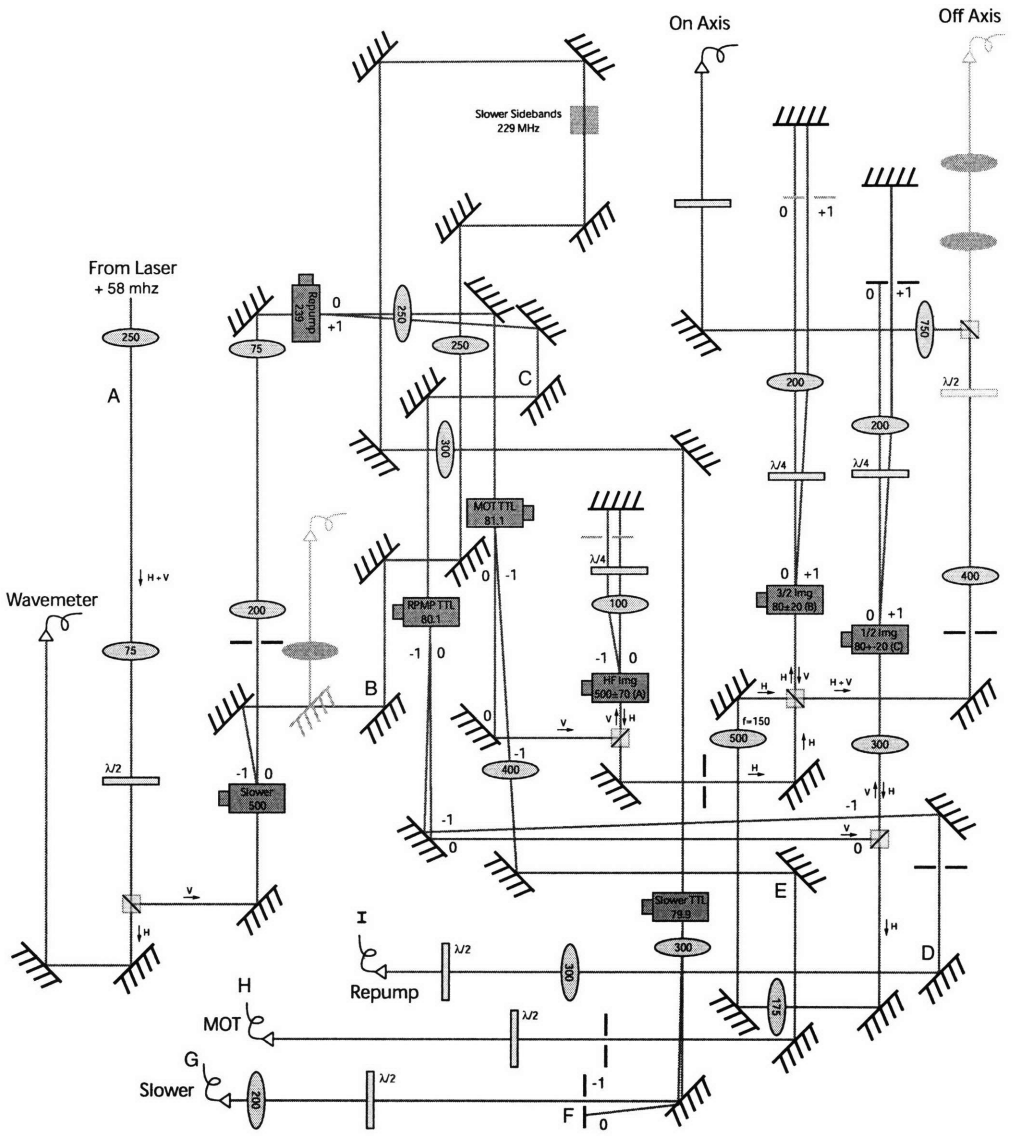

Figure 4-2: The lithium laser table. Letters denote the positions of power measurements as listed in Table 4.2.

4.4 The Infrared laser system

We use a 20 watt IPG Photonics fiber laser to generate the light for optical trapping and lattices. Figure 4-3 offers a schematic of the numerous IR beams which are used in the experiment. The laser light is split up first on an optical table, the arrangement of which details their chronology, before being sent to the experiment via optical fiber. In this Section we describe how different beams are implemented.

Working with multiple beams

A single beam ODT will naturally produce a long cylindrical trap, since the Rayleigh range is much longer than the beam waist. This geometry is not always desirable. We can, however, use two intersecting beams to produce a cross-ODT, which has a more spherical shape. In this case, the trap frequencies produced by the two beams add in quadrature. This is of course saying nothing more profound than that we add the potentials of the two beams.

$$V(x) = \frac{1}{2} m \omega_1^2 x^2 + \frac{1}{2} m \omega_2^2 x^2 = \frac{1}{2} m (\omega_1^2 + \omega_2^2) x^2 \tag{4.1}$$

If this is the desired effect, we need to make certain that the two beams do not interfere with each other, resulting in a spatial modulation of the trap. In principle, one can set the polarizations of the two beams to be orthogonal. However, this never works perfectly, in practice. Additional security is gained by using different frequencies. If the beams are derived from AOMs which differ by tens on megahertz, any interference pattern will move fast enough as to be time averaged away.

This, of course, assumes that your laser is single frequency. If it is not, you may wind up with frequency components that differ just so as to satisfy a Bragg resonance (which we discuss in the following Chapter). This was found to be the case when we used the *Versadisk* laser by ELS, and resulted in significant heating even when the two polarizations were made to be as orthogonal as possible.

Sometimes, even a single beam can be troublesome, as Figure 4-4 illustrates. There was a time when we noticed that a Na BEC released from our single beam ODT exhibited discrete momentum components, characteristic of having been released from a lattice potential. Except we weren't applying a lattice. Or so we thought. The ODT was aligned along our imaging axis, which used a dichroic mirror. While visible light was reflected onto the

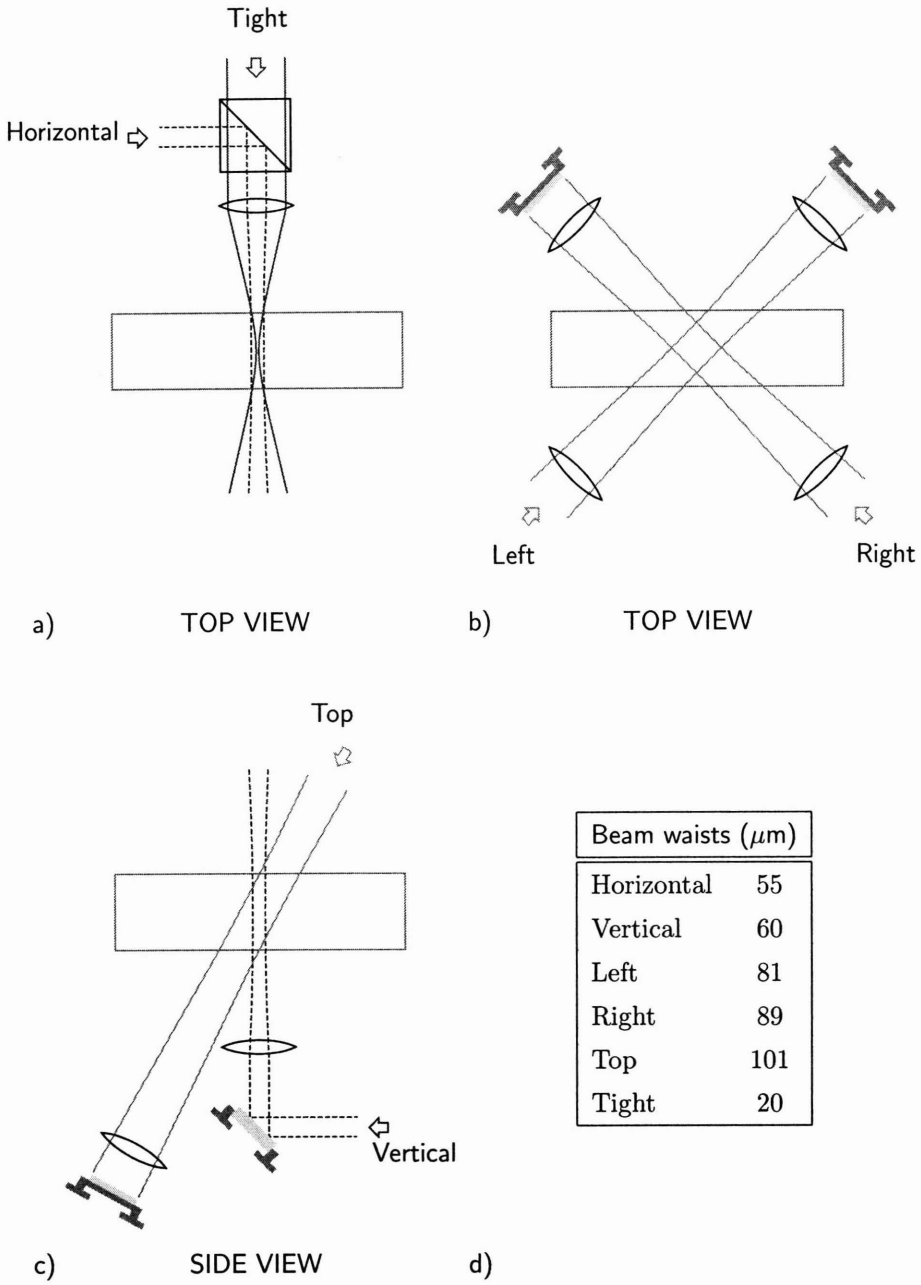

Beam waists (μm)	
Horizontal	55
Vertical	60
Left	81
Right	89
Top	101
Tight	20

Figure 4-3: Infrared laser system. Beam lines are shown with respect to the glass cell (box). a) The *Horizontal* and *Tight* beams are overlapped on a PBS cube before being directed onto the imaging path by a SWP dichroic mirror (not shown). b) The *Left* and *Right* lattice beams are oriented in the horizontal plane at 45° to the slowing axis. c) The *Vertical* beam is overlapped onto the MOT path using a SWP dichroic mirror. The *Top* lattice beam makes an angle of 20° with the horizontal plane. d) Beam waists (e^{-2} radius).

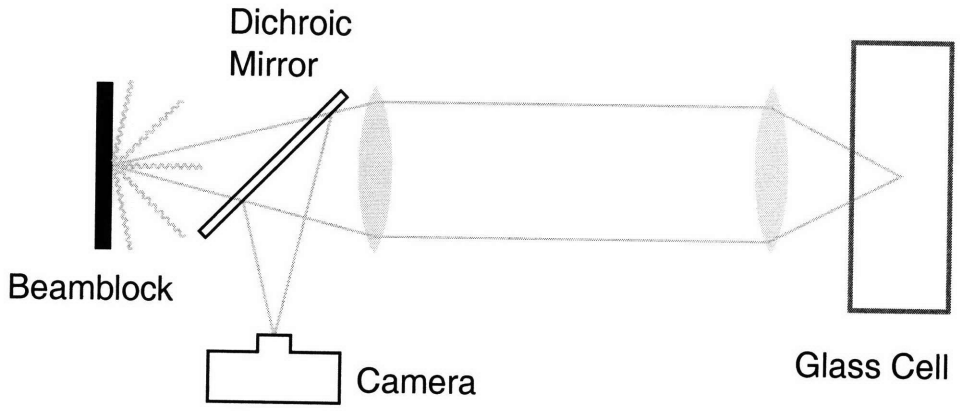

Figure 4-4: An accidental lattice. An optical dipole trap (ODT) is aligned on the imaging axis. A long wave pass dichroic transmits the ODT beam, which impinges on a beamblock. When the beamblock is located at the focus of the imaging system, much of the scattered light is imaged back onto the atomic sample, interfering with the incident ODT beam to produce a lattice.

camera, infrared was transmitted, and so a beam block was positioned in order to prevent that Watt of IR from wandering aimlessly. This beamblock had been positioned, without much thought, very close to the focus of the imaging system. So, while the light was being scattered uniformly, much of it was simply re-imaged back onto the condensate, interfering with the incident ODT.

Once the cause of this accidental lattice was identified, we simply moved the beamblock, alleviating the problem.

4.4.1 The different infrared potentials

The Tight Trap

After sympathetically cooling our Li sample, we transfer to an optical trap in order to work at high magnetic fields. At this stage, we need a large volume trap, so a single beam trap is preferable to a cross ODT. Other experiments [121] use a hybrid trap, in which the IR provides radial confinement, whereas the axial trapping is done magnetically. This configuration requires some finesse, as the magnetic moment is flipped when the atoms are transferred from the $|F = 3/2\rangle$ to the $|F = 1/2\rangle$ state. Instead, we opted to use tightly focused beam which has a Rayleigh range sufficiently short so as to provide axial confinement.

The *Tight* beam is focuses up to 6 watts of power down to 20 μm. It is overlapped with the *Horizontal* IR beam with a polarizing cube, and then onto the imaging path with a short wave pass (SWP) dichroic mirror (not pictured). This beam uses enough of the total laser power so as to limit other applications. For that reason, we are able to dynamically allocate power on the laser table. A $\lambda/2$-plate controls the distribution of power between the Tight beam and other branches, splitting the two paths on a cube. The $\lambda/2$-plate is mounted on a rotation mount which is controlled by a servo motor. During the relatively slow (1 s) evaporation stage we rotate the plate, putting the light to work elsewhere.

The cross ODT

We form a cross optical dipole trap at the intersection of the *Horizontal* and *Vertical* beams, which have beam waists of 55 μm and 60 μm, respectively. This provides a relatively spherical trap for our lattice work. This is preferable from primarily a technical standpoint. An elongated trap presents too large of a surface area to the lattice beams. The beams are detuned by 60 mhz with respect to each other, to prevent interference effects.

The optical lattice

The optical lattice featured in Ref [24], which we discuss in Chapter 6, is comprised of three different beams, retro-reflected upon themselves, and detuned by tens of mhz with respect to each other. The *Left* and *Right* beams are in the horizontal plane, intersecting the slower axis at 45°. The *Top* beam makes an angle of 20° with the horizontal plane, resulting in a lattice which is sheared rather than square.

The moving lattice

In the critical velocity experiment (Chapter 7) we use a moving 1D lattice to probe the Li sample, in one of two different configurations (see Figure 7-3). A moving lattice usually involves two different beams[1]. A frequency difference between the beams $\delta\nu$ sets the lattice in motion with velocity $v = \delta\nu\,\lambda_L$. The beams, which intersect at 90°, produce a lattice spacing of $\lambda_L = 0.75\mu$m, corresponding to a recoil energy $E_r = h \times 7.3$ khz for a Li pair, and twice that for a single atom (see Equation 3.17). The frequencies of the beams are shifted

[1] Alternatively, a DC EOM can be placed in the retro-reflecting path of a single beam. The lattice is then translated by changing the voltage across the nonlinear crystal.

by AOMs on the laser table. For such small shifts ($\sim$ 10 khz), the AOM deflection is not significantly altered, and the coupling into the fibers is preserved. This velocity can be be computer controlled for experimental convenience. An Agilent function generator provides the signal to the AOM driver, and can be GPIB controlled using a fine piece of software written by Widagdo Setiawan [101].

The first lattice geometry we use is similar to that used in the 3D lattice experiment [24], in which the lattice is relatively homogenous over the size of the trapped cloud. The sample is held in a cross ODT, formed by the *Horizontal* and *Vertical* beams. The 1D lattice is formed by the interference of the *Left* and *Right* lattice beams (the retro-reflections are blocked).

The second configuration we use aims to localize the lattice within the trapped cloud. Here we use the *Left* and *Right* lattice beams as a cross ODT, which has a larger volume then that formed by the *Horizontal* and *Vertical* beams. The lattice is created at the intersection of the *Vertical* and *Tight* beams.

4.4.2 ODT Calibration

While the trap frequencies are simple to calculate, we never take such calculations at face value. The most reliable method of calibrating our trap is to watch a dipole oscillation. A small pulse of current through one of the magnetic coils will *kick* a condensate, and we can measure the oscillation frequency by taking shots at successive hold times. For our two species experiment, it is often easier to characterize the trap with a ^{23}Na condensate, and scale the trap frequencies for ^{6}Li. The scaling goes as the square root of the polarizability over the mass, and for 1064 nm light is

$$\frac{\omega_{Li}}{\omega_{Na}} = 2.1 \tag{4.2}$$

For a shallow trap, one must be careful, as the two species experience a different *gravitational sag*. Usually this gradient can be compensated by magnetic levitation.

There are some situations in which applying a magnetic kick is not possible, at least not along all three principle axes. For example, at very high bias fields it is difficult to apply a radial gradient, since fields would have to add in quadrature to the strong bias. In this case, it may be best to use parametric heating. A modulation of the trap power at twice

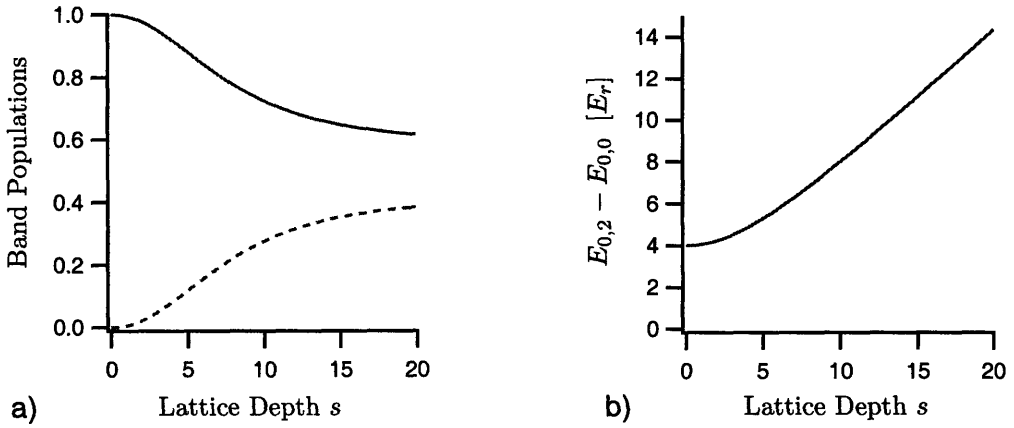

Figure 4-5: Band populations and energy gap. a) At a lattice depth s, the zero momentum state is a superposition of the eigenstates with zero quasimomentum in the $n = 0$ and $n = 2$ bands. The weightings of $\psi_{0,0}$ (solid line) and $\psi_{0,2}$ (dashed line) are shown (see also Equation 4.3). b) The energy difference between the $n = 0$ and $n = 2$ bands at $Q = 0$ sets the oscillation frequency of Kapitza-Dirac scattering, and can be approximated by Equation 4.4.

the trap frequency will induce resonant heating.

4.4.3 Lattice Calibration

There are a number of ways to calibrate an optical lattice [117]. On can, for example, look for resonant heating. Modulation of the lattice depth will drive a transition between the $n = 0$ and $n = 2$ bands at the correct frequency. Similarly, shaking the lattice back and forth will excite transitions between the $n = 0$ and $n = 1$ bands, although this is not easily accomplished in a simple retro-reflected configuration.

We usually calibrate our lattice using Kapitza-Dirac scattering (Section 3.3.3). Abruptly turning on the lattice potential projects the zero momentum state Φ_0 onto primarily the lowest two even bands. The band populations as a function of lattice depth $s = V_0/E_r$ are shown in Figure 4-5a. The overlap with the second band is approximately

$$|\langle \Phi_0 | \psi_{0,2} \rangle|^2 \approx \frac{0.4\, s^2}{73 - 2.86\, s + s^2} \,. \tag{4.3}$$

The population of the zero and first order diffraction peaks, in time of flight, oscillate as a function of the pulse duration at a frequency given by the energy difference between bands.

This energy difference, shown in Figure 4-5b, is approximately

$$E_{0,2} - E_{0,0} \approx \sqrt{16 + \frac{12}{25} s^2}\ E_r \ . \tag{4.4}$$

In the limit of vanishing lattice depth we recover the free particle relation. The kinetic energy associated with absorbing two photons is 4 E_r. At low lattice depth, this curve is fairly flat, and the Kapitza-Dirac oscillation is not a very sensitive measurement of V_0. It is best to work with a potential $V_0 > 10\, E_r$.

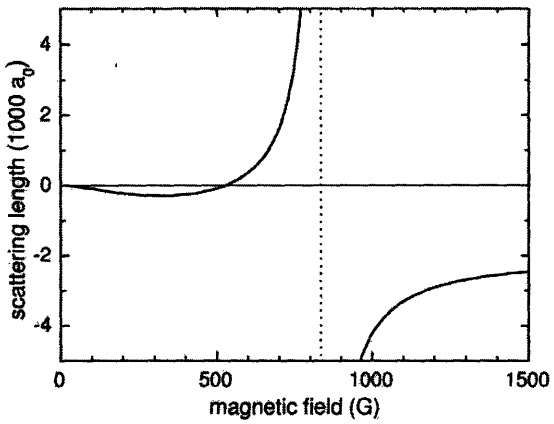

Figure 4-6: The broad Feshbach resonance between the two lowest hyperfine states in ^{6}Li, as given by Equation 4.5, from [8]. A narrow resonance also exists at at 543 G, near the 528 G zero crossing, and is not resolved on this scale.

4.5 The Lithium Feshbach resonance

While not exactly a piece of equipment, the Feshbach resonance between the two lowest hyperfine states in ^{6}Li does provide a "knob" which we quite frequently turn. A good deal of effort has been put into precisely characterizing this resonance [8]. Here I will simply state the result, which we show in Figure 4-6.

$$a(B) = a_{bg}\left(1 - \frac{\Delta B}{B - B_0}\right)(1 + \alpha(B - B_0)) \tag{4.5}$$

with $a_{bg} = -1405\,a_0$, $B_0 = 834.15$ G, $\Delta B = 300$ G, and $\alpha = 0.040\,\mathrm{kG}^-1$; here $a_0 = 0.529177$ nm is Bohrs radius.

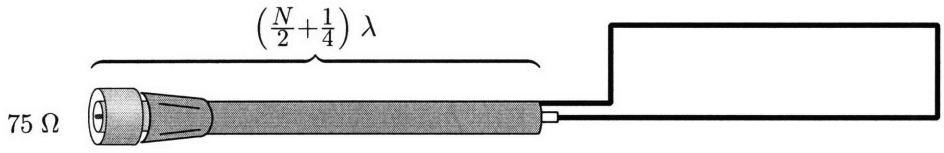

Figure 4-7: The Q-section antenna, built from a 75 Ω BNC cable.

4.6 The Q-section antenna

Efficient microwave evaporation is an important aspect of the preparation of a degenerate gas. High power amplifiers are expensive. Not only is it a shame to waste power through poor coupling, but it can be counter productive. Before we made any attempt to better impedance match our antennas to the 50 Ωtransmission line, many antennas mysteriously failed after a few days of use. Fortunately there is a simple way to achieve decent impedance matching.

A full-wave rectangular loop antenna, i.e. an antenna that is one wavelength in perimeter, has an impedance of about 100 Ω, as a rule of thumb. If we use a section of 75 Ω cable in between the antenna and the 50 Ω cable which runs to the amplifier, we can cancel much of the loss. Specifically, the 75 Ω *Q-section* needs to be $\lambda/4$ in length (plus an integer multiple of $\lambda/2$). The result is that the reflection off the 50 Ω to 75 Ω interface will interfere deconstructively with that off the 75 Ω to 100 Ω interface.

We implemented this by making the antenna out of 75 Ω BNC cable (RG59). A length of the cable is left intact for the Q-section, and the rest is stripped. The core was cut to the appropriate length for one wavelength, which for 1.7 Ghz, is about 7 inches. The end is then soldered to the shielding to complete the loop. As a finishing touch, the bare wire was insulated by wrapping Teflon pipe seal tape around it.

The antenna which we have made in this fashion has worked reliably for two years, and is many times more efficient than unmatched antennas, as measured by the minimum microwave power required to achieve Na BEC.

Chapter 5

Matter-wave Interference in a Thermal Cloud

Wave particle duality is fundamental to the quantum mechanical description of matter. Since the first observation of matter wave interference [30], matter wave interferometry has been discussed as superior to optical interferometry, in certain applications, owing to the accessibility of short wavelengths and long interaction times. Atom interferometers have since emerged as the leading instrument for certain precision measurements [51, 75, 90, 50]. While a BEC exhibits a spatial coherence that is equal to its size [87, 52, 10], a trapped thermal cloud can exhibit strong interference effects. This motivates a better understanding of the coherence properties of non-condensed atoms.

This chapter supplements work reported in the following publication:

D. E. Miller, J. R. Anglin, J. R. Abo-Shaeer, K. Xu, J. K. Chin, and W. Ketterle *"High-contrast interference in a thermal cloud of atoms,"* Phys. Rev. A 71, 043615 (2005).

(Included in Appendix A) Ref [83]

5.1 A Young's double slit for cold atoms

In the classic Young's double slit experiment, light is incident on a plate which has two slits cut into it, separated by a distance d. Further down the line, the intensity of the transmitted light exhibits fringes, resulting from the interference between the two "coherent" sources. The fringe spacing is inversely proportional to the slit spacing d.

A similar experiment was able to clearly demonstrate the wave nature of matter [30]. Electrons passing through a double slit would impinge upon a detector, registering as an individual spot. The accumulation of many spots, however, would add up in the form of an interference pattern. While the measurement of each electron collapsed the wavefunction to a single position, the ensemble average revealed a probability distribution $|\psi|^2$ which had fringes.

5.1.1 Matter wave interference of BEC

The first matter wave interference with BEC used a geometry similar to the Young's double slit experiment [6], which we illustrate schematically in Figure 5-1. A blue detuned laser beam was used to divide a trapped BEC into two. When released from the trap, the time of flight image revealed interference fringes.

During ballistic expansion, the wavefunction acquires a quadratic phase profile. In other words, an atom which has traveled a distance x during an expansion time t must have had a velocity $v = x/t$, and accrued a phase proportional to this kinetic energy. We can write the wavefunction as the combination of two wave packets, separated by a distance d.

$$\psi_{\pm}(x,t) = \sqrt{n_{\pm}(x,t)} \ \exp\left\{ i\frac{m}{2\hbar t}(x \pm d/2)^2 \right\} \tag{5.1}$$

where $n(x,t)$ is the density. The resulting matter wave interference pattern is

$$n(x,t) = n_0(x,t) \ \left[\tfrac{1}{2} + \tfrac{1}{2} \cos\left(2\pi \frac{x}{\lambda_f} \right) \right] \tag{5.2}$$

where $n_0(x,t)$ is the density envelope, and the fringe spacing is given by

$$\lambda_f = \frac{h\,t}{m\,d} \tag{5.3}$$

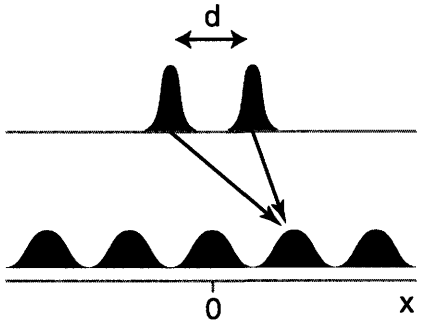

Figure 5-1: Young's double slit type experiment with matter waves. A wavefunction consisting of two wavepackets separated by a distance d reveals an interference pattern with fringe spacing $\lambda_f = ht/md$, after a time t of ballistic expansion. This reflects the different phases accrued by the different path lengths.

5.1.2 Trapped atom interferometry

An interesting application of this geometry would be to create the analogue of Mach-Zender interferometer with atoms. For example, we could have included a fixed phase term in Equation 5.1. Applying a phase shift to one wave packet shifts the position of the interference fringes. A number of experiments have demonstrated ... double-well

5.2 Interference of Thermal Atoms

The interference pattern we described in Equation 5.2 is just as valid for a single atom wavefunction as it is for the macroscopic wavefunction of a BEC. However, an ensemble of thermal atoms will add up incoherently, reducing the fringe contrast. In addition, for thermal atoms, the double-well potential does not in general result in the wavefunction we desire: that is, a superposition of two spatially separated wavepackets. The thermal de Broglie wavelength λ_T is usually shorter than the well separation d which can be achieved, and one ends up with two incoherent thermal clouds. We can, however, create this wavefunction using Bragg diffraction.

5.2.1 Autocorrelation pulse sequence

In our experiment, a sample of ^{23}Na atoms was cooled in a magnetic trap to a temperature T above the critical Bose-Einstein condensation temperature T_c, using rf-evaporation. We used a sequence of $\pi/2$ Bragg pulses to prepare each atom in a superposition of spatially separated wavepackets. The details of the sequence are given in Figure 5-2. The two Bragg beams, which intersect at $\sim 90°$, were large enough to be considered uniform over the size R_T of the trapped thermal cloud. In addition, the duration $\tau = 10\,\mu$s of the Bragg pulse

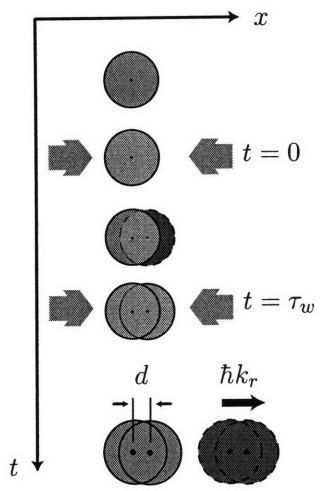

Figure 5-2: Autocorrelation pulse sequence. The first $\pi/2$ Bragg pulse creates an equal superposition of states with momentum 0 and $\hbar k_r$. After a time τ_w, the two states have separated spatially by a distance d. A second $\pi/2$ pulse converts each wavepacket into a superposition of the two momentum states. The result is one pair of wave packets at rest, separated by d, and a second pair traveling with momentum $\hbar k_r$.

was chosen to be short enough so as to couple the entire range of velocites in the thermal cloud, as in in Figure 3-3a.

5.2.2 Interference fringe contrast

Figure 5-3a shows an absorption image of a thermal cloud which has expanded after the pulse sequence. We fit the integrated optical density to the following function

$$n(x) = f(x)\left[1 + C\,\sin\left(\frac{2\pi}{\lambda_f}x + \phi\right)\right]. \tag{5.4}$$

to obtain a value for the fringe contrast C. The envelope function $f(x)$ is that of two gaussians, accounting for both the stationary and recoiling ($\hbar k$) clouds. The contrast is shown to be a decreasing function of cloud temperature, as shown in Figure 5-3c.

The functional form of the contrast can be easily derived. As we discussed in Section 5.1.1, a single particle wavefunction gives perfect contrast, with a fringe spacing $\lambda_f = ht/md$. We can model our thermal cloud as an ensemble of gaussian wavepackets of a width given by the thermal de Broglie wavelength[1]

$$\lambda_T = \frac{h}{\sqrt{2\,m\,k_B\,T}} \tag{5.5}$$

[1]The de Broglie wavelength is sometimes defined as $\lambda_T = \sqrt{\frac{2\pi\hbar^2}{mk_BT}}$. This choice is made so as to write the partition function as $\zeta \equiv \sum e^{-\epsilon/kT} = V/\lambda_T$, where V is the volume, as in [96, 91]

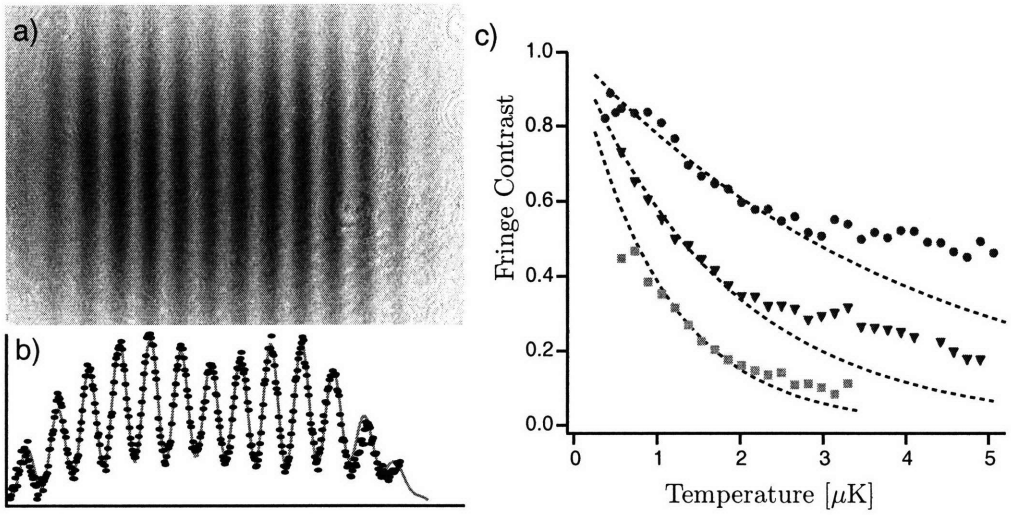

Figure 5-3: High contrast interference of a thermal cloud of atoms. a) Absorption image taken after 48 ms expansion. b) The integrated optical density is fit to Equation 5.4, resulting in a value for the fringe contrast C. c) Measured fringe contrast C as a function of temperature, for fringe spacing $\lambda_F = 340\,\mu m, 230\,\mu m, 170\,\mu m$ (circles, triangles, squares). The theoretical contrast of Equation 5.8 (dashed lines) describes the data well at low temperature.

These wavepackets are distributed over the thermal size of the cloud R_T in the trap

$$R_T = \sqrt{\frac{k_B T}{m\omega^2}} \tag{5.6}$$

where ω is the trap frequency along the axis we are probing. Integrating over the size of the cloud

$$n(x) = \int_{-\infty}^{\infty} dx_0 \; \frac{1}{\sqrt{2\pi R_T^2}} e^{-x_0^2/2R_T^2} \; \frac{1}{2} f(x - x_0) \left[1 + \cos \tfrac{2\pi}{\lambda_f}(x - x_0)\right] \tag{5.7}$$

we find the reduced fringe contrast

$$C = \exp\left(-\frac{2\pi^2 R_T^2}{\lambda_f^2}\right) \tag{5.8}$$

More simply stated, we loose contrast when we smear out the signal over a size equal to the fringe spacing. In Figure 5-3c we see that this result, without any free parameters, is in excellent agreement with the measured values of contrast, for several values of λ_f. At high

temperatures , however, the data deviates from Equation 5.8. We will discuss the reason for this in Section 5.3.

Density Matrix

The model we have suggested, gaussian wavepackets of width λ_T distributed across R_T (as illustrated in Figure 5-4), may appear to have been derived haphazardly. However, we note that this is simple model is exactly what comes from a more rigorous approach. The k-space distribution of noninteracting bosons in a harmonic trap, in the high temperature limit in which Maxwell-Boltzmann statistics apply, is given by the single particle density matrix for a harmonic oscillator. This may be written exactly as an ensemble of Gaussian pure states, incoherently averaged over their position x_0:

$$\begin{aligned}\langle k'|\hat{\rho}_{HO}(T)|k\rangle &= \frac{\sqrt{1+\tanh^2\frac{\hbar\omega}{2k_BT}}}{2\pi}\int dx_0\, e^{-\frac{M\omega}{2\hbar}x_0^2\coth\frac{\hbar\omega}{k_BT}} \\ &\quad \times e^{i(k-k')x_0}e^{-\frac{\hbar}{2M\omega}(k^2+k'^2)\tanh\frac{\hbar\omega}{2k_BT}} \\ &\xrightarrow[k_BT\gg\hbar\omega]{} \frac{1}{2\pi}\int dx_0\, e^{-\frac{x_0^2}{2R_T^2}}e^{i(k-k')x_0}e^{-\frac{1}{2}\lambda_T^2(k^2+k'^2)}.\end{aligned}$$

where $R_T = \sqrt{k_BT/M\omega^2}$ is the classical thermal size of a Maxwell-Boltzmann cloud in a harmonic trap of frequency ω. It is therefore appropriate to regard the thermal cloud as a collection of wave packets of gaussian width λ_T, distributed in space according to Maxwell-Boltzmann statistics[2].

5.2.3 Coherence length

It is also convenient to rephrase Equation 5.8 in the following way

$$C = \exp\left(-\frac{d^2}{2\,\ell_c^2}\right) \tag{5.9}$$

where we have defined a *coherence length* ℓ_c as

$$\ell_c = \frac{\lambda_T}{2\pi}\,\frac{\text{size in TOF}}{\text{size in trap}} \tag{5.10}$$

[2]I thank James Anglin for validating my *balls and springs* model.

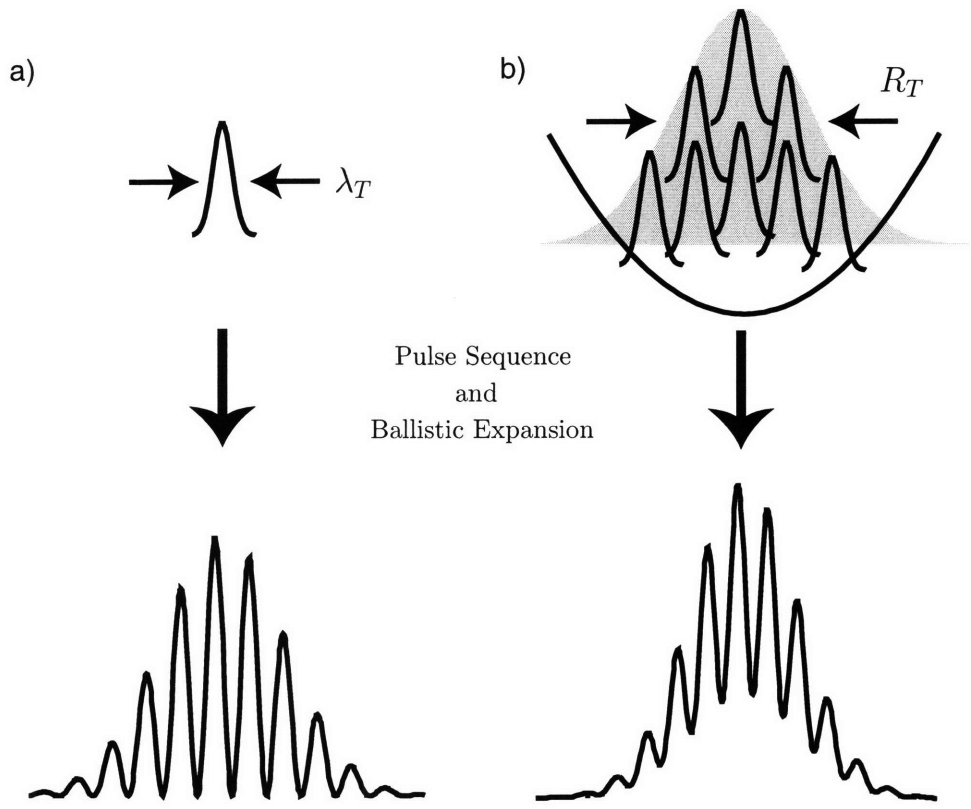

Figure 5-4: Reduced fringe contrast of a thermal cloud. a) The wavefunction of a single atom subjected to the autocorrelation Bragg pulse sequence is modulated with perfect contrast after expansion. b) The probability density of multiple thermal atoms add incoherently. An ensemble of single atom wavefunctions, of width λ_T, distributed over a trap with size R_T result in a fringe contrast less than unity (Equation 5.8).

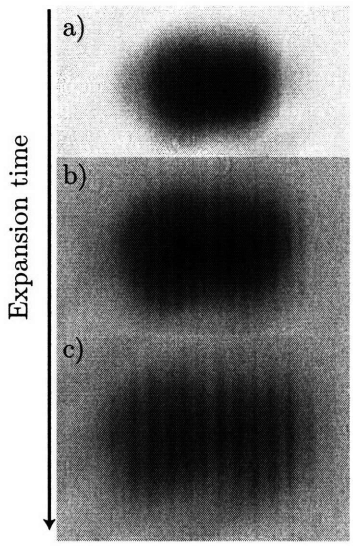

Figure 5-5: Contrast emerges in time of flight. The coherence length ℓ_c grows during expansion, and eventually exceeds the initial separation $d = 2\,\mu$m. Expansion time is a) 14 ms, b) 20 ms, and c) 25.

That is, the coherence length of an atom in the trap is λ_T, and contrast is lost when the separation d is larger than ℓ_c. However, during expansion, the local spread of momentum states decreases, and ℓ_c grows in proportion to the size of the cloud $ht/m\lambda_T$.

The implication is that we can always see interference from a thermal cloud, provided we give it enough expansion. In Figure 5-5 we show that interference which is imperceptible shortly after the cloud is released emerges in longer time of flight.

5.2.4 Ramsey Fringes

There is another framework for describing this experiment which I like, and that is to invoke the paradigm of Ramsey spectroscopy. In a Ramsey's method of *separated oscillatory fields*, two $\pi/2$ pulses are administered, separated by some wait time τ_w. The probability of being in the excited or ground state oscillates as a function of the wait time (or, equivalently, the phase of the field which induces the $\pi/2$ pulse). In the Bloch sphere picture, the first pulse rotates the Bloch vector up to the equator. During the wait time, the Bloch vector precesses, and a second pulse rotates the Bloch vector again. The projection onto the z-axis, and thus probability of being in one particular state, depends on how far it precesses azimuthally.

In this experiment, rather than varying τ_w or the relative phase of the pulses, we use a spread of momentum states. A momentum state $|\hbar k\rangle$ is coupled to $|\hbar(k + k_r)\rangle$, where k_r is

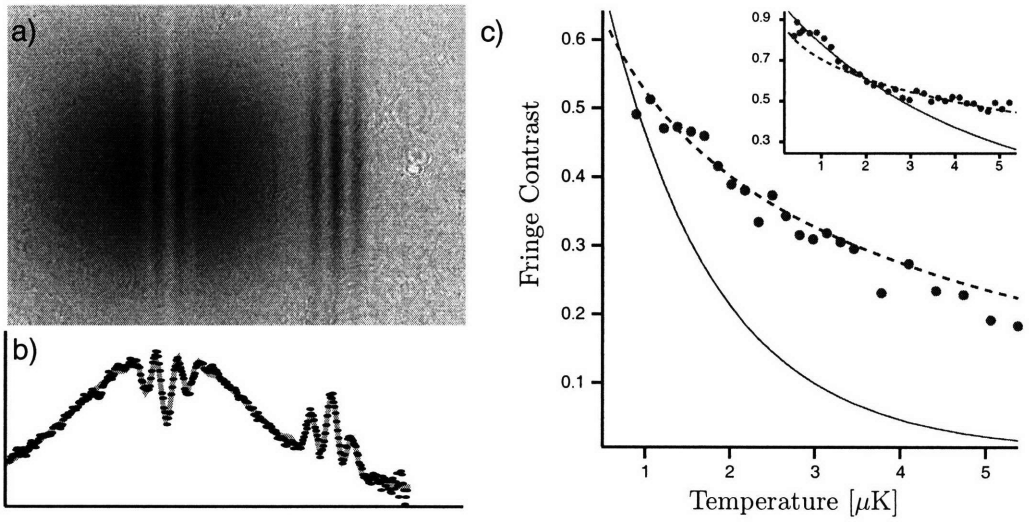

Figure 5-6: Fringe contrast for a *filtered* thermal cloud. A $\tau_w = 30\,\mu$s long Bragg pulse is used to out-couple a narrow slice of the available momentum states. a) An absorption image shows high contrast interference for this velocity subset with $\lambda_f = 170\,\mu$m. b) The integrated optical density is fit to extract a numerical value for the contrast C. c) Measured fringe contrast is found to exceed that predicted by Equation 5.8 (solid line). A model which introduces an effective de Broglie wavelength λ'_T (Equation 5.12) above an onset temperature T_0 follows the data (dashed line). This model is also applied to the $\tau_w = 10\,\mu$s pulse data from Figure 5-3: shown for $\lambda_f = 340\,\mu$m (inset).

the recoil momentum. The relative phase which accrues during τ_w is

$$\delta\phi = \frac{\hbar(k+k_r)^2}{2m}\tau_w - \frac{\hbar(k)^2}{2m}\tau_w = \frac{\hbar k_r \tau_w}{m}\,k + \frac{\hbar k_r^2 \tau_w}{2m} \tag{5.11}$$

where the last term is just a constant. In other words, the phase is linear in the initial momentum $\hbar k$. And since the cloud in time of flight reveals the in trap momentum distribution, the image is like a Ramsey fringe taken in one shot.

5.3 Momentum "Filtered" Interference

In Section 5.2.2 we discussed a simple model which could quantitatively describe the contrast of an interfering thermal cloud. At low temperature our model provides a very accurate description of the observed fringe visibility. At higher temperatures, however, the observed contrast is consistently greater than expected. One possible explanation for this behavior

is that our model fails when the Bragg pulses becomes velocity selective. At temperatures greater than some characteristic temperature T_0, the momentum spread $\hbar/\lambda_T$ will exceed the Fourier width of the Bragg pulses. Some momentum components are then excluded from the process. The Bragg coupling spans a range of $\delta p = \pi m/k_r\tau_p$. This implies an onset temperature $T_0 = \delta p^2/2mk_B$ for velocity selectivity. Indeed, for a $10\mu s$ pulse, we find $T_0 = 2.7\mu K$, which agrees with where the data begins to deviate from the theory curve.

In order to further investigate this possibility, we repeat the experiment at a longer pulse duration $\tau_p = 30\,\mu$s, which is more velocity selective. In Figure 5-6a, it is clear that we address a narrow range of momentum space. We must now account for the large background when fitting the cross section. While the fraction of atoms out-coupled falls with increasing temperature, the interference is still clearly visible. In fact, we find that the contrast (Figure 5-6c) is greatly enhanced over our simple theory (solid line).

The reason for this finding is not clear. Generally, one would not be surprised to find less coherence than expected, but to find *more* is striking. Perhaps this reflects a fault with the distribution in our single particle model, perhaps interactions play a role and a single particle model is insufficient. There is, however, no obvious weakness in our treatment. In the following Section, we describe a phenomenological model which does a pretty good job of following the data, but should be taken with a very large grain of salt.

5.3.1 Phenomenological Model for Enhanced Contrast

When data is found to follow some completely unexpected trend, the inclination is to find a model which describes this trend. This Section is the result of such an effort.

We found that the fringe contrast of an interfering thermal cloud was significantly enhanced when we *filtered* the sample, by using longer Bragg pulses. Since this implies a narrowed region of momentum space, correspondingly our atoms may be considered to have a larger effective de Broglie wavelength, and thus a larger coherence length. We can qualitatively introduce the effective de Broglie wavelength

$$\lambda'_T = \frac{\hbar}{\sqrt{2Mk_B}}\,(T\,T_0)^{-1/4} \tag{5.12}$$

If we use λ'_T in our description of the coherence length (Equation 5.10), we predict a contrast which agrees remarkably well with the data. In Figure 5-6c, we show this prediction (dashed

line) for both the long Bragg pulses, as well as the short pulses (inset) discussed earlier. When we allow the power of T and T_0 to vary as a free parameter in the fitting (i.e. $\left(T^{\alpha} T_0^{1-\alpha}\right)^{1/2}$) we find that Equation 5.12 is a good guess ($\alpha \simeq 0.53$).

5.4 Conclusion and Outlook

In this chapter we have explored the coherence properties of a thermal cloud of atoms. Under the appropriate conditions, a thermal sample can exhibit high contrast interference, analogous to a white light interferometer. Bose-Einstein condensation is not a precondition for obtaining an interference signal which may be applicable for a number of measurements. This, however, is a single particle effect. Unlike two BECs, two independent thermal clouds will not interfere with each other.

Chapter 6

Degenerate Fermions in an Optical Lattice

Strongly interacting Fermi gases have emerged as a new frontier where atomic physics and condensed matter physics overlap. The study of these quantum gases in the presence of an optical lattice may yield important insight into the nature of superconductivity in crystalline materials. The tools of atomic physics present a degree of control unavailable in solid state systems, offering a promising test bed for theoretical models which have sought greater verification for decades, as well as the opportunity to explore exciting new phenomena which are uniquely atomic.

This chapter supplements work reported in the following publication:

J.K. Chin, D.E. Miller, Y. Liu, C. Stan, W. Setiawan, C. Sanner, K. Xu and W. Ketterle *"Evidence for Superfluidity of Ultracold Fermions in an optical lattice,"*

Nature 443, 961 (2006).

(Included in Appendix C) Ref [24]

I was in a bar, in Knoxville, when I received an ecstatic phone call from the lab. From what I could make out, my labmates had just seen the first interference pattern of a fermion pair condensate released from a 3D optical lattice, conveniently, while I was away for the DAMOP conference. Over the following weeks we would complete what was to be the first paper of the newly refurbished machine, a triumph which was celebrated with a champagne toast at a 10 A.M. group meeting, following a sleepless night in the lab. In this Chapter, I will discuss these results, as well as some which were not featured in this publication. The Ph.D. thesis of Jit Kee Chin will provide a far more comprehensive account of this experiment.

6.1 The signature of superfluidity

There is almost no limit to the phenomena which can be studied in an optical lattice. To name just a few, experiments have demonstrated Bloch oscillations [97] and fermionic antibunching [98], whereas the phenomena anti-ferromagnetic order [111] and d-wave superfluidity [56] remain on the horizon. It was our goal to achieve superfluidity in a 3-D optical lattice. The signature for superfluidity, with some technical qualifications, is the appearance of sharp interference peaks at the reciprocal lattice vector, after expansion.

Despite our lab's extensive experience with loading Na into an optical lattice [114, 115], and a healthy Li pair condensate[1], the first signal proved elusive. When released from the lattice, the cloud appeared heated. However, if the lattice was adiabatically ramped down before the trap was switched off we regained a condensed sample. It soon became apparent that collisions between the discrete momentum components were the culprit. In an atomic BEC this effect manifests as the s-wave collision halo, visible in Figures 3-2 and 3-3. For a strongly interacting Fermi gas, however, the collisional cross section is much larger. Secondary and higher order collisions become appreciable, and the sample looks isotropically heated. The solution was to cut the magnetic field as quickly as possible, reducing interactions, before turning off the optical lattice. Figure 6-1 illustrates the effects of collisions at different magnetic fields. We found that keeping the lattice on for an additional 150 μs as the field is ramped was sufficient to ameliorate the effect of collisions.

In Figure 6-2, we show a schematic of of the imaging geometry which details the pro-

[1] the preparation of which is detailed in Chapter 4

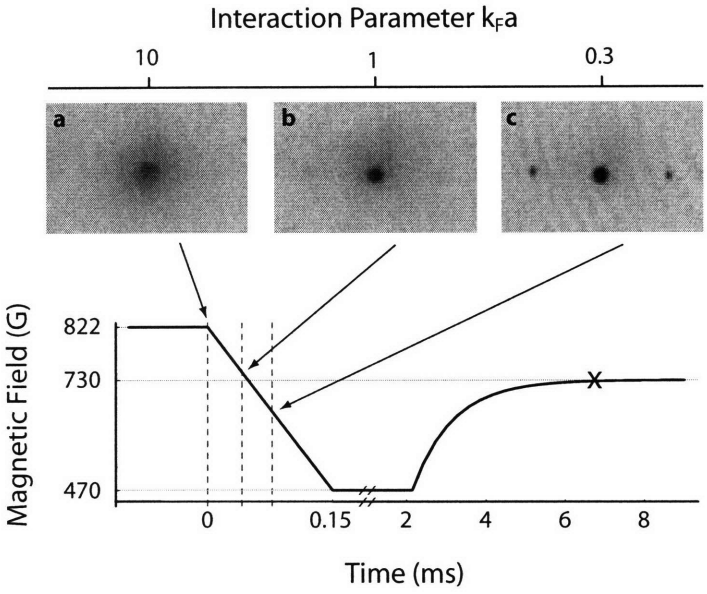

Figure 6-1: Dissipative collisions between momentum components. A Li pair condensate is prepared at 822 G. The magnetic field is cut abruptly when the cloud is released from the trap. As a probe of the scattering cross section σ, a short Kapitza-Dirac pulse is administered at different times during the field ramp, corresponding to magnetic fields (a) 822 G, (b) 749 G and (c) 665 G. The absorption images reveal different degrees of heating due to collisions between the discrete momentum components. For a sufficient reduction of the interaction parameter $k_F a$, and therefore the scattering cross section, the distinct momentum peaks are visible.

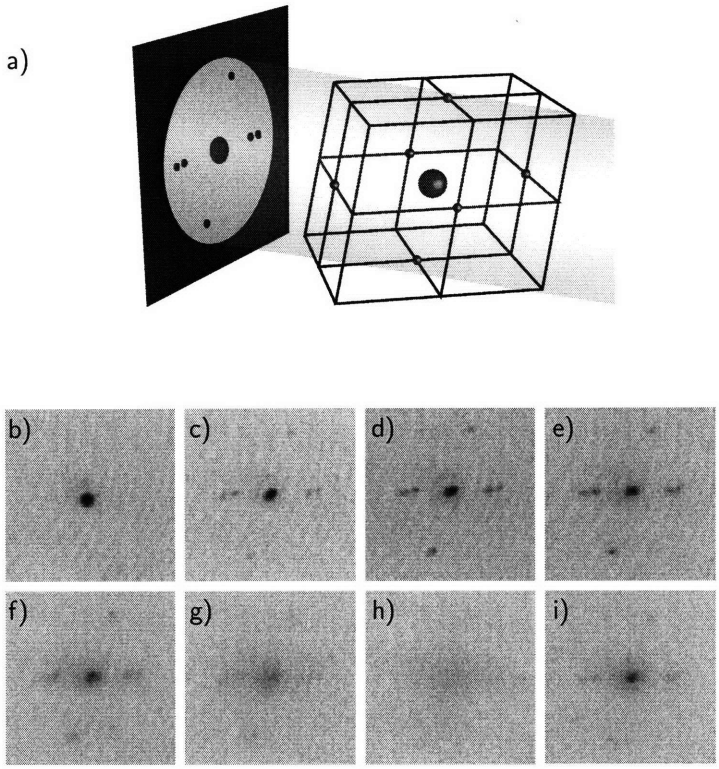

Figure 6-2: Interference of fermion pairs released from an optical lattice. a) Schematic of the imaging geometry, detailing the projection of the reciprocal lattice onto the imaging plane. (b-i) Absorption images of fermion pairs at a field of 822 G, released from varying lattice depths V_0. Values of V_0 are b) 0 E_r, c) 2.5 E_r, d) 4 E_r, e) 5 E_r, f) 6 E_r, g) 7 E_r and h) 9 E_r. i) The interference pattern is resurrected for a cloud which is ramped up to 10 E_r, and then back down to 2.5 E_r before being released.

jection of reciprocal lattice onto the imaging plane. We also show time of flight images for a pair condensate released from an optical lattice of varying depth. The sharpness of the interference peaks, with respect to their separation, provides an upper bound for the coherence length of ten lattice sites [42]. This neglects broadening mechanisms, such as the mean field energy. For deeper lattices, the interference pattern is replaced by a broad gaussian, a possible indication of an insulating state, which we discuss in the following Section.

6.2 The insulator state

Let us consider a sample of bosonic atoms in an optical lattice. In the superfluid state, the atomic wavefunction is delocalized across lattice sites. In expansion, the wavefunction at each lattice site acts as a coherent source, which adds up to produce the familiar interference

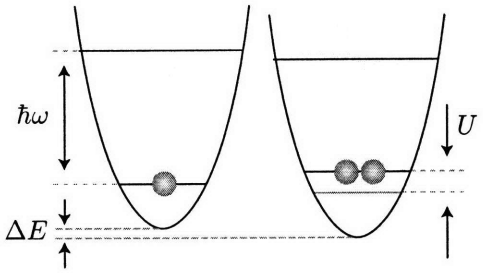

Figure 6-3: Individual lattice sites can be approximated as harmonic oscillators with energy spacing $\hbar\omega$. For repulsive interactions, there is an energy cost U for two atoms to occupy the same lattice site. The application of a potential gradient results in an energy difference ΔE between sites. For a conducting state, this will result in current. An insulating state, however, will not respond.

pattern. This delocalization implies an uncertainty in where an atom will be found, and therefore an uncertainty in the number of atoms which will be found on a particular lattice site. The occupation number of each lattice site is given by a Possionian distribution. There is an energy "J" associated with this delocalization, referred to as the tunneling energy.

For an interacting gas, this number uncertainty has a cost. A state in which two (or more) atoms can be found at the same lattice site must pay the interaction energy U, which is positive for repulsive interactions. If the cost of interaction U exceeds the benefit of delocalization J, it becomes energetically favorable for each atom to find its own lattice site and stick to it. This is known as the Mott insulator state [46], in which the wavefunction at each lattice site is described by a Fock state: a fixed atom number at each site. This certainty in number, however, corresponds to an uncertainty in the phase between adjacent sites, which washes out the interference pattern, leaving only a blurred gaussian cloud in expansion.

The ratio U/J can be increased with the lattice depth V_0. It is a characteristic feature of the Superfluid-Mott insulator transition [45] (SF-MI) that the interference pattern is lost as the lattice depth is increased and U/J exceeds some critical value. Because the Mott insulator is the ground state, lowering the lattice can adiabatically convert the system back into a superlfuid state, restoring coherence. There are some subtleties in the interpretation of the interference pattern [42, 35]. There do exist, however, other methods to more accurately identify the Mott insulator transition [3, 86].

Fermions

We turn now to the system at hand: a spin mixture of strongly interacting fermions in an optical lattice. In Figure 6-2, we observe the disappearance of the interference pattern with

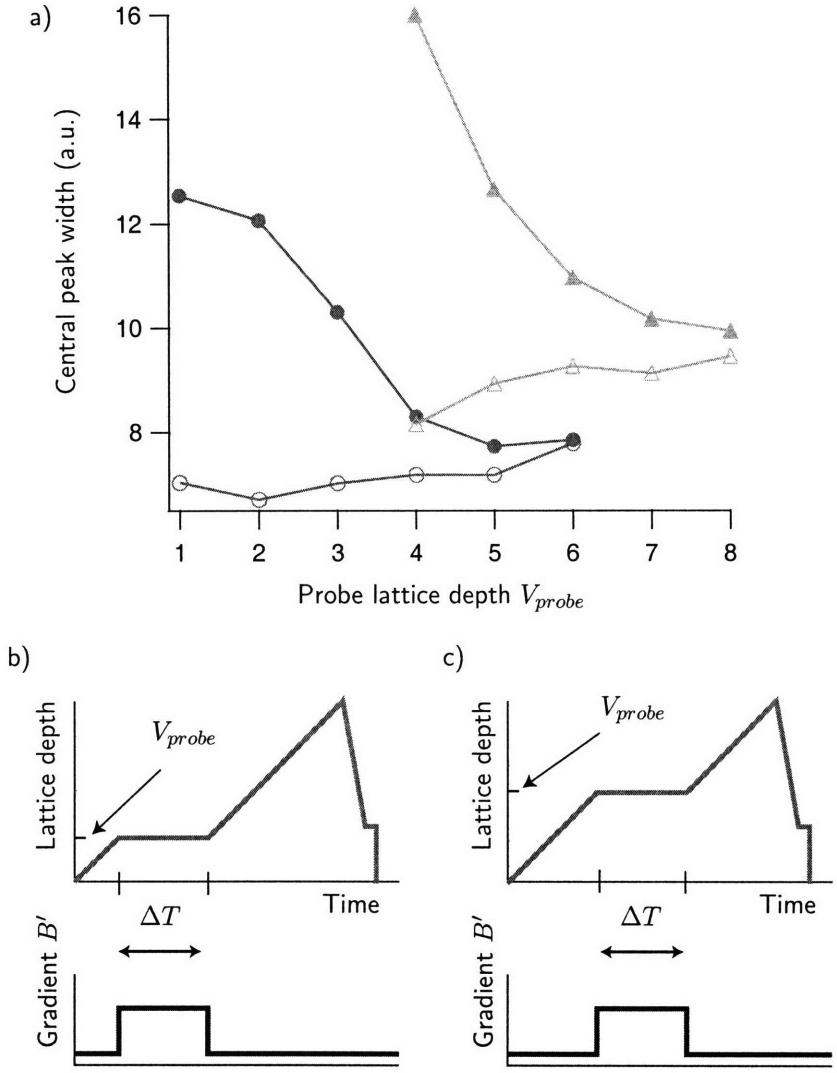

Figure 6-4: Excitation of a superfluid Fermi gas in a lattice. Starting with a pair condensate at 822 G, we ramp a 3-D optical lattice up to $V_0 = 8\,E_r$, then back down to $2\,E_r$, where it is held for 150 μs before release. The ramp up is interrupted at a particular value V_{probe} for a time ΔT, during which magnetic gradient of $B' = 4$ G/cm may be applied. A schematic of the ramp sequence for different values of V_{probe} is given in (b) and (c). After expansion, the gaussian width of the central momentum peak is used as a measure of coherence. (a) The measured width is shown as a function of the lattice depth V_{probe} at which the gradient is applied (filled markers). For comparison, the ramp sequence is repeated without the applied gradient (open markers). As V_{probe} is increased, the excitation effect of B' is reduced, perhaps indicating an insulating state. The depth V_{probe} at which this insulating behavior is observed varies with the hold time ΔT (10 ms and 30 ms; circles and triangles, respectively).

increasing lattice depth, as well as its restoration when the lattice is subsequently lowered. This behavior is qualitatively consistent with the superfluid-insulator transition described in the previous Section. However, one must be careful in our treatment of this pair condensate. While the pairs do in some respect behave as composite bosons, at some level the nature of the constituent fermions must play a role. In particular, the interaction energy U is not likely to be valid, insofar as we have defined it. The Pauli exclusion principle requires that pairs on the same lattice site be in orthogonal states, and the relevant "interaction" energy may be the harmonic oscillator spacing $\hbar\omega$. In this case, the single band model is no longer sufficient.

6.2.1 Insulating Behavior

While our description of the Mott-insulator is not strictly applicable to a unitary Fermi gas, the concepts are still relevant. Just as BEC superfluidity evolves continuously into BCS superfluidity in the BEC-BCS crossover, so the Mott insulator is expected to evolve into its counterpart, the band insulator [119]. While a comprehensive study of insulating behavior throughout the BEC-BCS crossover has yet to be performed, we have made some preliminary measurements.

The application of a potential gradient results in an energy difference ΔE between adjacent lattice sites. In a conducting state, neighboring sites accrue a phase difference, resulting in a current. Nonlinear effects can randomize this phase across the sample, broadening the interference pattern in time of flight. On the other hand, the phase between adjacent lattice sites in a Mott insulator state is completely uncertain, rendering any accrual of relative phase meaningless. An insulator is not excited by a gradient, and can therefore be converted back into a superfluid, producing a sharp interference pattern in expansion.

The excitation spectrum of the Mott insulator does, however, exhibit resonances. An excitation gap opens up for $\Delta E = U$, due to the creation of particle-hole pairs. This excitation gap has been measured for a BEC in the Mott insulator state [45]. The width of the central peak in time of flight was used as a measure of excitation. At low V_0, the superfluid is uniformly excited as a function of ΔE. At deeper V_0, however, excitation is only observed at distinct values of ΔE, indicative of a Mott insulator.

Technical limitations precluded the replication of this experiment with our Li gas. Our pinch coils produce a gradient of 0.4 G/cm, per 1 A of current. This corresponds to a

$\Delta E = h \times 20$ hz, across lattice sites[2]. (For comparison, the pull of gravity is equivalent to a magnetic gradient of 2 G/cm.) For our strongly interacting system, we do not expect to open an excitation gap until the gradient is on the order of the harmonic oscillator spacing $\hbar\omega$ of the lattice, which is tens of khz.

We did, however, study the excitation of our system in response to a fixed gradient, as we varied the lattice depth. Figure 6-4 shows the response to an applied gradient, as a function of V_0. At low lattice depths, the central peak width is significantly broadened, indicating excitation, whereas for deeper lattices the effect of the gradient is negligible. This would seem to indicate insulating behavior. However, the depth V_0 above which the width is not affected appears to be dependent on the duration ΔT of the applied gradient. This may be an effect of inhomogeneous density, and requires further study.

6.3 Recoherence

The field ramp technique which we employ (Figure 6-1), in order to reduce the collision cross section, raises a question: Are we actually probing the physics at the initial magnetic field? We may wish to infer from the sharp interference peaks in the time of flight images that the sample was coherent. However, is it possible that this coherence is established during the 150 μs field ramp? After all, the interactions are very strong, which may imply a short time scale for such an effect.

In order to address this question, we study the timescale on which coherence can be reestablished. A lattice is adiabatically ramped up to 8 E_r; a depth at which the interference pattern is essentially absent. The lattice depth is subsequently ramped down to 2.5 E_r over a variable ramp-down time τ, and held for 150 μs during the magnetic field ramp, before release. Again the width of the central peak is used as a measure of coherence. In Figure 6-5, the narrowing of the central peak shows that coherence is restored on a relatively short time scale of ~ 500 μs, indicating that the sample remains in the ground state during the application of the lattice. This is on the order of the single-particle tunneling time h/J for a $V_0 = 2.5E_r$ lattice. While the 150 μs duration of the field ramp is not completely negligible in comparison, we can conclude that the interference pattern we observe is indicative of the coherence of the sample at the original field.

[2] $1.4\frac{mhz}{G} \times 0.4\frac{G}{cm} \times \frac{0.5}{\sqrt{2}}\mu m$, where the $\sqrt{2}$ reflects the 45° orientation of the lattice with respect to the pinch coil axis.

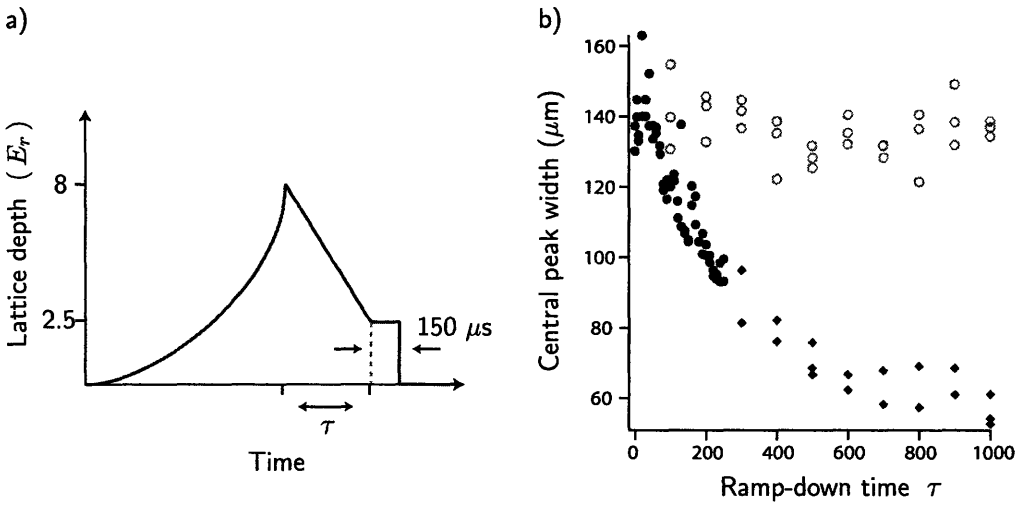

Figure 6-5: Restoring coherence from a deep lattice. a) The lattice is adiabatically ramped up to $V_0 = 8\,E_r$. A sample released from a lattice of this depth does not exhibit interference. In order to study the time scale on which coherence can be reestablished, we ramp V_0 down to 2.5 E_r over a variable ramp time τ. The sample is held here for 150 μs, while the magnetic field is ramped down, before release. b) As a measure of coherence, the widths of the central peak after 6.5 ms expansion, obtained from a gaussian (bimodal) fit, are plotted as solid circles (diamonds), as a function of τ. The fast time scale over which coherence is restored indicates that the sample stays in the ground state during the application of the lattice. A sample which has been decohered (open circles), through the application of a magnetic gradient during the lattice ramp-up, does not regain coherence under the same conditions.

Additionally, we can study a system which is not in the ground state. If we apply a magnetic gradient during the ramp up of the lattice, we can excite the sample. Such a dephased cloud will not recohere for any experimentally accessible ramp times. This illustrates the difference between a dephased sample and a ground state with phase uncertainty, and demonstrates that any recoherence, due to evaporative cooling for example, is negligible during the field ramp.

6.4 Conclusion and Outlook

In this chapter we discussed some of the first findings resulting from the loading of a superfluid Fermi gas into a 3D optical lattice. The future has much in store for this system. The search for anti-ferromagnetic order and d-wave superfluidity will occupy much of the coming research agenda. Degenerate Fermi gases are likely to produce a tremendous amount of insight into the workings of strongly correlated many-body quantum systems.

Chapter 7

Critical Velocity in the BEC-BCS Crossover

The flow of a current without dissipation has intrigued physicists since Kamerlingh-Onnes' discovery of superconductivity in 1911. Since then, the realm of superfluidity has expanded to include liquid helium, and more recently cold atomic gases, and comes in both bosonic and fermionic flavors. The nature of superfluidity can be understood as a consequence of collective excitations, which modify the free particle dispersion relation so as to render flow below a critical velocity dissipationless. Above the critical velocity, the current suffers an energetic (Landau) instability, resulting in excitations. Superfluid atomic Fermi gases offer the unique opportunity to study the transformation between bosonic superfluidity, such as in ^4He, to fermionic superfluidity, as in ^3He.

This chapter supplements work reported in the following publication:

D. E. Miller, J. K. Chin, C. A. Stan, Y. Liu, W. Setiawan, C. Sanner and W. Ketterle *"Critical velocity for superfluid flow across the BEC-BCS crossover,"*
preprint condmat/0707.2354 (2007).
(Included in Appendix D) Ref [28]

7.1 The Landau criterion

While superfluidity is, in essence, a quantum mechanical phenomena, we need nothing more than high-school mechanics to arrive at a fairly satisfying explanation of its origin. Consider an object of mass m moving with velocity $\vec{v}_0$ through a stationary fluid at zero temperature. The object may create an excitation in the fluid with momentum $\vec{p}$ and energy $E(p)$. This has the effect of damping the object's motion, reducing its velocity to $\vec{v}$. Conservation of energy gives us

$$\tfrac{1}{2}mv_0^2 = \tfrac{1}{2}mv^2 + E(p) \tag{7.1}$$

whereas conservation of momentum gives

$$m\vec{v}_0 = m\vec{v} + \vec{p} \tag{7.2}$$

From these conditions we find

$$\vec{p}\cdot\vec{v}_0 = \frac{p^2}{2m} + E(p) \ . \tag{7.3}$$

This is just another way of saying that, in the frame moving at v_0, the work done by the fluid is equal to the energy of the fluid excitation plus the kinetic energy transferred to the object. If we recognize that $\vec{p}\cdot\vec{v}_0 \leq p\,v_0$, and consider an object of very large mass, we see that excitations are only possible for

$$v_0 \geq \frac{E(p)}{p} \ . \tag{7.4}$$

This is the Landau criterion, which establishes a critical velocity for dissipation

$$v_c = \min E(p)/p \ . \tag{7.5}$$

For motion below this velocity, viscosity will be absent, and the flow is superfluid.

The complicated part, of course, is in the determination of the dispersion relation $E(p)$, which is where quantum mechanics enters the picture. The quadratic free particle dispersion $E(p) = p^2/2m$ gives a critical velocity of zero, i.e., no superfluidity. Collective excitations, however, can produce a more interesting dispersion relation, such as the one pictured in Figure 7-1. The Landau criterion may be depicted graphically as finding the line of the shallowest slope which passes through the origin and is tangent to $E(p)$. The slope of this

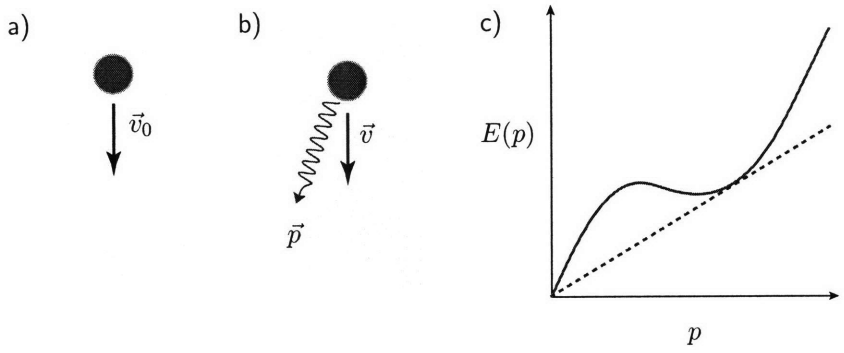

Figure 7-1: The Landau criterion for superfluidity. (a) An object passing through a fluid with velocity v_0 can (b) create an excitation in the fluid with momentum p. As a result, the motion is damped, reducing the velocity to v. Conservation of energy and momentum place a lower bound on the velocity for which excitations can occur, known as the Landau criterion (Equation 7.4). (c) This critical velocity, $v_c = \min E(p)/p$, can be depicted graphically as the slope of a (dashed) line which is tangent to the dispersion relation $E(p)$ (solid line).

line is the critical velocity.

Energetic instability

In general, we can calculate the energy spectrum of excitations by considering small perturbations to the ground state. A Landau instability develops when the energy of an excitation with some wavevector k becomes negative. The system can lower its energy by incorporating elementary excitations. In this way, we refer to dissipation above the Landau threshold as an *energetic* instability. For a superfluid, the energy of the system is a local minimum, and it is stable against small perturbations. Above the critical velocity, however, the superfluid flow lies at an energetic saddle point and is unstable [113].

7.1.1 Phonon excitation spectrum

In Chapter 2.1.6 we introduced the Bogliubov excitation spectrum, which describes the elementary excitations for a BEC. From Figure 2-2, it is clear that, according to the Landau criterion, the critical velocity is given by the speed of sound. The sound velocity was found to be

$$c = \sqrt{\frac{4\pi\hbar^2 a}{m^2} n} \ . \qquad \text{(BEC)} \qquad (7.6)$$

This is, of course, a specific case of a more general thermodynamic relation. The hydro-

dynamic description [57, 109, 81] is based on the continuity equation

$$\frac{\partial}{\partial t}n + \nabla(n\vec{v}) = 0 \tag{7.7}$$

and the Euler equation

$$m\frac{\partial}{\partial t}\vec{v} + \nabla\left[\mu(n) + \tfrac{1}{2}mv^2\right] = 0\,, \tag{7.8}$$

where $\vec{v}$ is the velocity field. Together, they produce a wave equation for small density perturbations, which travel at the speed of sound.

$$c = \sqrt{\frac{n}{m}\frac{\partial\mu}{\partial n}} \tag{7.9}$$

In the case of a two-component Fermi gas in the deep BCS limit ($1/k_F a \rightarrow -\infty$) the sound mode equivalent is known as the Bogoliubov-Anderson mode [53, 44]. Here, the gas behaves essentially as a noninteracting Fermi gas. Equation 2.9 tells us that $\mu \propto n^{2/3}$, from which it follows that

$$c = \frac{v_F}{\sqrt{3}} \qquad \text{(BCS)} \tag{7.10}$$

Figure 7-2 illustrates the evolution of the speed of sound throughout the BEC-BCS crossover [26, 53]. On the BEC side, c increases gradually with increasing interactions. This trend continues monotonically until c reaches the noninteracting Fermi gas limit $v_F/\sqrt{3}$. We can solve for the speed of sound on resonance using the chemical potential for a zero temperature universal Fermi gas (UFG) which we derived in Equation 2.16.

$$c = \frac{v_F}{\sqrt{3}}\,(1+\beta)^{1/2} \qquad \text{(UFG)} \tag{7.11}$$

A recent experiment at Duke [65] has measured the propagation of sound in an elongated superfluid Fermi gas across the BEC-BCS crossover, using a technique first implemented here at MIT [5] in which a far detuned laser creates a density perturbation which then travels down the sample. From the measurements on resonance, the universal parameter β was determined to be -0.570, in good agreement with other experimental measurements and theory [44].

7.1.2 Pair-breaking excitation spectrum

For a gas of superfluid Fermion pairs, phonons are not the only type of excitation which contribute to the Landau instability. Pair-breaking excitations may also contribute to dissipation. The solution of the Bogoliubov-de Gennes equation [31] gives the excitation spectrum

$$E(p) = \sqrt{\left(\frac{p^2}{2m} - \mu\right)^2 + \Delta^2} \tag{7.12}$$

The pairing gap Δ represents the minimum energy required to create a single particle excitation, and thus break a pair. At unitarity, it is on the order of the Fermi energy. In the BCS limit, the gap falls off exponentially with $(k_F a)^{-1}$, indicating the fragile nature of the BCS superfluid.

The critical velocity for these single particle excitations is, according to the Landau criterion,

$$v_{sp} = \left(\frac{\sqrt{\Delta^2 + \mu^2} - \mu}{m}\right)^{1/2} . \tag{7.13}$$

7.1.3 The Landau criterion in the BEC-BCS crossover

A simple estimate of the critical velocity in the crossover is given by the minimum velocity of these two loss mechanisms.

$$v_c = \min\left(c, v_{sp}\right) \tag{7.14}$$

In Figure 7-2, we see that this intersection yields a pronounced maximum near resonance. The critical velocity also defines a generalized healing length

$$\xi = \frac{\hbar}{m\, v_c} . \tag{7.15}$$

In the BEC limit this was given by Equation 2.4, and related to the speed of sound. In the BCS regime, it corresponds to the size of Cooper pairs.

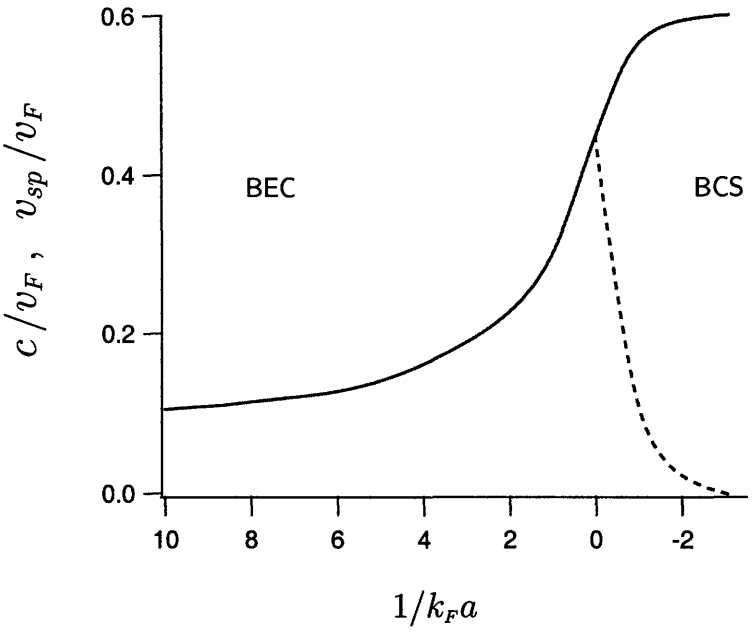

Figure 7-2: Speed of sound and pair-breaking threshold in a two-component Fermi gas. The speed of sound c (solid line) increases monotonically across the BEC-BCS crossover. The threshold velocity v_{sp} for pair-breaking falls exponentially in the BCS limit. The Landau critical velocity is given by the minimum velocity of these two, and is sharply peaked near resonance. Adapted from [26].

7.2 Measuring dissipation in a quantum gas

In this section we will review some of the previous experiments which have measured the critical velocity in an atomic BEC, as well as introduce the techniques we employed in our studies of a superfluid Fermi gas.

7.2.1 Stirring a BEC

Appropriately enough, the first measurements of critical velocity in a BEC were performed in the New Lab, by Chandra Raman and Roberto Onofrio [92, 89, 93]. In these experiments, a blue detuned beam (split off from the Argon ion laser which used to pump the dye laser) was used to stir a magnetically trapped BEC, as illustrated in Figure 7-3a. The beam was passed through an AOM, and the pointing could be controlled dynamically by changing the driving frequency. The stirring beam was scanned back and forth, along the long axis of the condensate, heating the sample. A bimodal fit to the expanded cloud produced a calorimetric measure of the heating. As a function of the stirring velocity, the heating rate showed an abrupt onset at some critical velocity $v_c \simeq 0.1\,c$, where c was the speed of sound calculated at the peak density of the condensate. This value of v_c was obtained by considering a drag force $F = \kappa\,(v - v_c)$, where κ is the drag coefficient [61, 41], which transfers energy to the system at a rate

$$\frac{dE}{dt} = F \cdot v = \kappa\, v\,(v - v_c) \ . \tag{7.16}$$

Such a small value of v_c/c may come as a surprise, based on our previous discussion of the Landau criterion. There are, however, a number of effects in this experiment with act to reduce v_c. The first is a purely geometrical concern. In the case of an impenetrable stirring object, the fluid must flow around the perimeter. Therefore, the actual velocity of the fluid is faster than that of the stirrer [41]. The second correction we must make is to account for the inhomogeneous density of the sample [62]. One may expect that the local speed of sound depends on the local density, which decreases towards the edge of the cloud. In such a case, there should be no sharp onset of dissipation, since the stirring beam pierces through a region were the density, and therefore, the critical velocity goes to zero. The MIT experiment did, however, observe an abrupt onset, and it turns out that the proper treatment of the density inhomogeneity is more complicated than we have let on.

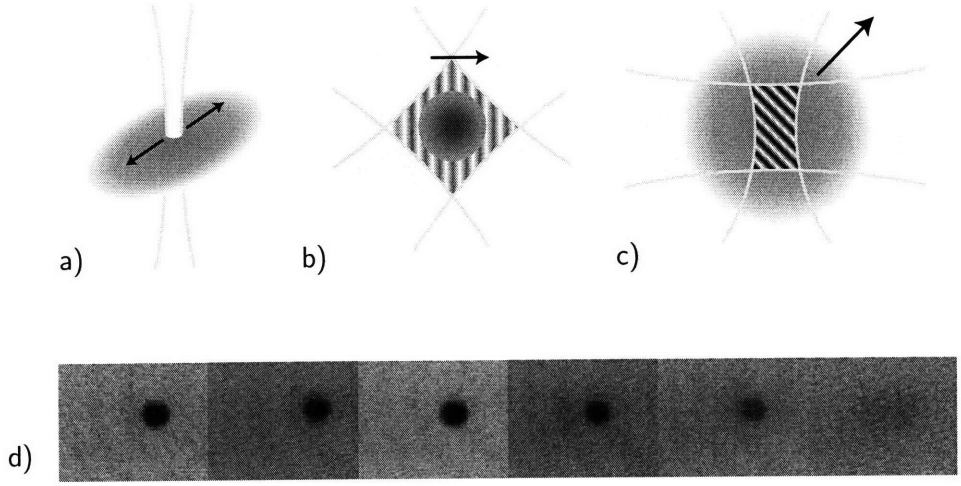

Figure 7-3: Various configurations for perturbing a condensate. a) A single far-detuned laser beam is focused at the center of an elongated cloud. The beam is scanned back and forth. b) *Uniform lattice*: Two intersecting laser beams with some frequency difference produce a moving optical lattice. An atomic sample is confined in the center, experiencing a relatively homogeneous lattice depth. c) *Centered lattice*: Two intersecting laser beams are focused to a size smaller than the trapped cloud, producing a moving optical lattice which probes a relatively homogeneous region of density. Trapping potentials (optical or magnetic) are not shown. The arrows indicate the direction of motion. d) Absorption images of a pair condensate subject to a lattice moving with increasing velocity (left to right) show an abrupt threshold for dissipation.

We will find that accounting for density inhomogeneity will be a recurring theme in such experiments.

7.2.2 BEC in a moving lattice

Similar experiments were conducted in Florence, in which a 1D optical lattice was used to perturb the system, rather than a stirring beam. The conclusions reached, however, were rather different. In the initial experiment [14], the BEC was displaced in the harmonic trap and set to oscillate. A more controlled experiment was performed later, in which the lattice was moved at a constant velocity [32]. The Florence group observed a gradual increase in dissipation with velocity, which saturated at a particular value. In their interpretation, the critical velocity is given by the local speed of sound. The lattice velocity v then sets some threshold density n_{th}, for which the speed of sound is $c(n_{th}) = v$. For a given velocity, the

fraction of the cloud which is below this threshold density experiences loss, while the rest is immune. When the lattice velocity exceeds $c(n_p)$, at the peak density n_p, the entire sample will incur dissipation, and the loss is flat with respect to v.

The behavior at low velocities, however, was not studied in detail. It is difficult to exclude the possibility of an abrupt onset of dissipation, such as that which was found in the MIT experiment. Additionally, the suggestion that the loss reaches a plateau seems difficult to reconcile with most models of friction, which are velocity dependent, as in Equation 7.16. The presence of a dynamical instability, which we introduced in Chapter 3.5, greatly limits the range of velocity over which the loss appears constant. In addition, lifetime data in this same paper does not show the same plateau as the condensate number.

The Florence group has also shown that thermal atoms participated in the loss process. For these experiments, the atomic sample was held in a magnetic trap. The application of an "RF-shield" prevented the accumulation of a thermal component as the condensate was heated by the moving lattice. The lifetime of shielded cloud was shown to exceed that of the unshielded cloud by an order of magnitude, at velocities below the threshold for dynamical instability. This strongly suggests that the loss they observe at low velocities is due, at least in part, to the collision of thermal *impurities* with the condensate; a finding which will guide the interpretation of our own data in the following Sections.

7.2.3 Superfluid Fermi gas in a moving lattice

In our determination of the critical velocity in a superfluid Fermi gas, we also study the dissipation induced by a moving 1D optical lattice. There are two lattice geometries that are used, which are shown in Figure 7-3, the experimental details of which are given in Chapter 4.4.1. In the first, the lattice beams extend to cover the entire trapped sample. The lattice depth is then fairly uniform across the pair condensate. The density which we probe, however, is not. In a second configuration, the lattice beams are focused down to a size smaller than the trapped cloud, sampling only the center of the cloud where the density is relatively homogeneous. In both cases, we observed a threshold velocity for dissipation, as shown in Figure 7-3d. In the following Sections we describe how we parameterized the loss signal, and how it was interpreted in the context of Landau instability.

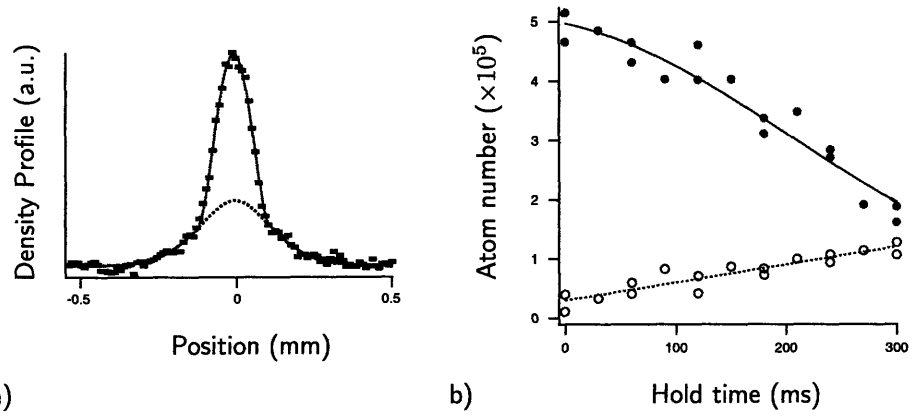

Figure 7-4: Dissipation in a moving lattice. a) A bimodal fit of the density profile, after 17 ms expansion, provides a measure of the heating incurred in the moving lattice. b) The number of pairs in the thermal component N_{th} (open circles) and those remaining in the condensate N_c (filled circles) as a function of the time held in the moving lattice. The thermal component grows approximately linearly (dashed line), whereas N_c is fit to model (solid line) in which the loss is proportional to N_{th} (Equation 7.18).

7.3 Uniform lattice / inhomogeneous density

The first system we studied was that of the *uniform lattice*, depicted in Figure 7-3b. After the preparation of a pair condensate, near resonance, the optical lattice is adiabatically ramped up, moving with a fixed velocity. The lattice is kept on for a duration up to 2 s. After the lattice is ramped off, we allow the cloud to expand, ramping the magnetic field as usual to preserve the momentum distribution [121].

From a bimodal fit to the density distribution, we extract the number of condensed pairs N_c, as well as the number in the thermal component N_{th}. Figure 7-4b shows the temporal dynamics of the dissipation (which is characteristic of both lattice configurations used). Atoms which are excited from the pair condensate either escape the optical trap or contribute to the thermal fraction. In order to quantify the loss, we first use a linear loss model.

$$N_c(t) = N_0 (1 - \gamma t) \tag{7.17}$$

In Figure 7-5, we interpret the dissipation through the linear loss fit parameter $\gamma(v)$. The loss at low velocities is essentially zero, whereas above some critical velocity there is a kink, and the loss rate increases sharply.

Furthermore, we study the loss on both sides of the resonance. Before the lattice is

brought up, we adiabatically ramp the magnetic field to probe the sample at the desired value of $k_F a$. We find that the superfluid is most robust near resonance, in that the onset of dissipation occurs at the highest velocity. This velocity is, however, quite small: about an order of magnitude smaller than the speed of sound $c \simeq 19$ mm/s, as calculated by Equation 7.11. We attribute this discrepancy to the inhomogeneous density of the cloud. The speed of sound which we have quoted is that at the trap center, i.e. for the peak density. As the density falls off radially, so does the local speed of sound. It is interesting, then, that we see a discontinuity in the loss rate at all. After all, the lattice probes the outer edges of the cloud, where the density approaches zero.

This observation, however, is not inconsistent with the M.I.T. stirring experiments [92, 93] which probed regions of vanishing density, as well. The propagation of sound in an elongated degenerate Fermi gas [18, 65] also discredits the simplistic portrait of a *local* speed of sound. Axially propagating wavefronts do not distort in accordance with the radially decreasing density profile. Rather, they remain flat, in apparent defiance of the local sound velocity. In fact, the concept of a *local* speed of sound may not even be valid in the outer wings of the cloud, at least insofar as we have defined it. The local density approximation, which we have invoked, fails at the outer boundary of the cloud, where the density can not be considered slowly varying.

In any case, it is clear that accounting for the inhomogeneous density is a messy affair. This is what motivated us to use a different lattice geometry, in which only the central region of the cloud was probed. I will address these results in a later Section, but before doing so, I would like discuss the temporal dynamics of the loss process.

7.3.1 Loss dynamics

Figure 7-4b offers a characteristic portrait of the loss dynamics. We chose to parameterize this data in terms of a linear loss model (Equation 7.17), which was adequate for identifying the sharp onset of loss. Yet, this was merely a convenient choice which lacked any physical motivation, and it is interesting to speculate upon the nature of the dissipation so as to construct a more robust model.

In Section 7.2.2 we discussed an experiment which provided evidence for the participation of thermal atoms in the dissipation of an atomic BEC in a moving lattice. We have seen evidence that the thermal component plays a similar role in our fermionic system. We

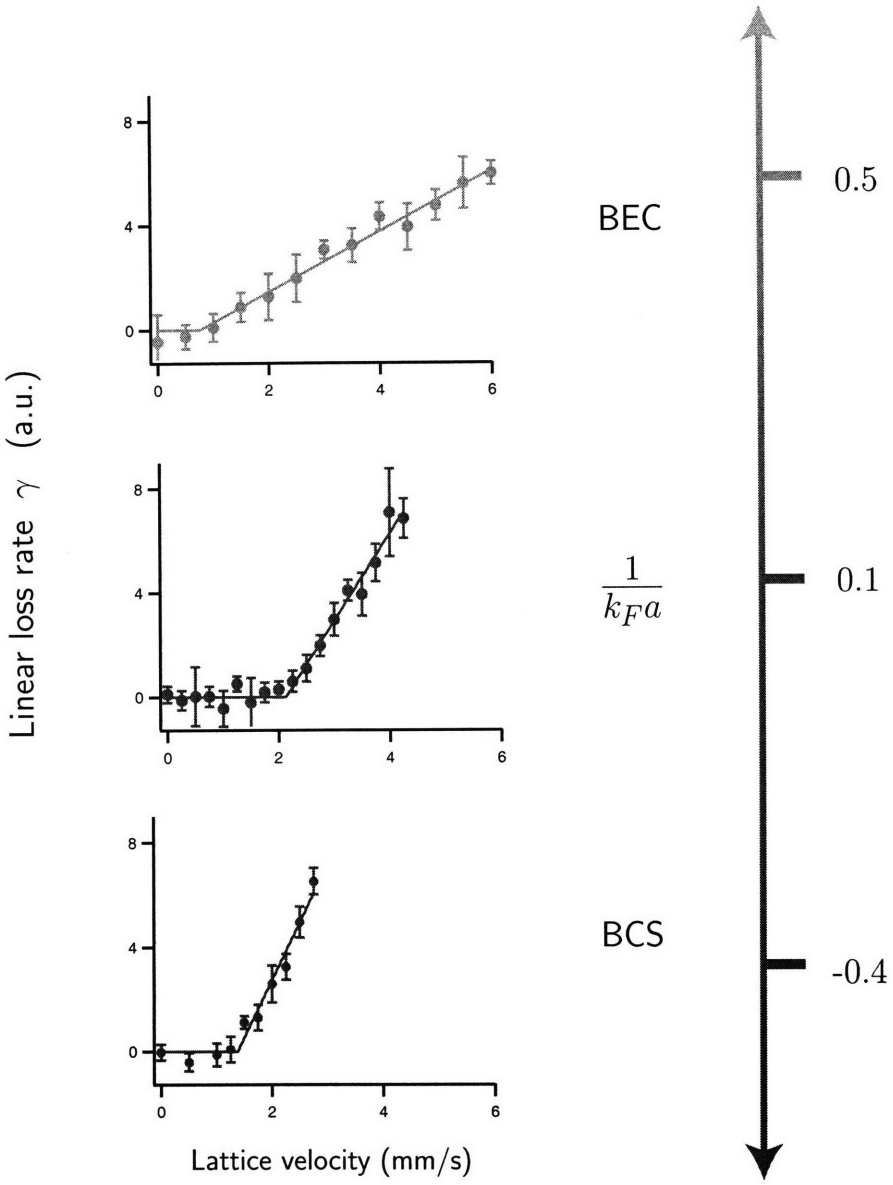

Figure 7-5: Abrupt onset of dissipation. The time series of loss is fit with a linear function (Equation 7.17), which characterizes the dissipation at a given lattice velocity by a linear loss rate γ. We see a sharp kink in the loss behavior at some critical velocity. The loss is studied throughout the BEC-BCS crossover, and indicates a critical velocity which is greatest near resonance.

can prevent the accumulation of a thermal component during exposure to the lattice by gradually reducing the trap depth from U_0 to some final value U_{min}, allowing the heated pairs to evaporate. We find that the lifetime is enhanced by at least a factor of two over that of a sample held in a fixed trap, at either U_0 or U_{min}. An experiment with greater control over the temperature would certainly shed more light. Unfortunately, the use of an optical trap does not permit the variation of the trap depth independently of the trapping frequencies, and therefore the density of the sample.

Nevertheless, our finding supports a picture of dissipation which is driven by the collision of thermal impurities with the condensate. This may suggest a model of an exponential loss

$$N_c(t) = N_c(0)\, e^{-\Gamma t} \quad , \tag{7.18}$$

in which the loss rate $\Gamma = \gamma_0 N_{th}$ is proportional to the number of thermal atoms N_{th}. In Figure 7-4 we apply this fitting function, where we have approximated the thermal component as growing linearly in time. This model satisfactorily describes a loss which is faster than linear, consistent with our observation. Impurities in the form of unpaired atoms would allow us to better test the validity of this model. Unfortunately, phase separation effects [102] make controllably varying the population imbalance difficult for our geometry.

A dissipation which is driven by thermal impurities is also more consistent with the threshold behavior we observe. The lattice potential itself should only provide a matrix element between momentum states differing by h/λ_L. This would result in a loss which is resonant, centered at a lattice velocity $v = 22$ mm/s, corresponding to the Bragg resonance. Rather, we observe a threshold behavior. If the loss is driven by thermal impurities which are dragged along by the lattice [71], the matrix element is essentially a point source which can couple to excitations at all wavevectors. This type of coupling can be used as a probe for Landau instability.

7.4 Centered lattice / homogeneous density

The obvious shortcomings in a system of inhomogeneous density motivated us to adopt a lattice configuration in which only the central region of the cloud is probed (Figure 7-3c). This arrangement also yielded a threshold for loss. In the previous Section, we extracted a loss rate from the temporal behavior, a process which is both data intensive and model

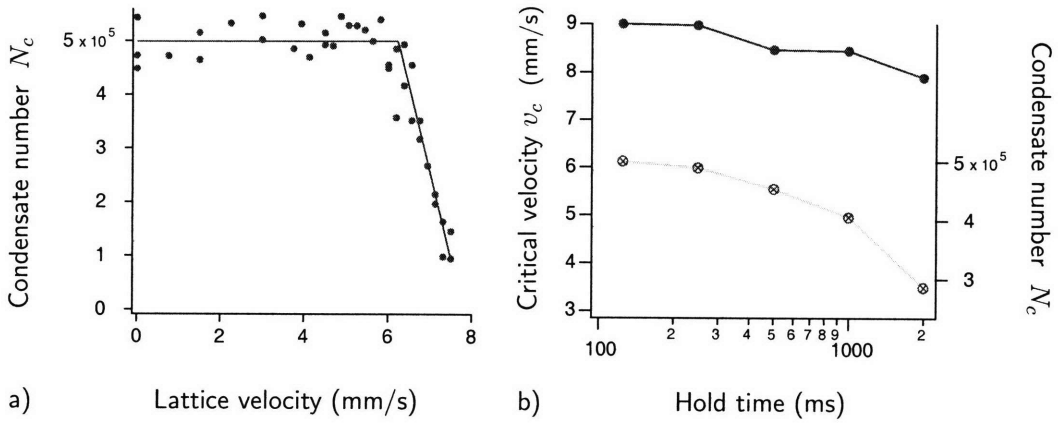

Figure 7-6: Critical velocity at the cloud center. a) Number of pairs which remained in the condensate N_c after being subjected to a $V_0 = 0.2\,E_F$ deep optical lattice for 500 ms, moving with velocity v_L, at a magnetic field of 822 G ($1/k_F a = 0.15$)) An abrupt onset of dissipation is observed above a critical velocity v_c, which we identify from a fit to Equation 7.19. b) The critical velocity we obtain (filled circles) is weakly dependent on the time held in the lattice (logarithmic scale). Some of this variation may in fact be attributed to the reduction in numbers, and therefore speed of sound, due to the sample's finite lifetime. We show N_c as a function of hold time in a stationary lattice (crossed circles).

dependent. Here we identify the critical velocity from a trace taken for a single exposure time in the lattice. In Figure 7-6a, we show the number of condensed pairs remaining as a function of lattice velocity v_L. We define the critical velocity v_c from a fit to the intersection of two lines.

$$N_c(v) = N_c(0) \times [\,1 - max(0, \alpha \times (v - vc))\,] \tag{7.19}$$

As we show in Figure 7-6b, this approach gives a fairly consistent value over a large range of hold times. Longer hold times do consistently point to a somewhat smaller v_c. Some of this effect, however, may be due to the reduced numbers at long hold times. In a stationary lattice (or without a lattice at all) the total number will decay substantially over 2 s. This has the effect of reducing the density, and thus the speed of sound.

7.4.1 Critical velocity throughout the BEC-BCS crossover

We repeat this measurement of the critical velocity at different magnetic fields, as shown in Figure 7-7. We find that v_c is maximum near resonance, falling off precipitously on the BCS side and more gradually on the BEC side. This behavior is consistent with the model for Landau instability which we discussed in Section 7.1.3. On the BEC side, the critical

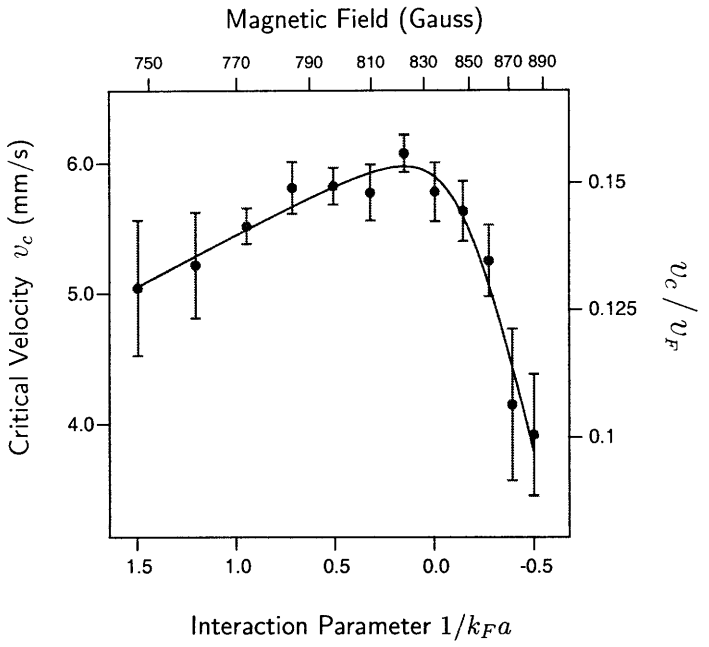

Figure 7-7: Critical velocity throughout the BEC-BCS crossover. The value of v_c at each magnetic field is obtained from a fit to Equation 7.19, as shown in Figure 7-6. The critical velocity falls off gradually on the BEC side along with the speed of sound, and more sharply on the BCS side due to pair breaking. Data is shown for a $V_0 = 0.2\,E_F$ deep lattice, held for t=500 ms.

velocity is determined by the speed of sound, whereas on the BCS side it is given by the pair breaking threshold.

While this data is in qualitative agreement with such an understanding, there are still some quantitative issues which need to be resolved. As most theory papers discuss homogenous systems, or equivalently work in the local density approximation, it is most convenient to reference the local Fermi velocity (see Equation 2.19) at the trap center

$$v_F = (1+\beta)^{-1/4}\sqrt{2E_F/m} \tag{7.20}$$

The (non-interacting) Fermi energy for this system is $E_F = h \times 7.6$ khz. The corresponding Fermi velocity is then $v_F = 39$ mm/s.

In terms of the Fermi velocity, the speed of sound is $c_s = 0.37\, v_F$, according to Equation 7.11. The pair breaking threshold, given by Equation 7.13, is $v_{sp} = 0.34\, v_F$, where we have used $\Delta = 0.50\, \varepsilon_F$ [19, 20]. These two values should provide a good estimate of the critical velocity on resonance, although our measurements appear to come up short. If we are to make a quantitative comparison with theory, we need to address the effects of a finite lattice potential.

7.4.2 Critical velocity at different lattice depth

Numerical simulations for both a BEC [58] and a superfluid fermi gas [103] have shown that the Landau criterion provides an upper bound for the critical velocity which is attained only in the limit of vanishing perturbing potential. While the lattice does reduce the speed of sound [73], through the effective mass, this effect is insignificant for the lattice depths we explore. Rather, nonlinear corrections to the Bogoliubov spectrum [84] are expected to play a role. In Figure 7-8, we explore the critical velocity near resonance ($1/k_F a = 0.15$) over a large range of lattice depths. In the limit of low lattice depth, v_c converges to $v_c^{peak} \approx 0.25\, v_F$. Measurements at the smallest lattice depths became more uncertain as the hold time required to observe an effect of the lattice approached the natural lifetime of our sample. It is for this reason that we studied the field dependence (Figure 7-7) at an intermediate lattice depth where v_c was more well defined. Nevertheless, the value we obtain for v_c^{peak} near resonance is within 10% of the predictions. Extrapolation between the pair breaking and collective excitation branches may reduce the effective v_c. Any additional

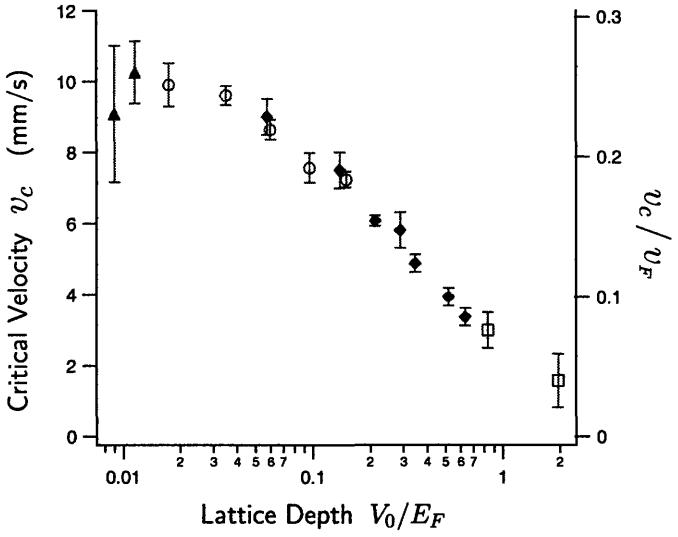

Figure 7-8: Critical velocity at different lattice depths. The results show v_c to be a decreasing function of lattice depth V_0. In the limit of low V_0, v_c converges to a maximum value of 0.25 v_F. Data was taken near resonance, at 822 G ($1/k_F a = 0.15$) for hold times t = 250 ms, 500 ms, 1000 ms, 2000 ms (squares, diamonds, circles, triangles).

discrepancy which we observe may be attributed to the density variation across the lattice.

7.4.3 Dynamical instability

While we have framed our results in the context of an energetic instability, there exist other loss mechanism which may occur in a moving lattice. A dynamical instability, which we introduced in Chapter 3.5, occurs when two particles from the condensate collide and scatter into states with opposite momentum $\pm\delta k$. The lattice modifies the dispersion relation so that this process becomes energetically possible when condensate has a certain momentum in the lattice frame. Our results, however, are not consistent with the simple understanding of a dynamical instability, which can not set in below 0.5 q_B, corresponding to $v = 11$ mm/s, where $q_B = h/2\lambda_L$ is the Bragg momentum which defines the edge of the Brillouin zone. The highest critical velocity observed, in the low V_0 limit, is just below this threshold (see Figure 7-8). However, v_c falls rapidly for increasing V_0. Recently it has been shown [86] that strong interactions can lower the threshold for dynamical instability, reaching zero at the Mott Insulator transition. However, it is very likely that the range of lattice depths explored here ($V_0 \leq 2\,E_r$) are too shallow to exhibit this effect. The loss of coherence which typically accompanies the superfluid to Mott insulation transition was found to occur at $V_0 \simeq 6\,E_r$ in a 3-D optical lattice [24]. We have observed that coherence persists in a 1-D lattice up to $V_0 \simeq 25\,E_r$. For these reasons, we rule out the role of dynamical instability in the dissipation which we observe.

7.5 Bragg spectroscopy in the BEC-BCS crossover

In the previous sections we discussed using a 1D moving lattice to probe excitations at all wavevectors, through collisions with thermal impurities. Such a lattice can also be used to study excitations at a single wavevector, given by the spatial period of the lattice. In Figure 3-8 we saw that Bragg diffraction could impart a quantity (two photons worth) of momentum unto either a single atom or bound diatomic molecule. Distinguishing between the two was straightforward as for a molecule the doubled mass halves the recoil energy and recoil velocity. The molecular Bragg resonance occurs at half the frequency of the atomic peak. It is interesting to ask what happens to the spectrum when we can tune continuously between these two cases, i.e. in the BEC-BCS crossover. We have taken some preliminary

data to address this question.

Traditionally, in Bragg spectroscopy , one relies on the out-coupled fraction which appears in time of flight, as in Figure 3-2c, for a signal. This is not possible in the strongly interacting regime, because the distinct momentum component collide violently as the pass one another. However, after collisions, a small out-coupled fraction manifests as a protuberance, and the width of the expanded cloud can be used as a measure of the Bragg diffraction efficiency.

Figure 7-9 we show Bragg spectra taken throughout the crossover. On the BEC side, we observe a peak corresponding to the Bragg scattering of molecules. As we move towards the BCS limit, the peak shifts towards the atomic resonance, but also broadens significantly. This may be related to a broad pair breaking feature such as that observed in Ref. [21]. This interesting behavior certainly warrants greater attention. In particular, one may wish to vary the recoil energy with respect to E_F (by changing the angle of the Bragg beams, perhaps).

7.6 Conclusion and Outlook

In this chapter we have explored the limits of superfluidity in the BEC-BCS crossover. The technique we use may find application in identifying superfluidity in other systems, such as degenerate Fermi gases in lower dimensions. The role of the thermal component, as well as a greater understanding of the dissipation mechanism, in general, requires further investigation.

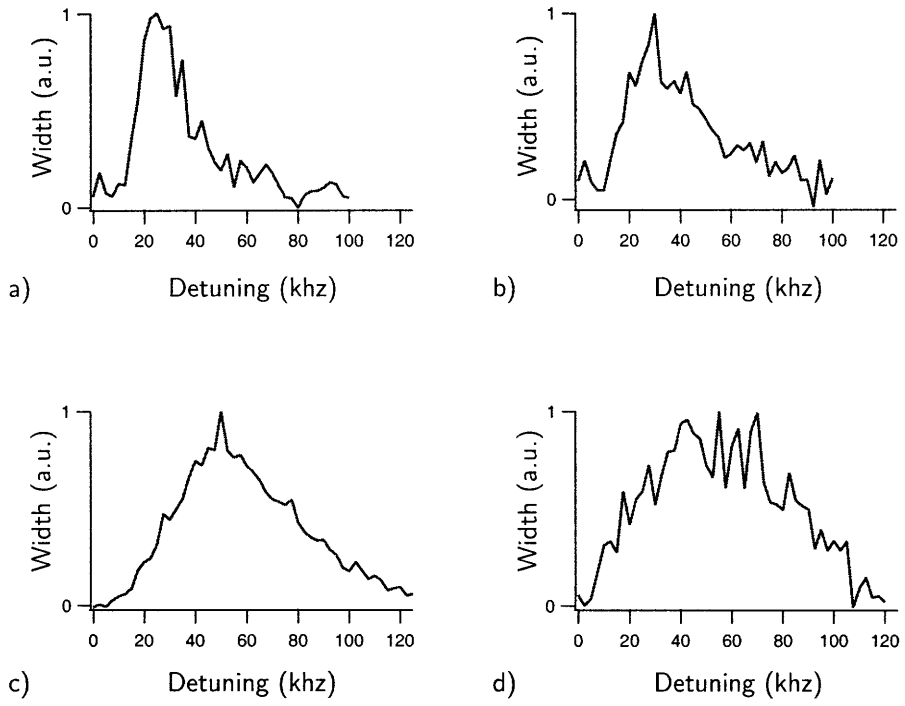

Figure 7-9: Bragg spectroscopy in the BEC-BCS crossover. Strong collisions prevent the identification of the out-coupled fraction as a signal. Rather, the width of the cloud in expansion, which is distorted due to the collisions, provides a measure of the Bragg diffraction efficiency. The Fermi energy is $E_F = h \times 12.4$ khz. The recoil energy for a pair is $E_r = h \times 7.3$ khz. Measurements of the BEC side of the resonance, at a) 750 G and b) 820 G, show a peak at the molecular resonance $h\,\delta\nu = 4\,E_r$. On the BCS side of the resonance, at c) 890 G and d) 960 G, the spectra shift towards an atomic resonance, in which the Bragg process breaks a pair and the momentum is carried by a single atom. The resolution, given by the finite pulse duration, is 3.5 khz.

Epilogue

"I don't want to achieve immortality through my work ...
I want to achieve it through not dying."
- Woody Allen

After five years, and countless late nights in the lab, I can attest to the incompatibility of these two aims. Graduate school has been a remarkable experience; one of great intensity and freedom. I have been extremely fortunate to have had this opportunity to have rubbed elbows with some brilliant individuals, to have witnessed a number of impressive milestones in the advancement of science, and to have played my own small role in this great theater.

Appendix A

High-contrast Interference in a Thermal Cloud of Atoms

D. E. Miller, J. R. Anglin, J. R. Abo-Shaeer, K. Xu,
J. K. Chin, and W. Ketterle
"High-contrast interference in a thermal cloud of atoms,"
Phys. Rev. A 71, 043615 (2005).

High-contrast interference in a thermal cloud of atoms

D. E. Miller, J. R. Anglin, J. R. Abo-Shaeer, K. Xu, J. K. Chin, and W. Ketterle*
Department of Physics, MIT-Harvard Center for Ultracold Atoms,
and Research Laboratory of Electronics, MIT, Cambridge, Massachusetts 02139, USA
(Received 23 December 2004; published 29 April 2005)

The coherence properties of a gas of bosonic atoms above the Bose-Einstein-condensation transition temperature were studied. Bragg diffraction was used to create two spatially separated wave packets, which interfere during expansion. Given sufficient expansion time, high fringe contrast could be observed in a cloud of arbitrary temperature. Fringe visibility greater than 90% was observed, which decreased with increasing temperature, in agreement with a simple model. When the sample was "filtered" in momentum space using long, velocity-selective Bragg pulses, the contrast was significantly enhanced in contrast to predictions.

DOI: 10.1103/PhysRevA.71.043615 PACS number(s): 03.75.Hh, 34.20.Cf, 32.80.Pj, 33.80.Ps

Images of interfering atomic clouds are widely considered a hallmark of Bose-condensed systems and a signature of long-range correlations [1]. A thermal atomic cloud is often regarded as an incoherent source, with a coherence length too short to obtain high-contrast interference patterns when two clouds are overlapped. Here we show that ballistic expansion can increase the coherence length such that "Bose-Einstein-condensation-type" ("BEC-type") interference can be observed in a thermal cloud. Currently, there is considerable interest in characterizing the coherence properties of noncondensed systems including ultracold fermions [2], fermion pairs [3–5], and ultracold molecules [6–8]. In this paper we show that an interferometric autocorrelation technique, previously only applied to condensates [9,10], can be used to study the coherence properties of samples at finite temperature.

We studied the first-order spatial coherence of a trapped thermal cloud of atoms. After release from the trap, the atom cloud expanded ballistically, and Bragg diffraction was used to create an identical copy of the initial cloud displaced by a distance d. Therefore, our study was analogous to Young's double-slit experiment [11]. We investigate the conditions under which two such overlapping clouds produce a high-contrast interference pattern. Our result is that for sufficiently long expansion times, there will always be high contrast, but the required time of flight becomes longer at higher temperatures.

The experiment used a magnetically trapped thermal cloud of $\sim 5\times 10^7$ sodium atoms, prepared in a manner similar to our previous work [12]. Atoms in the $|F=1,m_F=-1\rangle$ state were loaded from a magneto-optical trap (MOT) into a magnetic trap, where they were further cooled by radio frequency (rf) evaporation. The rf evaporation was stopped before the critical temperature for Bose-Einstein condensation, T_c, was reached, yielding a thermal cloud at a controlled temperature. Shortly after being released from the trap (2 ms), the cloud was exposed to two successive Bragg pulses, separated by wait time τ_w. The effect of the Bragg beams [13,14] was to couple two momentum states $|\hbar\mathbf{k}_0\rangle$ and $|\hbar(\mathbf{k}_0+\mathbf{k}_r)\rangle$ via a two-photon transition, where $\mathbf{k}_r=(\mathbf{k}_1-\mathbf{k}_2)$ and $\mathbf{k}_1$, $\mathbf{k}_2$ are the wave vectors of the two Bragg beams. The coupling-induced Rabi oscillations and the pulse area were experimentally chosen to correspond to $\pi/2$ (i.e., an atom originally in a well-defined momentum state was taken to an equal superposition of the two states). During the wait time τ_w the two states accrued different phases before a second $\pi/2$ pulse mixed the states again. Considering only two momentum states, this is equivalent to Ramsey spectroscopy [15] (see Fig. 1).

One can regard a thermal cloud as an ensemble of atoms, each having its initial amplitude spread over a range of momentum states centered about zero, with rms width h/λ_T, where $\lambda_T=h/\sqrt{mk_BT}$ is the thermal de Broglie wavelength and m the atomic mass. The relative detuning of $\delta\nu=45$ kHz between the Bragg beams and pulse duration $\tau_p=10$ μs were chosen to couple all initial momentum components to those centered at $\mathbf{k}_r$. During τ_w the relative phase accumulated between coupled states is proportional to k_0, and the momentum distribution shows a sinusoidal modulation (Ramsey fringes) after the Bragg sequence. In long time of flight (TOF), the spatial density simply mimics this momentum distribution. Interference fringes were observed at a spacing $\lambda_f=ht_{\mathrm{tof}}/md$, where

$$d=v_r(\tau_w+4/\pi\tau_p) \tag{1}$$

is the cloud separation discussed in the equivalent picture of two overlapping clouds. v_r is the two-photon recoil velocity. The factor of $4/\pi$ emerges from a simple Rabi oscillation model and includes the extra phase accumulated while the Bragg beams effect a $\pi/2$ pulse. The sum of single-particle interference patterns results in a density along the x direction with reduced contrast C:

$$n(x)=f(x)\left[1+C\sin\left(\frac{2\pi}{\lambda_f}x+\phi\right)\right], \tag{2}$$

where $f(x)$ is an envelope function.

To find the expected contrast we consider the k-space distribution of noninteracting bosons in a harmonic trap assuming the high-temperature (Maxwell-Boltzmann) limit. This may be written exactly as an ensemble of single-particle

*Website: cua.mit.edu/ketterle_group

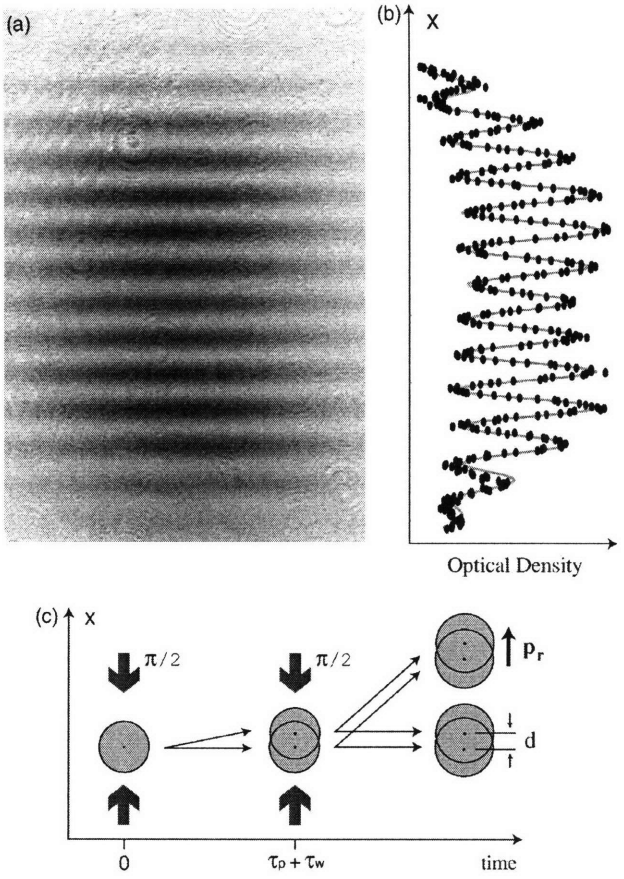

FIG. 1. Interference of spatially separated thermal clouds: (a) An absorption image, taken after 48 ms time of flight, shows fringes with a spatial period of $\lambda_f = 340$ μm. (b) A cross section of the optical density (black circles) taken through the center of the image was fit (gray line) to extract the fringe contrast. (c) Schematic depiction of the Bragg pulse sequence. The first $\pi/2$ pulse at $t=0$ created a superposition of stationary and moving clouds. At $t=\tau_p + \tau_w$ the clouds had separated by distance d, and a second pulse created a superposition of cloud pairs: one pair moving with recoil momentum $\mathbf{p}_r$, the other stationary. Each pair developed an interference pattern.

Gaussian states, incoherently averaged over their positions. Thus, it is appropriate to regard the thermal cloud as a collection of wave packets of Gaussian width λ_T, distributed in space according to Maxwell-Boltzmann statistics.

The incoherent sum over all particles results in contrast

$$C = \exp\left(-\frac{2\pi^2 R_T^2}{\lambda_f^2}\right) = \exp\left(-\frac{d^2}{2\ell_c^2}\right), \tag{3}$$

where $R_T = \sqrt{k_B T/m\omega^2}$ is the thermal size of a cloud in a harmonic trap of frequency ω and where we have defined the coherence length as

$$\ell_c = \frac{\lambda_T}{2\pi}\frac{\text{size in TOF}}{\text{size in trap}}. \tag{4}$$

Equation (3) gives two different, but equivalent criteria for the loss of contrast. While the interference pattern of a single-particle quantum state (as well as that of a pure condensate) should always show perfect contrast, the incoherent sum over a thermal cloud washes out the fringe visibility. Contrast is lost when the single-particle interference pattern is smeared out over an initial size R_T that is larger than the fringe spacing λ_f. However, because the fringe spacing grows as the cloud expands, contrast will always emerge with enough time of flight. Alternatively, Eq. (3) states that interference is lost when the separation d of the two sources exceeds the coherence length ℓ_c. Here it is important to note that the coherence length increases with time of flight [Eq. (4)]. The coherence length is inversely proportional to the local momentum spread which decreases in ballistic expansion as atoms with different velocities separate from each other. For very long expansion times, the coherence length becomes arbitrarily large resulting in high-contrast interference (Fig. 2). This can also be understood by the conservation of local phase-space density during ballistic expansion, where the decrease in density is accompanied by a decrease in momentum spread.

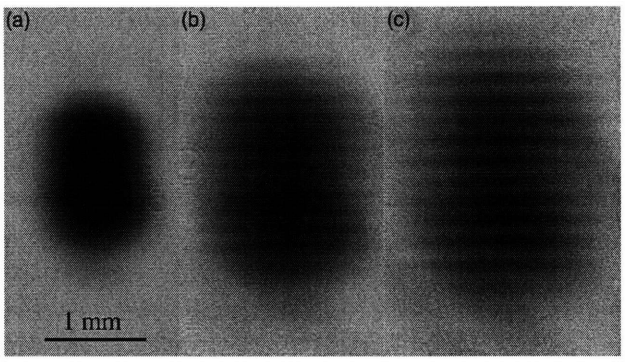

FIG. 2. Emerging contrast during ballistic expansion. The coherence length ℓ_c grew larger than the initial separation $d=2$ μm as the cloud expanded for (a) 14 ms, (b) 20 ms, and (c) 25 ms [see Eq. (4)].

We repeated the experiment over a range of temperatures for several values of the cloud separation d. The temperature was controlled by varying the final value of the rf evaporation. Each temperature was calibrated by measuring the size of a cloud in expansion without pulsing on the Bragg beams. The temperature calibration was consistent with the observed onset of BEC at the calculated temperature of $T_c = 0.6$ μK. The Bragg beams were detuned 30 GHz from the atomic transition and heating was demonstrated to be negligible by observing the effects of the light with the two-photon detuning $\delta\nu$ set far from the Bragg resonance. Absorption images of our samples were taken after 48 ms time of flight [Fig. 1(a)]. A cross section of the atomic density was fit to Eq. (2) to determine the contrast. Deviation of the pulse area from $\pi/2$ reduces the number of atoms in the out-coupled cloud; however, it does not reduce the contrast assuming the two pulses are equal.

Figure 3(a) shows the measured fringe contrast of the out-coupled cloud as a function of the cloud temperature for three different fringe spacings λ_f. The data are compared to the contrast expected from Eq. (3) (dashed line) with no free parameters. At low temperature this equation provides an

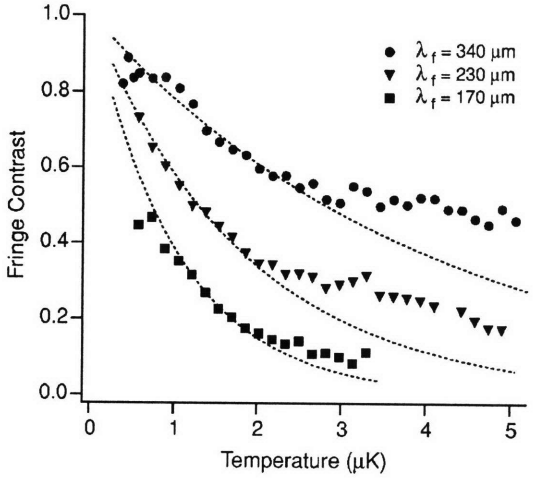

FIG. 3. Contrast vs temperature for 10-μs Bragg pulses. Different fringe spacings λ_f were realized by varying the wait time τ_w between the two Bragg pulses. The time of flight was kept fixed at 48 ms. At lower temperatures the observed contrast agreed well with theory (dashed lines) given by Eq. (3). At higher temperature, however, the contrast was higher than predicted, owing to the velocity selectivity of the Bragg pulses. The BEC transition temperature was at T_c=0.6 μK.

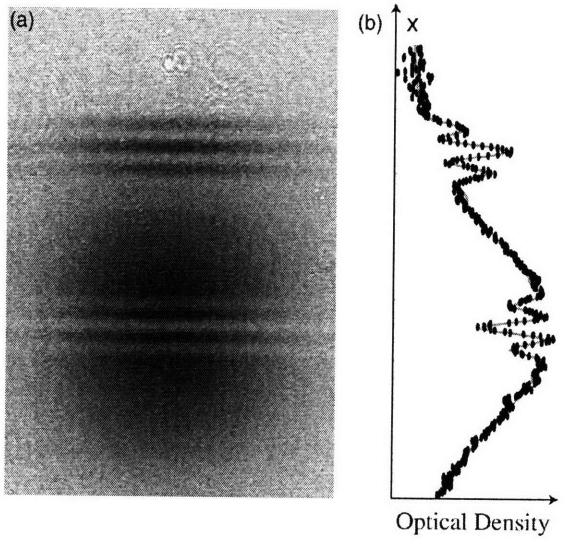

FIG. 4. Velocity-selective Bragg diffraction: (a) Absorption image of atoms subject to 40-μs Bragg pulses. The fringe spacing was λ_f=210 μm after 48 ms time of flight. These longer Bragg pulses addressed only a subset of the momentum distribution. (b) Cross section and fit (black circles and gray line, respectively).

accurate description of the observed fringe visibility. At higher temperatures, however, the observed contrast is consistently greater than expected. While Bose-Einstein statistics can considerably enhance contrast at temperatures even above T_c [16,17], our experiment does not achieve the high densities necessary to make this effect pronounced. One possible explanation for the discrepancy in Fig. 5, below, is that our model fails when the Bragg diffraction becomes velocity selective—i.e., when the Doppler width of the atoms exceeds the Fourier width of the Bragg pulses.

In order to further investigate this effect, we repeated the experiment with longer, more velocity-selective pulses. The absorption images showed that these pulses addressed a narrow range of atomic velocities (Fig. 4). In this case the fit routine was modified to account for the (Gaussian) background of atoms unaffected by the Bragg pulses. While the fraction of out-coupled atoms decreased with increasing temperature, the interference was still clearly visible. In Fig. 5 the measured contrast deviates substantially from theory (dashed line). While velocity selectivity clearly plays a role, the mechanism for this enhanced contrast is not apparent. We have shown that it is only the initial cloud size R_T that determines the contrast for a given λ_f [Eq. (3)]. Since the Bragg pulses are not spatially selective, we do not expect their details to influence the contrast. Similarly, Eq. (4) illustrates why velocity selection does not increase the coherence length in time of flight: the narrowed momentum distribution implies a larger effective de Broglie wavelength which is exactly canceled by the reduced expansion in time of flight. Therefore, the enhanced contrast in Fig. 5 cannot be described by the single-particle free expansion of a thermal gas. We suspect that particle interactions play a role.

In conclusion, we have shown how the coherence length of a trapped gas is modified during ballistic expansion. This allows for the observation of high-contrast interference in a sample at any temperature and is not limited to condensates. For the technique employed here, the only advantage of a BEC is its larger initial coherence length, which is equal to the size of the condensate [1,9,16]. However, it is the ability of two independent condensates to interfere that sets this state of matter apart [18]. Two independent thermal clouds would not interfere. The self-interference technique characterized here can be used to study the coherence properties of other novel quantum degenerate systems. One example is molecular clouds created by sweeping an external magnetic

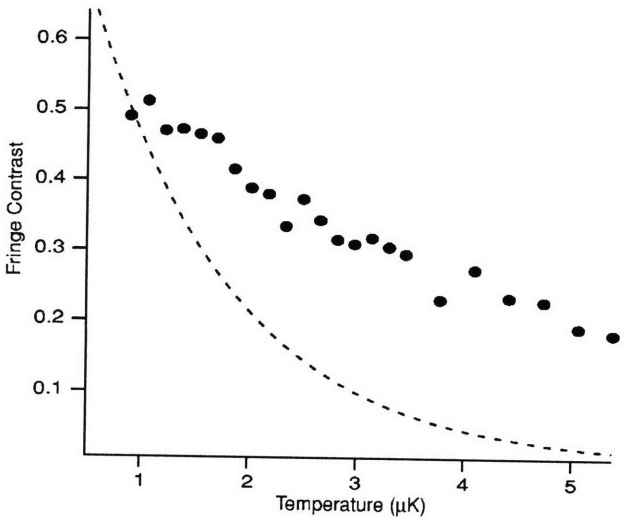

FIG. 5. Measured contrast for τ_p=30 μs velocity-selective Bragg pulses. The contrast was significantly higher than that predicted by Eq. (3) (dashed line). The fringe spacing was λ_f =170 μm after 48 ms expansion time.

field across a Feshbach resonance. While the rapid decay of such a sample precluded thermalization, an interferometric method has already been used to demonstrate coherence in this system [19].

The authors thank D. E. Pritchard for a critical reading of the manuscript, M. W. Zwierlein for contributions to the data analysis, and W. Setiawan for experimental assistance. This research was supported by NSF, ONR, ARO, and NASA.

[1] M. R. Andrews, C. G. Townsend, H.-J. Miesner, D. S. Durfee, D. M. Kurn, and W. Ketterle, Science **275**, 637 (1997).
[2] A. Cho, Science **301**, 750 (2003).
[3] C. A. Regal, M. Greiner, and D. S. Jin, Phys. Rev. Lett. **92**, 040403 (2004).
[4] M. W. Zwierlein, C. A. Stan, C. H. Schunck, S. M. F. Raupach, A. J. Kerman, and W. Ketterle, Phys. Rev. Lett. **92**, 120403 (2004).
[5] C. Chin, M. Bartenstein, A. Altmeyer, S. Riedl, S. Jochim, J. H. Denschlag, and R. Grimm, Science **305**, 1128 (2004).
[6] J. Herbig, T. Kraemer, M. Mark, T. Weber, C. Chin, H.-C. Ngerl, and R. Grimm, Science **301**, 1510 (2003).
[7] S. Dürr, T. Volz, A. Marte, and G. Rempe, Phys. Rev. Lett. **92**, 020406 (2004).
[8] K. Xu, T. Mukaiyama, J. R. Abo-Shaeer, J. K. Chin, D. E. Miller, and W. Ketterle, Phys. Rev. Lett. **91**, 210402 (2003).
[9] E. Hagley *et al.*, Phys. Rev. Lett. **83**, 3112 (1999).
[10] J. E. Simsarian, J. Denschlag, M. Edwards, C. W. Clark, L. Deng, E. W. Hagley, K. Helmerson, S. L. Rolston, and W. D. Phillips, Phys. Rev. Lett. **85**, 2040 (2000).
[11] O. Carnal and J. Mlynek, Phys. Rev. Lett. **66**, 2689 (1991).
[12] J. R. Abo-Shaeer, C. Raman, J. M. Vogels, and W. Ketterle, Science **292**, 476 (2001).
[13] P. J. Martin, B. G. Oldaker, A. H. Miklich, and D. E. Pritchard, Phys. Rev. Lett. **60**, 515 (1988).
[14] D. M. Giltner, R. W. McGowan, and S. A. Lee, Phys. Rev. A **52**, 3966 (1995).
[15] N. F. Ramsey, Rev. Mod. Phys. **62**, 541 (1990).
[16] I. Bloch, T. Hänsch, and T. Esslinger, Science **403**, 166 (2000).
[17] M. Naraschewski and R. J. Glauber, Phys. Rev. A **59**, 4595 (1999).
[18] M. Naraschewski, H. Wallis, A. Schenzle, J. I. Cirac, and P. Zoller, Phys. Rev. A **54**, 2185 (1996).
[19] J. R. Abo-Shaeer, D. E. Miller, J. K. Chin, K. Xu, T. Mukaiyama, and W. Ketterle, Phys. Rev. Lett. **94**, 040405 (2005).

Appendix B

Coherent Molecular Optics using Sodium Dimers

J. R. Abo-Shaeer, D. E. Miller, J. K. Chin, K. Xu,
T. Mukaiyama and W. Ketterle

"Coherent Molecular Optics Using Ultracold Sodium Dimers,"
Phys. Rev. Lett. 94, 40405 (2005).

Coherent Molecular Optics Using Ultracold Sodium Dimers

J. R. Abo-Shaeer,* D. E. Miller, J. K. Chin, K. Xu, T. Mukaiyama, and W. Ketterle†

Department of Physics, MIT-Harvard Center for Ultracold Atoms, and Research Laboratory of Electronics, MIT, Cambridge, Massachusetts 02139, USA

(Received 13 September 2004; published 3 February 2005)

Coherent molecular optics is performed using two-photon Bragg scattering. Molecules were produced by sweeping an atomic Bose-Einstein condensate through a Feshbach resonance. The spectral width of the molecular Bragg resonance corresponded to an instantaneous temperature of 20 nK, indicating that atomic coherence was transferred directly to the molecules. An autocorrelating interference technique was used to observe the quadratic spatial dependence of the phase of an expanding molecular cloud. Finally, atoms initially prepared in two momentum states were observed to cross pair with one another, forming molecules in a third momentum state. This process is analogous to sum-frequency generation in optics.

DOI: 10.1103/PhysRevLett.94.040405 PACS numbers: 03.75.Be, 32.80.Pj, 33.80.Ps, 34.20.Cf

Similar to the field of optics, where the high intensity and coherence of lasers allow for the observation of effects such as frequency doubling and wave mixing, atom optics has benefited greatly from the realization of Bose-Einstein condensates (BECs). High phase-space density (atoms per mode) and a uniform phase [1,2] give the condensate its laserlike qualities. Although not fundamentally required [3,4], BECs have led to the observation of such phenomena as four-wave mixing [5], matter wave amplification [6,7], and atom number squeezing [8].

The current state of molecular optics is similar to atom optics prior to the realization of BECs. Diffraction and interferometry of thermal molecular beams has been demonstrated [9–12], yet monoenergetic beams lack the density necessary to observe nonlinear effects. However, recent experiments using Feshbach resonances have demonstrated the conversion of degenerate atomic bosons [13–15] and fermions [16–20] into ultracold molecules. These sources have the potential to greatly advance molecular optics. Furthermore, atom-molecule coupling can be studied as the first steps towards "superchemistry," where chemical reactions are stimulated via macroscopic occupation of a quantum state [21].

The coherent manipulation of atomic matter waves via stimulated light scattering has been crucial in the development of nonlinear atom optics (for a review, see [22]). Here we demonstrate the ability to apply Kapitza-Dirac and Bragg diffraction [23] to cold molecules. Using optical standing waves of suitably chosen frequencies, sodium dimers were coherently manipulated with negligible heating or other incoherent processes. First, we characterized the coherence of our "source" molecules, created via Feshbach resonance. By measuring the Bragg spectrum of the molecules immediately after their creation, the conversion from atoms to molecules was shown to be coherent—the matter wave analog to frequency doubling in optics. The quadratic spatial dependence of the phase of the expanding molecules was observed using an autocorrelation interference technique. By creating a duplicate sample of molecules and overlapping it with the original, matter wave interference was observed. Finally, the matter wave analog to sum-frequency generation was demonstrated. Atoms prepared in two momentum states, prior to creating molecules, were observed to cross pair, generating a third momentum state.

To produce molecules, sodium condensates were prepared in a crossed optical dipole trap in the $|F, m_F\rangle = |1, -1\rangle$ state. Trap frequencies of $(\omega_x, \omega_y, \omega_z) = 2\pi \times (146\,105\,23)$ Hz yielded a typical peak density of $n_0 \simeq 4.3 \times 10^{14}$ cm^{-3} for 25×10^6 atoms. Atoms were then spin-flipped to the $|1, 1\rangle$ state, in which a 1 G wide Feshbach resonance exists at 907 G [24].

The magnetic field sequence used to create and detect Na_2 molecules was identical to our previous work [15,25]. Briefly, the axial (z axis) magnetic field was ramped to 903 G in 100 ms. In order to prepare the condensate on the negative scattering length side of the resonance, the field was stepped up to 913 G as quickly as possible (~ 1 μs) to jump through the resonance with minimal atom loss. After waiting 1200 μs for the transient field to die down, the field was ramped back down to 903 G in 50 μs to form molecules. In order to remove nonpaired atoms from the trap, the sample was irradiated with a 10 μs pulse of resonant light. Because 903 G is far from the Feshbach resonance, the mixing between atomic and molecular states was small, and therefore molecules were transparent to this "blast" pulse. By ramping the field back to 913 G, molecules were converted back to atoms. Absorption images were taken at high fields (either at 903 G or 913 G), with the imaging light incident along the axial direction of the condensate. Bragg scattering of atoms and molecules was carried out using two nearly orthogonal beams ($\theta_B = 84°$), aligned such that particles were scattered along the x axis of the trap. The beams were far detuned from atomic-molecular transitions to limit spontaneous scattering. For atoms the detuning was $\simeq 4$ nm from the sodium D lines. To find a suitable transition for the molecules, we scanned the laser wavelength and measured the Rabi frequency for Bragg transitions. Several narrow transitions were observed, but not carefully characterized. For this work the

laser was set to 590.159 nm and detuned ~50 MHz from the apparent resonance, yielding a Rabi frequency of 2 kHz.

Figure 1 shows time-of-flight images of Bragg scattering for atoms and molecules. Because the kinetic energy of the scattered particles was much larger than their mean-field energy, individual momentum states were well resolved in ballistic expansion. Both atoms and molecules receive equal two-photon recoil momentum, $p_r = 2h\sin(\theta_B/2)/\lambda_L$, where λ_L is the wavelength of the Bragg beams. However, scattered molecules move away from the central peak with half the velocity of atoms, owing to their doubled mass. Figures 1(c) and 1(d) show Kapitza-Dirac scattering, where multiple atomic and molecular momentum states were populated due to the broad frequency distribution of the short pulse (5 μs).

In order to study the coherence properties of the sample, Bragg spectra [1] were taken with ~1 kHz resolution by pulsing on the two laser beams (250 μs square pulse) before releasing the particles from the trap. For noninteracting particles, the Bragg resonance occurs at a relative detuning of $\nu_0 = \pm p_r^2/2mh$ between the beams, where the sign of ν_0 dictates the direction of outcoupling. Interactions in a condensate give rise to a mean-field shift of the resonance $\delta\nu = 4n_0U/7h$, where $U = 4\pi\hbar^2a/m$ and a is the scattering length. Figure 2 shows three spectra for (a) atoms above the Feshbach resonance, as well as (b) atoms and (c) molecules after sweeping through the resonance. The reduced mean-field shift for atoms below the resonance [Fig. 1(b)] can be attributed to inelastic losses caused by passing through the resonance. Atoms below the resonance coexisted with a small fraction of molecules (2%). The peak output for each set of data is normalized to 1. The actual peak outcoupled fractions were 0.06 for the atoms and 0.5 for the molecules. The atomic signal was kept intentionally low to minimize collisions which make the data analysis difficult [see halos in Fig. 1(c)]. As expected from the resonance condition, molecular resonances occur at half the frequency of atomic resonances.

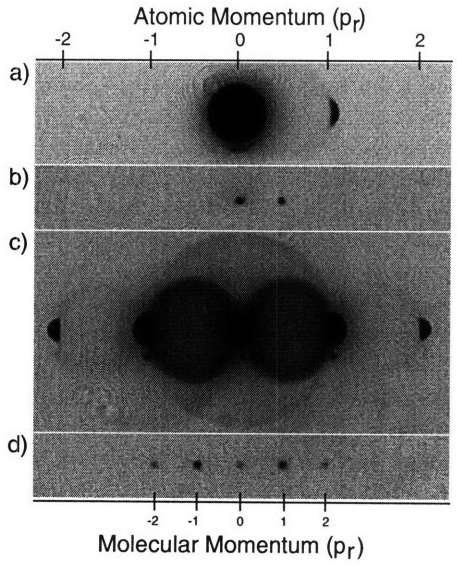

FIG. 1. Bragg diffraction of (a) atoms and (b) molecules. Scattered particles recoil with identical momenta, p_r. However, during ballistic expansion, diffracted molecules expand with half the velocity of atoms, due to their doubled mass. The pulse duration in each image was 200 μs. A shorter pulse (5 μs) populated multiple (c) atomic and (d) molecular momentum states. The halos in (c) are due to collisions between different momentum states [36]. The time of flight in each image is 17 ms.

Two mechanisms contribute to the fundamental width of the Bragg resonance [1,26]. For a parabolic density distribution, the finite size of the sample yields a momentum spread

$$\Delta\nu_p = 1.58\frac{p_r}{2\pi m x_0}, \tag{1}$$

where x_0 is the Thomas-Fermi radius. In addition, the inhomogeneous density distribution of the sample produces a spread in mean-field energy

$$\Delta\nu_n = \sqrt{\frac{8}{147}}\frac{n_0U}{h}. \tag{2}$$

The fundamental width is approximately given by the quadrature sum of these two broadening mechanisms $\Delta\nu = \sqrt{\Delta\nu_n^2 + \Delta\nu_p^2}$.

The fundamental width, $\Delta\nu$, and measured rms width, $\overline{\sigma}$, are compared for each case in Table I. n_0 and x_0 were determined from the size of the condensate in time of flight. The measured widths cannot be accounted for by fundamental broadening mechanisms alone. For atoms above resonance, the fundamental width is $\Delta\nu = 1.39$ kHz, compared to the measured value of

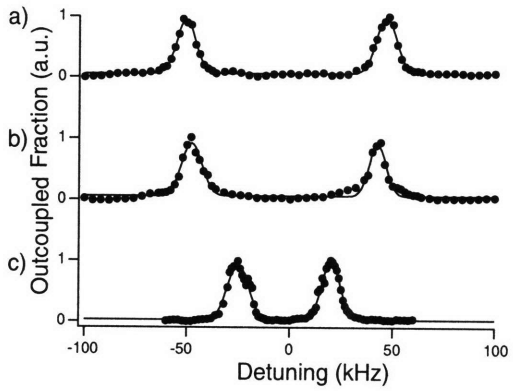

FIG. 2. Bragg spectra for atoms and molecules. In (a) the spectrum is taken for a pure atomic sample above the Feshbach resonance (913 G). (b) and (c) are spectra of atoms and molecules, respectively, below the resonance (903 G). In (c) atoms were removed from the trap with resonant light to limit losses due to atom-molecule collisions. The Bragg resonance condition for molecules occurs at half the frequency of the atomic resonance.

4.46 kHz. Therefore, another broadening mechanism must contribute ~4 kHz to the width. Most likely this is due to Doppler broadening caused by random center-of-mass motion and other collective excitations of the condensate. This was investigated by mixing two frequencies into each Bragg beam to outcouple particles in both $\pm x$ directions. For particles at rest, the outcoupling should always be symmetric. However, we observe the ratio of outcoupled particles in either direction to fluctuate. In addition, we measure a small, consistent shift in the Bragg spectrum, indicating a drift velocity. A line broadening of 4 kHz corresponds to a velocity of $\simeq 2$ mm/s, or a vibrational amplitude of $\simeq 2$ μm (compared to $x_0 = 13$ μm). This is not unreasonable, because the field ramping scheme used to bring the atoms to high field is violent and may induce collective excitations such as breathing modes.

Despite vibrational noise making the dominant contribution to the width of the spectra, the measured values are still narrow enough to indicate quantum degeneracy. For a given $\overline{\sigma}$, the corresponding temperature for a thermal distribution of particles is

$$T = \frac{mh^2\overline{\sigma}^2}{k_B p_r^2}. \tag{3}$$

Thus, for an rms width of 4.5 kHz, the temperature for a thermal distribution of molecules would be 20 nK, comparable to a previous value obtained using a time-of-flight technique [15]. The BEC transition temperature for our trap parameters [27] and 5×10^4 molecules is much higher (115 nK). This demonstrates a deeply degenerate, purely molecular sample, where as previous experiments have demonstrated coherent admixture of molecular character into an atomic BEC [28].

The molecular Bragg spectrum showed a surprisingly large shift of $\delta\overline{\nu} = 625$ Hz. If interpreted as a mean-field shift, this would imply either a very high density (possible due to a spatial collapse) or an anomalously large molecular scattering length outside the Feshbach resonance. Further study is necessary.

The spatial phase of the expanding molecular cloud was directly imaged using an autocorrelation method [29], which gives rise to the self-interference of the molecular sample (see Fig. 3). To accomplish this, two identical copies of the sample were made using a short Kapitza-Dirac pulse (10 μs), applied after 2 ms of ballistic expansion. The copies, with momentum $\pm p_r$, moved away from the zero momentum peak for time Δt before an identical pulse recombined them with the original. This type of interferometer has three readout ports, with momenta 0, $\pm p_r$. The straightline interference fringes are characteristic of a quadratic spatial phase. We observe fringe contrast as high as 50% and a fringe spacing consistent with $\lambda_f = ht/md$ [30], where $d = p_r\Delta t/m$ is the distance the copies moved between pulses [31]. Interference fringes can only be resolved for small d. Therefore, this method cannot be used to observe coherence lengths longer than those inferred from Bragg spectroscopy. It should be noted that the appearance of interference fringes does not imply that the sample is condensed. Rather, it demonstrates only that the coherence length in time of flight is longer than the separation d. Therefore, similar interference can also be observed for a cloud of thermal atoms [32,33].

The conversion of atoms to molecules may be viewed as the atom optic equivalent of frequency doubling [34]. The relevant Hamiltonian for the atom-molecule coupling has the same form as that for the optical frequency doubling process:

$$a_{2m}^\dagger a_m a_m, \tag{4}$$

where a_m is the annihilation operator for the atomic field and $a_{2m}^\dagger$ is the creation operator for the molecular field. The measurement of the Bragg spectrum shows that the sharp "linewidth" of the seed (atom) laser is inherited by the molecular laser. In nonlinear optics, photon interactions are

TABLE I. Fundamental width ($\Delta\nu$), measured rms width ($\overline{\sigma}$), and the corresponding temperature (T), assuming a thermal distribution.

Spectrum	$\Delta\nu$ (kHz)	$\overline{\sigma}$ (kHz)	T (nK)
Atoms (above)	1.39	4.46(17)	10
Atoms (below)	1.03	4.50(60)	10
Molecules	0.36[a]	4.53(14)	20

[a]This lower bound assumes that the molecules have the same spatial profile as the atoms, which our results indicate is not the case.

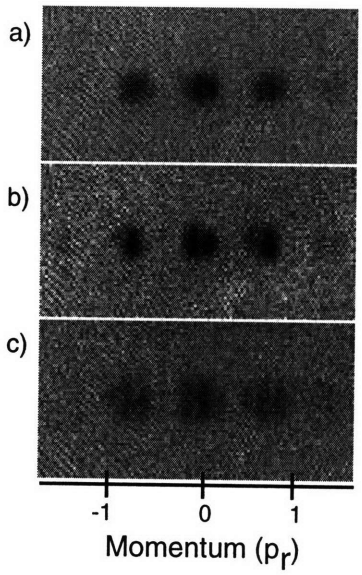

FIG. 3. Matter wave interference of molecules. (a) The molecular sample is split with a short Kapitza-Dirac pulse, creating two identical copies with momenta $\pm p_r$. (b),(c) After the copies have separated for time $\Delta t = 100$ μs, a second pulse recombines them, giving rise to interference in each momentum component. The time of flight in each image is 12 ms.

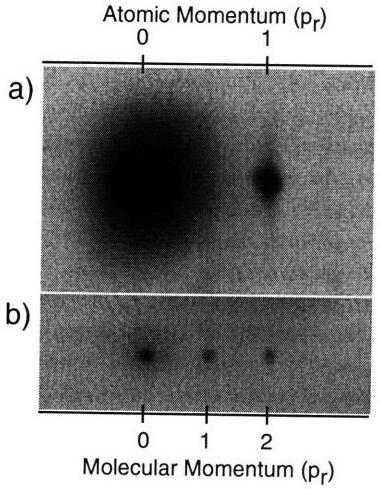

FIG. 4. Sum-frequency generation of atomic matter waves. (a) Atoms were initially prepared in momentum states 0, 1. (b) By sweeping through the Feshbach resonance, atoms combine to form molecules with momenta 0, 1, and 2. Momentum state 1 is the sum frequency of the two atomic matter waves. The "nonlinear medium" is provided by the atomic interactions. The time of flight in each image is 17 ms.

typically mediated by a refractive medium. Here, the nonlinearity arises from the atoms themselves, in the form of s-wave interactions. The high density, or "brightness," of the source, together with the enhanced interactions at the Feshbach resonance provide the means to combine two matter waves. By combining two disparate matter waves, rather than identical ones, we extend the analogy of frequency doubling to the more general process of sum-frequency generation. To do this, atoms were initially prepared in momentum states 0, 1 (in units of p_r). By sweeping through the resonance, molecules were produced in three momentum states: 0, 1, and 2 (see Fig. 4). States 0 and 2 are simply the frequency doubled components of the two initial matter waves. State 1, however, results from cross pairing between the initial momentum states and is thus their sum frequency. This is the first time that a Feshbach resonance was observed between atoms colliding with a controlled nonvanishing momentum. The Feshbach resonance should be slightly shifted compared to the resonance for atoms at rest, which reflects the same physics encountered in the temperature dependence of the position of the resonance [35].

In conclusion, we have demonstrated coherent molecular optics using standing light waves. The ability to coherently convert atoms into molecules makes molecular optics even richer than atom optics. In addition, the techniques demonstrated in this Letter could prove useful for probing molecules formed in quantum-degenerate Fermi systems, and possibly even Cooper pairs.

The authors would like to acknowledge M. Boyd and W. Setiawan for experimental contributions and thank A. E. Leanhardt and M. W. Zwierlein for critical readings of the manuscript. This research is supported by NSF, ONR, ARO, and NASA.

*Present address: Lawrence Berkeley National Laboratories, MS88R0192, Berkeley, CA 94720-8101, USA.
Email address: jrabo-shaeer@lbl.gov
†Electronic address: http://cua.mit.edu/ketterle_group

[1] J. Stenger *et al.*, Phys. Rev. Lett. **82**, 4569 (1999).
[2] E. W. Hagley *et al.*, Phys. Rev. Lett. **83**, 3112 (1999).
[3] M. G. Moore and P. Meystre, Phys. Rev. Lett. **86**, 4199 (2001).
[4] W. Ketterle and S. Inouye, Phys. Rev. Lett. **86**, 4203 (2001).
[5] L. Deng *et al.*, Nature (London) **398**, 218 (1999).
[6] S. Inouye *et al.*, Nature (London) **402**, 641 (1999).
[7] M. Kozuma *et al.*, Science **286**, 2309 (1999).
[8] C. Orzel *et al.*, Science **291**, 2386 (2001).
[9] C. Bordé *et al.*, Phys. Lett. A **188**, 187 (1994).
[10] M. S. Chapman *et al.*, Phys. Rev. Lett. **74**, 4783 (1995).
[11] L. Hackermüller *et al.*, Phys. Rev. Lett. **91**, 090408 (2003).
[12] H. Sakai *et al.*, Phys. Lett. A **57**, 2794 (1998).
[13] S. Dürr, T. Volz, A. Marte, and G. Rempe, Phys. Rev. Lett. **92**, 020406 (2003).
[14] J. Herbig *et al.*, Science **301**, 1510 (2003).
[15] K. Xu *et al.*, Phys. Rev. Lett. **91**, 210402 (2003).
[16] C. A. Regal, C. Ticknor, J. L. Bohn, and D. S. Jin, Nature (London) **424**, 47 (2003).
[17] S. Jochim *et al.*, Science **302**, 2101 (2003).
[18] M. W. Zwierlein *et al.*, Phys. Rev. Lett. **91**, 250401 (2003).
[19] J. Cubizolles *et al.*, Phys. Rev. Lett. **91**, 240401 (2003).
[20] K. E. Strecker, G. B. Partridge, and R. G. Hulet, Phys. Rev. Lett. **91**, 080406 (2003).
[21] D. J. Heinzen, R. Wynar, P. D. Drummond, and K. V. Kheruntsyan, Phys. Rev. Lett. **84**, 5029 (2000).
[22] S. L. Rolston and W. D. Phillips, Nature (London) **416**, 219 (2002).
[23] M. Kozuma *et al.*, Phys. Rev. Lett. **82**, 871 (1999).
[24] S. Inouye *et al.*, Nature (London) **392**, 151 (1998).
[25] T. Mukaiyama *et al.*, Phys. Rev. Lett. **92**, 180402 (2004).
[26] J. Stenger *et al.*, Phys. Rev. Lett. **84**, 2283(E) (2000).
[27] For an optical dipole trap using 1064 nm light, the trap parameters for both atoms and molecules are the same.
[28] E. A. Donley, N. R. Claussen, S. T. Thompson, and C. E. Wieman, Nature (London) **417**, 529 (2002).
[29] J. Simsarian *et al.*, Phys. Rev. Lett. **85**, 2040 (2000).
[30] M. R. Andrews *et al.*, Science **275**, 637 (1997).
[31] Strictly speaking, this analysis applies only to the out-coupled ports. The center port is comprised of three copies.
[32] I. Bloch, T. W. Hänsch, and T. Esslinger, Nature (London) **403**, 166 (2000).
[33] D. Miller *et al.*, cond-mat/0412672.
[34] B. Saleh and M. Teich, *Fundamentals of Photonics* (Wiley, New York, 1991).
[35] V. Vuletić, C. Chin, A. J. Kerman, and S. Chu, Phys. Rev. Lett. **83**, 943 (1999).
[36] A. P. Chikkatur *et al.*, Phys. Rev. Lett. **85**, 483 (2000).

Appendix C

Evidence for Superfluidity of Ultracold Fermions in an Optical Lattice

J.K.Chin, D.E. Miller, Y. Liu, C. Stan, W. Setiawan,

C. Sanner, K.Xu, W. Ketterle

"Evidence for Superfluidity of Ultracold Fermions in an Optical Lattice,"

Nature 443, 961 (2006).

LETTERS

Evidence for superfluidity of ultracold fermions in an optical lattice

J. K. Chin[1], D. E. Miller[1], Y. Liu[1], C. Stan[1]†, W. Setiawan[1], C. Sanner[1], K. Xu[1] & W. Ketterle[1]

The study of superfluid fermion pairs in a periodic potential has important ramifications for understanding superconductivity in crystalline materials. By using cold atomic gases, various models of condensed matter can be studied in a highly controllable environment. Weakly repulsive fermions in an optical lattice could undergo *d*-wave pairing[1] at low temperatures, a possible mechanism for high temperature superconductivity in the copper oxides[2]. The lattice potential could also strongly increase the critical temperature for *s*-wave superfluidity. Recent experimental advances in bulk atomic gases include the observation of fermion-pair condensates and high-temperature superfluidity[3–8]. Experiments with fermions[9–11] and bosonic bound pairs[12,13] in optical lattices have been reported but have not yet addressed superfluid behaviour. Here we report the observation of distinct interference peaks when a condensate of fermionic atom pairs is released from an optical lattice, implying long-range order (a property of a superfluid). Conceptually, this means that *s*-wave pairing and coherence of fermion pairs have now been established in a lattice potential, in which the transport of atoms occurs by quantum mechanical tunnelling and not by simple propagation. These observations were made for interactions on both sides of a Feshbach resonance. For larger lattice depths, the coherence was lost in a reversible manner, possibly as a result of a transition from superfluid to insulator. Such strongly interacting fermions in an optical lattice can be used to study a new class of hamiltonians with interband and atom–molecule couplings[14].

Previous experiments showing long-range phase coherence in Bose–Einstein condensates (BECs) and in fermion superfluids used ballistic expansion to observe the interference of two independent condensates[15], vortex lattices[8,16,17] or interference peaks after release from an optical lattice[18,19]. However, for strongly interacting fermions, elastic collisions can change the momentum distribution and wash out interference peaks. For an initially superfluid cloud, such dissipative dynamics corresponds to superfluid flow faster than the critical velocity. Consistent with this expectation is the observation that a strongly interacting Fermi superfluid initially containing distinct momentum components yielded a broad diffuse cloud after expansion (Fig. 1). This issue was addressed by using a magnetic field ramp that quickly increased the detuning from a Feshbach resonance, taking the system out of the strongly interacting regime and enforcing ballistic expansion. In previous studies of strongly interacting Fermi gases, magnetic field sweeps were applied to prevent fermion pairs above the Feshbach resonance from dissociating[6,7,20]. In contrast, our experiment required a magnetic field sweep both above and below the Feshbach resonance to avoid elastic collisions.

Our experiments used a balanced mixture of ^{6}Li fermions in the two lowest hyperfine states. Evaporative cooling produced a nearly pure fermion pair condensate that was adiabatically loaded into a three-dimensional optical lattice. A broad Feshbach resonance centred at 834 G enabled tuning of the interatomic interactions over a wide range. On resonance, a bound molecular state becomes degenerate with the open atomic scattering channel, leading to a divergence in the scattering length a. Here we explore the region of strong interactions, also known as the BEC–BCS (Bardeen–Cooper–Schrieffer) crossover, in which the magnitude of the interaction parameter $|k_F a|$ is greater than unity, and k_F is defined as the peak Fermi wavevector of a two-component non-interacting mixture of ^{6}Li atoms. In the crossover region, pairing occurs as a result of many-body interactions. Below resonance, for strong interactions, the bare two-body state has a bond length larger than the interatomic spacing and is irrelevant. In a lattice, atom pairs above and below the resonance can be confined to one lattice site[11], and crossover physics may require an occupation larger than or equal to one.

The peak pair filling factor of the lattice was about unity. At this density in the bulk, the fermion pair size is on the order of $1/k_F = 170$ nm, comparable to the lattice spacing of 532 nm. To probe the momentum distribution, we ramped the magnetic field out of the strongly interacting regime as fast as technically possible (about 150 μs) and then turned off the confining potential. Absorption

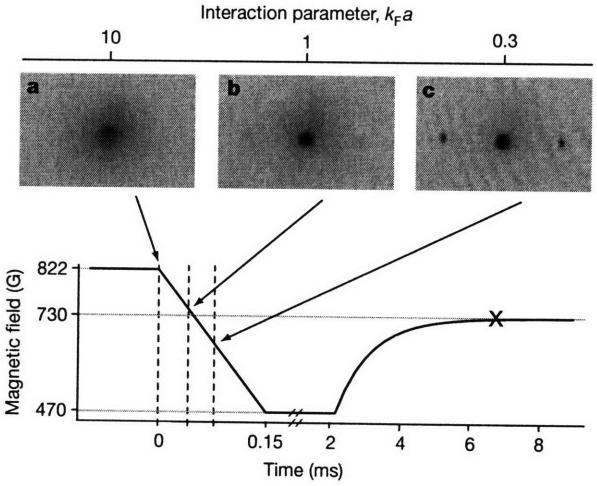

Figure 1 | Dissipative collisions during expansion of a strongly interacting fermionic superfluid. The schematic shows the time sequence of the magnetic field ramp used throughout this paper. A one-dimensional optical standing wave was pulsed onto the superfluid at different magnetic fields B_p (indicated by arrows at 822 G (**a**), 749 G (**b**) and 665 G (**c**)) during expansion, creating particles at twice the photon recoil[30]. Absorption images taken at the time marked with the cross show distinct momentum peaks only at magnetic fields $B_p \leq 750$ G, where $k_F a \leq 1$. At higher magnetic fields, the peaks blurred into a broad diffuse cloud as a result of the larger collision cross-section.

[1]Department of Physics, MIT-Harvard Center for Ultracold Atoms, and Research Laboratory of Electronics, Massachusetts Institute of Technology, Cambridge, Massachusetts 02139, USA. †Present address: Department of Chemistry and Chemical Biology, Harvard University, Cambridge, Massachusetts 02138, USA.

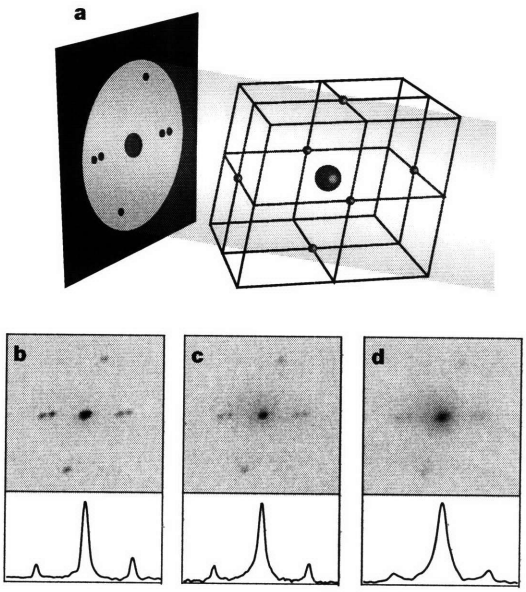

Figure 2 | Observation of high-contrast interference of fermion pairs released from an optical lattice below and above the Feshbach resonance. **a**, The orientation of the reciprocal lattice, also with respect to the imaging light. **b–d**, Interference peaks are observed for magnetic fields of 822 G (**b**), 867 G (**c**) and 917 G (**d**). The lattice depth for all images is $5E_r$, and each image is the average of three shots. The field of view is 1 mm × 1 mm. Density profiles through the vertical interference peaks are shown for each image.

images taken after 6.5 ms of expansion reveal sharp peaks at the reciprocal lattice vectors—the signature of long-range coherence, a strong indicator for superfluidity.

We observed these interference peaks at magnetic fields both above and below the Feshbach resonance (Fig. 2). The six first-order diffracted peaks are clearly visible around the zero momentum fraction and their positions correspond to the expected momentum quanta of $2\hbar k_L$ carried by molecules of mass $2m$, where k_L is the lattice wavevector. At high magnetic fields (Fig. 2d) the visibility of the interference peaks decreased and some additional heating was observed. This degradation could be due to a higher fraction of thermal atoms as we approached the BCS limit, but it was not studied in detail.

The narrow interference peaks clearly reveal the presence of a macroscopic wavefunction possessing long-range phase coherence. The separation between the interference peaks relative to their width gives an estimate of the coherence length of about ten lattice sites. This estimate is a lower bound, because effects of finite resolution and mechanisms of residual broadening have been neglected. With unity occupation, and in the absence of any discernible background at magnetic fields near the Feshbach resonance, this implies a minimum phase space density of 10^3 and shows that our samples are deep in the quantum-degenerate regime. In previous studies of ultracold Bose and Fermi gases, the appearance of a condensate fraction and long-range phase coherence was shown to occur concurrently with the possibility to excite superfluid flow[8,16,17,21]. Superfluid hydrodynamics is usually regarded as the direct proof for superfluidity. However, all reports of superfluidity of bosons in three-dimensional optical lattices have relied solely on observations of sharp interference peaks and inferred superfluidity from the established connection between long-range coherence and superfluidity[19,22]. Similarly, our observations directly show long-range coherence and indirectly show superfluidity of fermion pairs in an optical lattice.

For deep lattices, breakdown of superfluid behaviour has been observed for weakly interacting BECs of different bosonic species[19,23]. This phase transition to the Mott-insulator state occurs when on-site interactions start to suppress atom number fluctuations and the system undergoes a transition from a delocalized superfluid

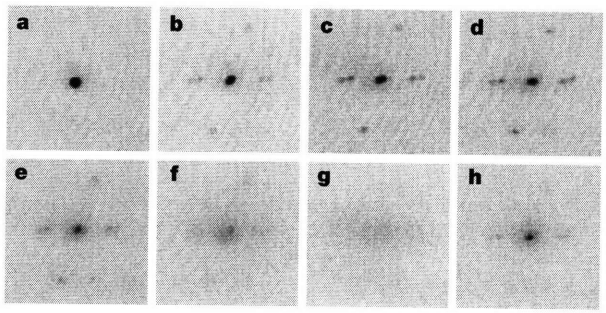

Figure 3 | Interferograms of fermion pairs released from different lattice depths V_0 at a field of 822 G. Values of V_0 are $0E_r$ (**a**), $2.5E_r$ (**b**), $4E_r$ (**c**), $5E_r$ (**d**), $6E_r$ (**e**), $7E_r$ (**f**), $9E_r$ (**g**) and $2.5E_r$ (**h**). **a–g** were taken after an adiabatic ramp up to the final V_0, whereas **h** was taken after first ramping up to $10E_r$ before ramping down to $2.5E_r$.

described by a macroscopic wavefunction to a product of Wannier states tightly localized at each lattice site. Experimentally, this is manifested as a smearing of the distinct $2\hbar k_L$ interference peaks.

Figure 3 shows the change in the coherence properties when the lattice depth was increased. The interference peaks became more pronounced initially, because of increased modulation of the wavefunction. The interference peaks began to smear out, rapidly giving way to a featureless cloud, beyond a critical lattice depth $V_c \approx 6E_r$, where $E_r = \hbar^2 k_L^2/4m = h \times 15$ kHz is the recoil energy. This indicates that all phase coherence had been lost. On subsequent ramping down of the lattice, interference peaks became visible again (Fig. 3h), showing reversibility of the lattice ramp.

We repeated this sequence for a wide range of initial magnetic fields, both above and below the resonance, and observed the same marked change in the interference pattern. Figure 4 displays the peak optical density of the interference peaks for different lattice depths at representative fields. Across all fields, the sharp decrease in peak optical density occurred between $5E_r$ and $6E_r$. A further increase in the magnetic field resulted in decreasing overall visibility, until interference peaks could no longer be observed regardless of lattice depth.

The loss of phase coherence with increasing lattice depth is consistent with the qualitative description of the superfluid to Mott-insulator transition. However, the usual single-band description is no longer applicable, because in the strong-coupling regime the on-site interaction strength should be comparable to the band gap $\hbar\omega$, where ω is the onsite trap frequency. Furthermore, Pauli blocking forbids the multiple occupation of the lowest state of an

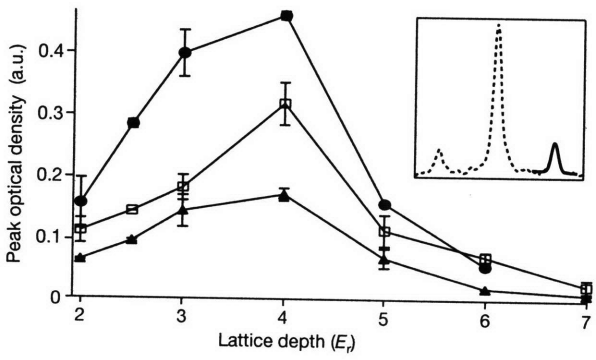

Figure 4 | Peak optical density of interference peaks for increasing lattice depths at different magnetic fields. Values of magnetic fields are 842 G (filled circles), 892 G (open squares) and 942 G (filled triangles). Peak optical densities were estimated from fits to the peaks, including background subtraction. The inset shows a sample density profile of the central and one pair of interference peaks (dotted line), with a bimodal fit to one side peak (solid line). Each point is the average of three different images with six interference peaks per image. Error bars show s.d.

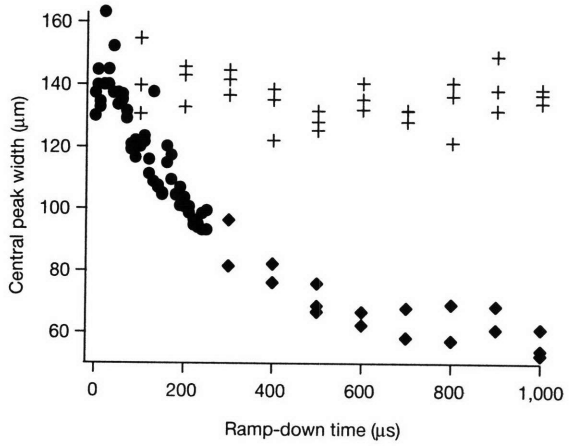

Figure 5 | Restoring coherence from a deep lattice. The width of the central peak is used as a measure of phase coherence after an adiabatic ramp up to $8E_r$, followed by a fast ramp down to $2.5E_r$ at a fixed magnetic field of 822 G. Filled circles were extracted with the use of a gaussian fit, and diamonds with a bimodal fit. Also plotted for comparison is the gaussian width of the central peak for a dephased sample, in which a field gradient was applied during the ramp up of the lattice (crosses). All points were taken for 6.5 ms time of flight.

individual lattice site by identical fermions, and modification of the single-particle tunnelling rate is expected as a result of virtual pair-breaking transitions[14]. One may still be tempted to use the standard bosonic Hubbard model and estimate the critical lattice depth V_c for an assumed value of onsite interaction energy $U = \hbar\omega$ and non-interacting, single-particle tunnelling J, but the obtained $V_c \approx 3E_r$ is significantly smaller than our observation, which is in turn much smaller than the $V_c > 10E_r$ observed for weakly interacting atomic BECs[19,23]. Together with the observed insensitivity of V_c to the magnetic field, this shows that models based on weak interactions are inadequate.

Figure 3h shows the reversibility of the transition from a long-range coherent state to a state without strong coherence. We now study the timescale for this recoherence, by analogy with similar measurements performed across the transition from superfluid to Mott insulator in atomic BECs[19]. Figure 5 shows that phase coherence was restored on a submillisecond timescale, on the order of the single-particle tunnelling time of about 500 μs (for a shallow lattice of $2.5E_r$). When the same lattice ramp sequence was applied to a superfluid that had been dephased by a magnetic field gradient[19], the system did not regain phase coherence on the timescales that we probed. Evaporative cooling is therefore negligible during this time. The short recoherence time of the condensate is evidence that the system stayed in its ground state or at least in a low-entropy state when the lattice was ramped up.

Figure 5 also provides evidence that the system could not recohere during the 150-μs magnetic field ramp. In Fig. 3h, the central peak is well fitted by a bimodal distribution with a width of 35 μm, in clear contrast to the gaussian width of 105 μm obtained from Fig. 5 after 150 μs. We therefore conclude that the observed interference patterns in Fig. 1 reflect the coherence of the cloud at the initial magnetic field, in the strongly interacting regime.

We have shown long-range phase coherence of fermion pairs in an optical lattice in the BEC–BCS crossover region by observing sharp interference peaks during ballistic expansion. This indicates that we have achieved *s*-wave pairing and superfluidity in a lattice potential. Further studies will reveal how the pair wavefunction is affected by confinement[24], and whether the lattice shifts the BEC–BCS crossover away from the Feshbach resonance[25]. The loss of coherence during the lattice ramp up and the rapid recoherence are characteristic of a Mott insulator. However, definitive proof will require a better understanding of the unitarity-limited interactions in such a Fermi system. Recent theoretical work[14,26] predicts that strongly interacting fermions in an optical lattice feature multiband couplings and next-neighbour interactions and can realize the important t–J and magnetic XXZ models of condensed-matter theory. This demonstrates that such atomic systems are an ideal laboratory for the exploration of novel condensed-matter physics.

METHODS

Clouds of superfluid fermion pairs were created in a new experimental setup[27,28] by using techniques similar to those described elsewhere[8]. In brief, a combination of laser cooling and sympathetic cooling of spin-polarized fermions by bosonic ^{23}Na was followed by a spin transfer to create a two-component Fermi gas, allowing further cooling through direct evaporation of the fermions. As the fermions cooled, they formed pairs that Bose-condensed.

Estimates of the scattering length, and hence the interaction parameter, from the magnetic field were obtained with $a(B) = -1{,}405a_0[1 + 300/(B - 834)][1 + 0.0004(B - 834)]$ (ref. 29), where B is measured in gauss and a_0 is the Bohr radius. The calibration of the magnetic field in our system had an uncertainty of about 5 G.

Evaporation was performed at a magnetic field of 822 G, at which strong interactions permitted efficient evaporation. An estimated average final number of $N \approx 2 \times 10^5$ ^{6}Li pairs and harmonic trapping frequencies of $\nu_{x,y,z} = (270{,}340{,}200)$ Hz gave a trap depth of 1.7 μK and a Fermi energy of $E_F = k_B \times 1.4\,\mu K$, where $E_F = \hbar\bar{\omega}(6N)^{1/3}$ and $\bar{\omega}$ is the average trapping frequency. After evaporation, the magnetic field was brought to a desired value B_0 in 20 ms and the condensate was allowed to equilibrate for a further 200 ms. Before ramping to values of B_0 on the BCS side, we also recompressed the optical trap to (340,440,270) Hz and 2.2 μK depth in 100 ms to accommodate the larger Fermi clouds above the resonance[7].

A three-dimensional optical lattice was formed from three optical standing waves, oriented such that the resulting unit cell had a sheared cubic structure, with one axis tilted about 20° from the normal for reasons of optical access (see Fig. 1a)[23]. The incident laser beams were focused down to the condensate with waists of about 90 μm, then retroreflected and overlapped at the condensate to generate the standing-wave potentials. All lattice light was derived from a 1,064-nm single-frequency fibre laser, and each beam was detuned by tens of MHz with respect to the others to eliminate interference between different beams.

The lattice potential was imposed on the condensate by adiabatically increasing the intensity of the laser beams to a variable final value V_0. The calibration of V_0 had an uncertainty of about 20%. A simple linear ramp with a constant rate dV_0/dt of $0.5E_r\,ms^{-1}$ was used unless otherwise specified. This satisfies the inter-band adiabaticity condition of $dV_0/dt \ll 16E_r^2/\hbar$.

Ballistic expansion for the detection of the different momentum components was provided by a magnetic field sequence (shown in Fig. 1) that quickly brought the system out of the strongly interacting regime when all confinement was switched off. During the magnetic field ramp of about 150 μs, the lattice potential was kept on. The first 2 ms of expansion took place at 470 G, at which the molecules are tightly bound, before the field was ramped back up to 730 G in the next 4.5 ms, at which the weakly bound molecules strongly absorb light near the atomic resonance line and could be observed by absorption imaging. The specific magnetic field sequence was chosen to minimize collisions within technical capabilities.

Received 29 June; accepted 25 August 2006.

1. Hofstetter, W., Cirac, J. I., Zoller, P., Demler, E. & Lukin, M. D. High-temperature superfluidity of fermionic atoms in optical lattices. *Phys. Rev. Lett.* **89**, 220407 (2002).
2. Scalapino, D. J. The case for $d_{x^2-y^2}$ pairing in the cuprate superconductors. *Phys. Rep.* **250**, 329–365 (1995).
3. Greiner, M., Regal, C. A. & Jin, D. S. Emergence of a molecular Bose–Einstein condensate from a Fermi gas. *Nature* **426**, 537–540 (2003).
4. Jochim, S. *et al.* Bose–Einstein condensation of molecules. *Science* **302**, 2101–2103 (2003).
5. Zwierlein, M. W. *et al.* Observation of Bose–Einstein condensation of molecules. *Phys. Rev. Lett.* **91**, 250401 (2003).
6. Regal, C. A., Greiner, M. & Jin, D. S. Observation of resonance condensation of fermionic atom pairs. *Phys. Rev. Lett.* **92**, 040403 (2004).
7. Zwierlein, M. W. *et al.* Condensation of pairs of fermionic atoms near a Feshbach resonance. *Phys. Rev. Lett.* **92**, 120403 (2004).
8. Zwierlein, M. W., Abo-Shaeer, J. R., Schirotzek, A., Schunck, C. H. & Ketterle, W. Vortices and superfluidity in a strongly interacting Fermi gas. *Nature* **435**, 1047–1051 (2005).

9. Modugno, G., Ferlaino, F., Heidemann, R., Roati, G. & Inguscio, M. Production of a Fermi gas of atoms in an optical lattice. *Phys. Rev. A* **68**, 011601(R) (2003).
10. Köhl, M., Moritz, H., Stöferle, T., Gunther, K. & Esslinger, T. Fermionic atoms in a three-dimensional optical lattice: observing Fermi surfaces, dynamics, and interactions. *Phys. Rev. Lett.* **94**, 080403 (2005).
11. Stöferle, T., Moritz, H., Gunther, K., Kohl, M. & Esslinger, T. Molecules of fermionic atoms in an optical lattice. *Phys. Rev. Lett.* **96**, 030401 (2006).
12. Volz, T. *et al.* A Mott state of molecules. *Condensed Matt.* (submitted); preprint at <http://arxiv.org/abs/cond-mat/0605184> (2006).
13. Winkler, K. *et al.* Repulsively bound atom pairs in an optical lattice. *Nature* **441**, 853–856 (2006).
14. Duan, L-M. Effective Hamiltonian for Fermions in an optical lattice across a Feshbach resonance. *Phys. Rev. Lett.* **95**, 243202 (2005).
15. Andrews, M. R. *et al.* Observation of interference between two Bose condensates. *Science* **275**, 637–641 (1997).
16. Madison, K. W., Chevy, F., Wohlleben, W. & Dalibard, J. Vortex formation in a stirred Bose–Einstein condensate. *Phys. Rev. Lett.* **84**, 806–809 (2000).
17. Abo-Shaeer, J. R., Raman, C., Vogels, J. M. & Ketterle, W. Observation of vortex lattices in Bose–Einstein condensates. *Science* **292**, 476–479 (2001).
18. Anderson, B. P. & Kasevich, M. A. Macroscopic quantum interference from atomic tunnel arrays. *Science* **282**, 1686–1689 (1998).
19. Greiner, M., Mandel, O., Esslinger, T., Hänsch, T. W. & Bloch, I. Quantum phase transition from a superfluid to a Mott insulator in a gas of ultracold atoms. *Nature* **415**, 39–44 (2002).
20. Schunck, C., Zwierlein, M. W., Schirotzek, A. & Ketterle, W. Superfluid expansion of a strongly interacting Fermi gas. *Condensed Matt.* (submitted); preprint at <http://arxiv.org/abs/cond-mat/0607298> (2006).
21. Onofrio, R. *et al.* Observation of superfluid flow in a Bose–Einstein condensed gas. *Phys. Rev. Lett.* **85**, 2228–2231 (2000).
22. Schori, C., Stöferle, T., Moritz, H., Köhl, M. & Esslinger, T. Excitations of a superfluid in a three-dimensional optical lattice. *Phys. Rev. Lett.* **93**, 240402 (2004).
23. Xu, K. *et al.* Sodium Bose–Einstein condensates in an optical lattice. *Phys. Rev. A.* **72**, 043604 (2005).
24. Moritz, H., Stöferle, T., Gunter, K., Köhl, M. & Esslinger, T. Confinement induced molecules in a 1d Fermi gas. *Phys. Rev. Lett.* **94**, 210401 (2005).
25. Koetsier, A. O., Dickerscheid, D. B. M. & Stoof, H. T. C. BEC–BCS crossover in an optical lattice. *Condensed Matt.* (submitted); preprint at <http://arxiv.org/abs/cond-mat/0604186> (2006).
26. Gubbels, K. B., Dickerscheid, D. B. M. & Stoof, H. T. C. Dressed molecules in an optical lattice. *Condensed Matt.* (submitted); preprint at <http://arxiv.org/abs/cond-mat/0605056> (2006).
27. Hadzibabic, Z. *et al.* Fifty-fold improvement in the number of quantum degenerate fermionic atoms. *Phys. Rev. Lett.* **91**, 160401 (2003).
28. Stan, C. A. & Ketterle, W. Multiple species atom source for laser-cooling experiments. *Rev. Sci. Instrum.* **76**, 063113 (2005).
29. Bartenstein, M. *et al.* Precise determination of ^{6}Li cold collision parameters by radio-frequency spectroscopy on weakly bound molecules. *Phys. Rev. Lett.* **94**, 103201 (2004).
30. Gould, P. L., Ruff, G. A. & Pritchard, D. E. Diffraction of atoms by light: the near-resonant Kapitza–Dirac effect. *Phys. Rev. Lett.* **56**, 827–830 (1986).

Acknowledgements We thank E. Demler, Z. Hadzibabic and M. Zwierlein for discussions. This work was supported by the NSF, the Office of Naval Research and NASA.

Author Information Reprints and permissions information is available at www.nature.com/reprints. The authors declare no competing financial interests. Correspondence and requests for materials should be addressed to J.K.C. (jitkee@mit.edu).

Appendix D

Critical velocity for superfluid flow across the BEC-BCS crossover

D. E. Miller, J. K. Chin, C. A. Stan, Y. Liu, W. Setiawan,
C. Sanner and W. Ketterle
"Critical velocity for superfluid flow across the BEC-BCS crossover,"
Phys. Rev. Lett. 99, 070402 (2007) .

Critical Velocity for Superfluid Flow across the BEC-BCS Crossover

D. E. Miller, J. K. Chin, C. A. Stan,* Y. Liu, W. Setiawan, C. Sanner, and W. Ketterle†

Department of Physics, MIT-Harvard Center for Ultracold Atoms, and Research Laboratory of Electronics, MIT, Cambridge, Massachusetts 02139, USA

(Received 11 July 2007; published 16 August 2007)

Critical velocities have been observed in an ultracold superfluid Fermi gas throughout the BEC-BCS crossover. A pronounced peak of the critical velocity at unitarity demonstrates that superfluidity is most robust for resonant atomic interactions. Critical velocities were determined from the abrupt onset of dissipation when the velocity of a moving one-dimensional optical lattice was varied. The dependence of the critical velocity on lattice depth and on the inhomogeneous density profile was studied.

DOI: 10.1103/PhysRevLett.99.070402 PACS numbers: 03.75.Kk, 03.75.Lm, 03.75.Ss, 05.30.Jp

The recent realization of the BEC-BCS crossover in ultracold atomic gases [1] allows one to study how bosonic superfluidity transforms into fermionic superfluidity. The critical velocity for superfluid flow is determined by the low-lying excitations of the superfluid. For weakly bound fermions, the (Landau) critical velocity is proportional to the binding energy of the pairs, which increases monotonically along the crossover into the Bose-Einstein condensation (BEC) regime. However, the speed of sound, which sets the critical velocity for phonon excitations, is almost constant in the BCS regime, but then decreases monotonically on the BEC side, since the strongly bound molecules are weakly interacting. At the BEC-BCS crossover, one expects a rather narrow transition from a region where excitation of sound limits superfluid flow, to a region where pair breaking dominates. In this transition region, the critical velocity is predicted to reach a maximum [2–4]. This makes the critical velocity one of the few quantities that show a pronounced peak across the BEC-BCS crossover in contrast to the chemical potential, the transition temperature [5], the speed of sound [6,7], and the frequencies of shape oscillations [8], which all vary monotonically.

In this Letter, we report the first study of critical velocities across the BEC-BCS crossover, where a Feshbach resonance allows the magnetic tuning of the atomic interactions, and find that superfluid flow is most robust near the resonance. Our observation of a pronounced maximum of the critical velocity is in agreement with the predicted crossover between the two different mechanisms for dissipation.

Critical velocities have been determined before in atomic BECs perturbed by a stirring beam [9–11] as well as by a 1D moving optical lattice [12]. In both cases, the inhomogeneous density of the harmonically trapped sample had to be carefully accounted for in order to make quantitative comparisons to theory. Here we mitigate this problem by probing only the central region of our sample with a tightly focused moving lattice formed from two intersecting laser beams. For decreasing lattice depths, the critical velocity increases and, at very small depths, approaches a value that is in agreement with theoretical predictions.

In our experiments, we first create a superfluid of ^{6}Li pairs according to the procedure described in previous work [13]. Forced evaporative cooling of an even mixture of the two lowest hyperfine states is performed at a magnetic field of 822 G, on the BEC side of a broad Feshbach resonance centered at $B_0 = 834$ G. This results in a nearly pure Bose-Einstein condensate of $N \approx 5 \times 10^5$ pairs in a cross optical dipole trap with harmonic trapping frequencies $\nu_{x,y,z} = (65, 45, 50)$ Hz. The Fermi energy of the system is $E_F = h\bar{\nu}(6N)^{1/3} = h \times 7.6$ kHz. To form the moving lattice, we focus two phase-locked 1064 nm laser beams to intersect at the sample with an angle of ~90° (see Fig. 1). The resulting 1D lattice has a spatial period of $\lambda_L = 0.75$ μm. A frequency difference between the two beams of $\Delta\nu$ causes the lattice to move with velocity $v_L = \lambda_L \Delta\nu$. The beams have e^{-2} waists of 20 and 60 μm, respectively, and address a relatively homogeneous region at the center of the cloud which has Thomas-Fermi radii $R_{x,y,z} = (63, 91, 82)$ μm. The minimum density at the position of the e^{-2} waist is 42% of the central density.

The lattice which necessarily varies in depth across the sample, is characterized by its peak depth V_0 specified in units of E_F or the recoil energy $E_r = h^2/(8m\lambda_L^2) = h \times 7.3$ kHz, where m is the molecular mass. The lattice depth is calibrated using Kapitza-Dirac scattering. Because of the inhomogeneity of the lattice, the uncertainty is 40%. The lattice depths explored in this Letter are sufficiently small such that motion induced in the laboratory frame is negligible, in contrast to [14].

The lattice moving at a constant velocity is adiabatically ramped up and held for a time t up to 2 s, after which the lattice is ramped down and all confinement is switched off. As in previous work [13], a fast magnetic field ramp is used to reduce strong interactions in order to probe the center-of-mass momentum distribution of the pairs. Subsequently, absorption imaging is done on the atomic resonance line at 730 G. A bimodal fit reveals the number of pairs remaining

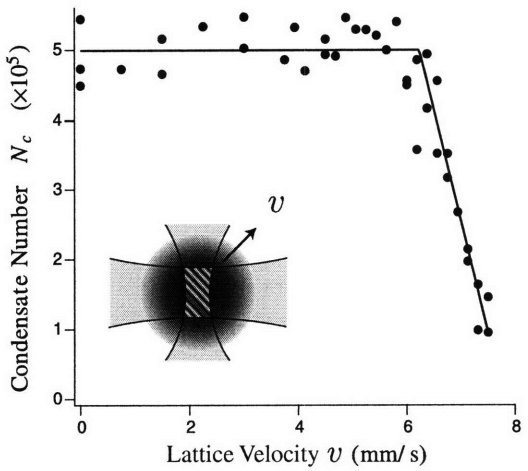

FIG. 1. Onset of dissipation for superfluid fermions in a moving optical lattice. (Inset) Schematic of the experiment in which two intersecting laser beams produced a moving optical lattice at the center of an optically trapped cloud (trapping beams not shown). Number of fermion pairs which remained in the condensate N_c after being subjected to a $V_0 = 0.2E_F$ deep optical lattice for 500 ms, moving with velocity v_L, at a magnetic field of 822 G ($1/k_F a = 0.15$). An abrupt onset of dissipation occurred above a critical velocity v_c, which we identify from a fit to Eq. (1).

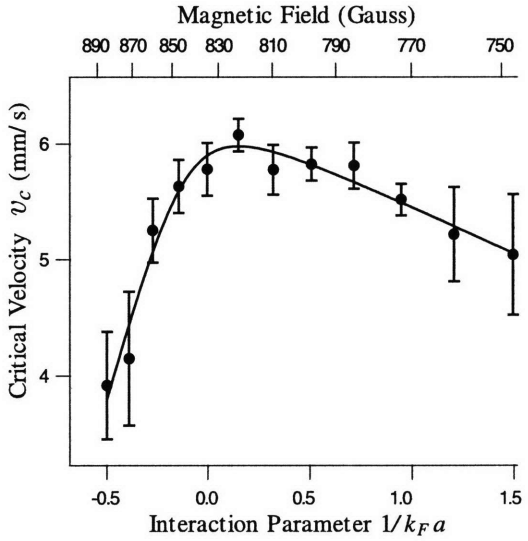

FIG. 2. Critical velocities throughout the BEC-BCS crossover. A pronounced maximum was found at resonance. Data are shown for a $V_0 = 0.2E_F$ deep lattice, held for $t = 500$ ms. The solid line is a guide to the eye.

in the condensate N_c, providing a measure of the heating incurred during application of the moving lattice.

Figure 1 illustrates the characteristic dependence of dissipation on the velocity of the moving lattice. At low velocities, the sample is unaffected. Above some critical velocity v_c, dissipation sets in abruptly. We determine v_c from a fit of N_c to the intersection of two lines with slopes 0 and α:

$$N_{\mathrm{cond}}(v) = N_{\mathrm{cond}}(0)\{1 - \max[0, \alpha(v - vc)]\}. \quad (1)$$

The critical velocity that we obtain from this procedure is consistent for a large range of hold times, varying by less than 15% when the hold time t is changed by a factor of 20. We explore the BEC-BCS crossover by adiabatically ramping the magnetic field to different values after evaporation and repeating the measurement as before. The crossover is parametrized by the interaction parameter $1/k_F a$, where k_F is the Fermi wave vector and a is the B-field dependent s-wave scattering length [15]. Again, we observe a threshold for dissipation.

Figure 2 shows the measured critical velocity throughout the BEC-BCS crossover. The maximum near resonance is consistent with the picture of a crossover between two different types of excitation, as discussed in the introduction, and confirms that superfluidity is most robust on resonance.

To illuminate the role of the inhomogeneous density distribution, we performed experiments in which the entire sample was perturbed by a uniform lattice. Lattice beams with 80 μm waists probed a more tightly confined sample of 2×10^5 pairs, with spatial extent $R_{TF} \simeq 37$ μm. The onset of dissipation seen in Fig. 3 is still striking, but now loss is observed at much lower lattice velocities, in spite of a larger Fermi energy $E_F = h \times 12.4$ kHz. Moreover, the onset of dissipation is slightly more gradual. When the magnetic field was varied across the Feshbach resonance, we again found a maximum of the critical velocity near resonance. The lowering of the critical velocity due to the inhomogeneous density profile is expected, since at lower density, both the speed of sound and (on the BCS side) the pairing energy decrease. Although the critical velocity should approach zero in the low density wings of the cloud, we still observe a sudden onset of dissipation at a finite velocity, similar to studies in Refs. [9–11], where a laser beam pierced through the whole condensate, but in contrast to studies reported in [12].

In the limit of vanishing perturbation, the critical velocity should be given by the Landau criterion. In Fig. 4 we address the effects of a finite lattice potential in the original lattice configuration, as depicted in Fig. 1. The critical velocity is shown to be a decreasing function of V_0, saturating in the limit of low lattice depth ($V_0 \leq 0.03E_F$). This behavior is consistent with numerical simulation [4,16]. Measurements at the smallest lattice depths had large uncertainties, as the hold time required to observe a heating effect of the lattice approached the natural lifetime of our sample. For this reason, we studied the field dependence (Fig. 2) at an intermediate lattice depth, where v_c was more well defined.

For comparison with theory we reference the local Fermi velocity at the trap center $v_F = v'_F(1 + \beta)^{-1/4} = 39$ mm/s, where $v'_F = \sqrt{2E_F/m}$ is the Fermi velocity of a noninteracting gas at the trap center, and $\beta = -0.58$ is a universal parameter characterizing unitarity limited inter-

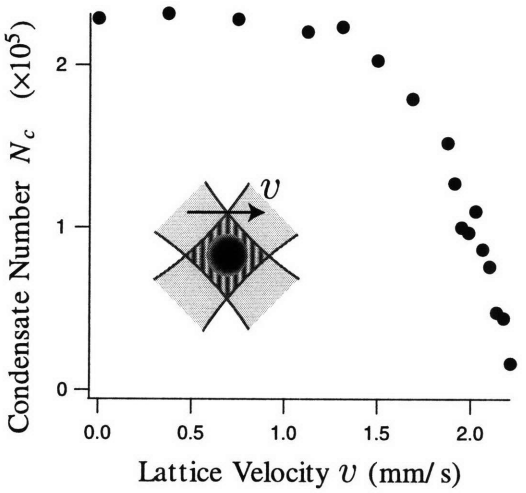

FIG. 3 (color online). Effects of density inhomogeneity on the critical velocity. A configuration in which the lattice beams (80 μm) were larger than the trapped sample (37 μm) results in loss in the condensate number N_c at significantly lower velocity. Data are shown for a $V_0 = 0.15E_F$ deep optical lattice held for 200 ms at a magnetic field of 822 G.

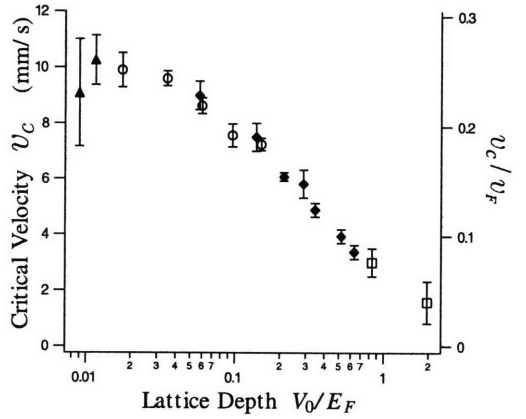

FIG. 4. Critical velocities at different lattice depths. The results show v_c to be a decreasing function of lattice depth V_0. In the limit of low V_0, v_c converges to a maximum value of 0.25 v_F. Data were taken near resonance, at 822 G ($1/k_F a = 0.15$) for hold times $t = 250$, 500, 1000, 2000 ms (squares, diamonds, circles, triangles).

actions [17–19]. For vanishing lattice depth, the observed critical velocity at unitarity approaches $v_c/v_F = 0.25$. If we use the local Fermi velocity $v_{F,w}$ at the e^{-2} waist of the lattice, we obtain $v_c/v_{F,w} = 0.34$. The difference between these values indicates the uncertainty due to residual density inhomogeneity. The local speed of sound in a Fermi gas at unitarity is

$$c_s = v_{F,\mathrm{loc}}(1+\beta)^{1/2}/\sqrt{3} = 0.37 v_{F,\mathrm{loc}}. \quad (2)$$

The critical velocity for pair breaking is

$$v_{\mathrm{pair}} = ((\sqrt{\Delta^2+\mu^2}-\mu)/m)^{1/2} = 0.34 v_{F,\mathrm{loc}}, \quad (3)$$

with $\Delta = 0.50 v_{F,\mathrm{loc}}^2/2m$ [17,19] and $\mu = (1+\beta)v_{F,\mathrm{loc}}^2/2m$. These two values should provide approximate upper bounds to the critical velocity at unitarity [2,3]. It seems natural that the combination of both excitation mechanisms lowers the critical velocity further. Within these uncertainties, and those of the density, the theoretical predictions agree with the experimental results.

Up until now, we have deferred a discussion of how the moving lattice couples to the excitations. In a pure system at zero temperature, one would expect the excitation spectrum to exhibit discrete resonances, where the perturbation couples only to modes with the k vector of the lattice. On the other hand, at finite temperature, it is possible that the lattice drags along thermal atoms which are pointlike perturbations and can create excitations at all k vectors. Our observation that the dissipation sets in at a certain threshold velocity and increases monotonically with velocity is consistent with the participation of the thermal component.

We further elucidated the role of thermal excitations by varying the temperature. Gradually reducing the trap depth from U_0 to U_{min}, during exposure to a lattice moving above v_c, will suppress the accumulation of a thermal component. The lifetime in this case exceeded that for a sample held at a fixed depth of either U_0 or U_{min}. For Bose-Einstein condensates, theoretical papers emphasized the role of the thermal component in the Landau damping process in a moving lattice [20,21]. This was confirmed qualitatively in an experiment at Florence [12] in which the lifetime of the sample was drastically improved by eliminating the thermal atoms.

In our experiments, the clouds heated up during the exposure to the moving lattice. Figure 5 shows the increase in the number of thermal atoms and the loss in the total number of atoms due to evaporative cooling. In an idealized model, where density is fixed, constant dissipation would result in a linear decrease in the number of atoms due to evaporative cooling. Our data show an accelerated decrease, possibly reflecting increased dissipation due to the increasing fraction of thermal atoms. However, an accurate model should include the change in density (and therefore critical velocity) during the exposure time. Additional impurity atoms (e.g., sodium atoms) could cause dissipation even at zero temperature and would allow more controlled studies of the dissipation mechanism. Unpaired atoms in clouds with population imbalance may not play this role because of phase separation effects [22].

Another possible dissipation mechanism in a lattice is the creation of two excitations through a dynamical or modulational instability. Such an instability [23] occurs already for weakly interacting particles moving through a lattice with momentum q, when they collide and scatter into states with momenta $q \pm \delta q$, analogous to optical parametric generation [24]. This process is energetically

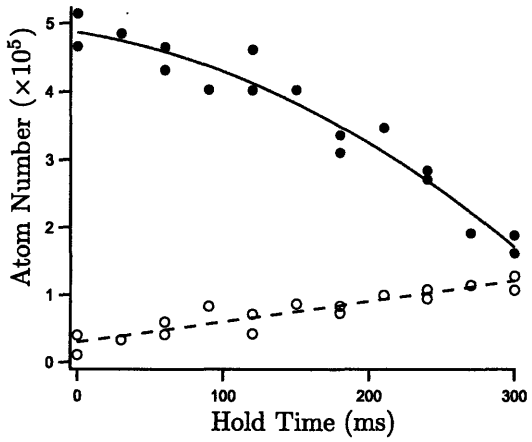

FIG. 5. Number of pairs that remained in the condensate N_c (solid circles) and thermal component N_{th} (open circles) after being held in a $V_0 = 0.35E_F$ deep optical lattice moving with velocity $v_L = 6$ mm/s for a variable hold time. The thermal component shows a linear increase (dashed line), whereas N_{cond} showed an accelerated loss, and is fit to a quadratic function (solid line).

possible only above $0.5q_B$, where $q_B = h/2\lambda_L$ is the Bragg momentum that defines the edge of the Brillouin zone. This corresponds to a velocity $v = 11$ mm/s for fermion pairs (and twice this value for single atoms). Since the highest critical velocities we observe are slightly below this threshold, and strongly decrease already for relatively small V_0, it is very unlikely, that dynamical instabilities play a role in our experiments. Moreover, such instabilities should be strongly modified by Pauli blocking. For our ratio of local Fermi momentum to the Bragg momentum of 0.9, the first band is nearly full in the center of the cloud. For Bose-Einstein condensates, it has been recently predicted [25] and experimentally shown [14] that strong interactions can lower the threshold for the dynamical instability, close to the Mott-insulator transition. The range of 1D lattice depths explored here ($V_0 \leq 2E_r$) is far from the 1D Mott-insulator regime. We have observed the loss of coherence which typically accompanies the superfluid to Mott insulation transition to occur only beyond $V_0 \simeq 25E_r$.

In conclusion, we have used a novel optical lattice geometry to determine critical velocities in the BEC-BCS crossover without the complications of strong density inhomogeneity. This configuration could be applied to studies in atomic Bose gases which so far have been limited by the inhomogeneous density [9–12]. In addition, it would be interesting to study dynamical instabilities for fermions and the role of Pauli blocking.

The authors would like to thank Aviv Keshet for experimental assistance. This research has been supported by the NSF and the U.S. Office of Naval Research.

*Present address: Department of Chemistry and Chemical Biology, Harvard University, Cambridge, MA 02138, USA.

†http://cua.mit.edu/ketterle_group

[1] S. Giorgini, L. P. Pitaevskii, and S. Stringari, arXiv:0706.3360.
[2] R. Sensarma, M. Randeria, and T.-L. Ho, Phys. Rev. Lett. **96**, 090403 (2006).
[3] R. Combescot, M. Y. Kagan, and S. Stringari, Phys. Rev. A **74**, 042717 (2006).
[4] A. Spuntarelli, P. Pieri, and G. C. Strinati, Phys. Rev. Lett. **99**, 040401 (2007).
[5] C. A. R. Śa de Melo, M. Randeria, and J. R. Engelbrecht, Phys. Rev. Lett. **71**, 3202 (1993).
[6] R. Haussmann, W. Rantner, S. Cerrito, and W. Zwerger, Phys. Rev. A **75**, 023610 (2007).
[7] J. Joseph, B. Clancy, L. Luo, J. Kinast, A. Turlapov, and J. E. Thomas, Phys. Rev. Lett. **98**, 170401 (2007).
[8] A. Altmeyer, S. Riedl, C. Kohstall, M. J. Wright, R. Geursen, M. Bartenstein, C. Chin, J. H. Denschlag, and R. Grimm, Phys. Rev. Lett. **98**, 040401 (2007); **98**, 040401 (2007).
[9] C. Raman, M. Köhl, R. Onofrio, D. S. Durfee, C. E. Kuklewicz, Z. Hadzibabic, and W. Ketterle, Phys. Rev. Lett. **83**, 2502 (1999).
[10] R. Onofrio, C. Raman, J. M. Vogels, J. R. Abo-Shaeer, A. P. Chikkatur, and W. Ketterle, Phys. Rev. Lett. **85**, 2228 (2000).
[11] C. Raman, R. Onofrio, J. Vogels, J. Abo-Shaeer, and W. Ketterle, J. Low Temp. Phys. **122**, 99 (2001).
[12] L. De Sarlo, L. Fallani, J. E. Lye, M. Modugno, R. Saers, C. Fort, and M. Inguscio, Phys. Rev. A **72**, 013603 (2005).
[13] J. Chin, D. Miller, Y. Liu, C. Stan, W. Setiawan, C. Sanner, K. Xu, and W. Ketterle, Nature (London) **443**, 961 (2006).
[14] J. Mun, P. Medley, G. K. Campbell, L. G. Marcassa, D. E. Pritchard, and W. Ketterle, arXiv:0706.3946.
[15] M. Bartenstein *et al.*, Phys. Rev. Lett. **94**, 103201 (2005).
[16] S. Ianeselli, C. Menotti, and A. Smerzi, J. Phys. B **39**, S135 (2006).
[17] J. Carlson, S.-Y. Chang, V. R. Pandharipande, and K. E. Schmidt, Phys. Rev. Lett. **91**, 050401 (2003).
[18] G. E. Astrakharchik, J. Boronat, J. Casulleras, and S. Giorgini, Phys. Rev. Lett. **93**, 200404 (2004).
[19] J. Carlson and S. Reddy, Phys. Rev. Lett. **95**, 060401 (2005).
[20] S. Tsuchiya and A. Griffin, Phys. Rev. A **70**, 023611 (2004).
[21] S. Konabe and T. Nikuni, J. Phys. B **39**, S101 (2006).
[22] Y. Shin, M. W. Zwierlein, C. H. Schunck, A. Schirotzek, and W. Ketterle, Phys. Rev. Lett. **97**, 030401 (2006).
[23] B. Wu and Q. Niu, Phys. Rev. A **64**, 061603 (2001).
[24] G. K. Campbell, J. Mun, M. Boyd, E. W. Streed, W. Ketterle, and D. E. Pritchard, Phys. Rev. Lett. **96**, 020406 (2006).
[25] E. Altman, A. Polkovnikov, E. Demler, B. I. Halperin, and M. D. Lukin, Phys. Rev. Lett. **95**, 020402 (2005).

Bibliography

[1] J. R. Abo-Shaeer, D. E. Miller, J. K. Chin, K. Xu, T. Mukaiyama, and W. Ketterle. Coherent molecular optics using ultracold sodium dimers. *Phys. Rev. Lett.*, 94:040405, 2005.

[2] Jamil Abo-Shaeer. *Novel Ground States of Bose-Condensed Gases.* PhD thesis, M.I.T., 2004.

[3] E. Altman, A. Polkovnikov, E. Demler, B. I. Halperin, and M. D. Lukin. Superfluid-insulator transition in a moving system of interacting bosons. *Phys. Rev. Lett.*, 95:020402, 2005.

[4] M.H. Anderson, J.R. Ensher, M.R. Matthews, C.E. Wieman, and E.A. Cornell. Observation of boseeinstein condensation in a dilute atomic vapor. *Science*, 269:198, 269.

[5] M. R. Andrews, D. M. Kurn, H.-J. Miesner, D. S. Durfee, C. G. Townsend, S. Inouye, and W. Ketterle. Propagation of sound in a bose-einstein condensate. *Phys. Rev. Lett.*, 79(4):553–556, Jul 1997.

[6] M. R. Andrews, C. G. Townsend, H.-J. Miesner, D. S. Durfee, D. M. Kurn, and W. Ketterle. Observation of interference between two bose condensates. *Science*, 275:637, 1997.

[7] Neil W. Ashcroft and N. David Mermin. *Solid State Physics.* Thomson Learning, Inc., 1976.

[8] M. Bartenstein, A. Altmeyer, S. Riedl, R. Geursen, S. Jochim, C. Chin, J. Hecker Denschlag, R. Grimm, A. Simoni, E. Tiesinga, C. J. Williams, and P. S. Julienne.

Precise determination of 6li cold collision parameters by radio-frequency spectroscopy on weakly bound molecules. *Phys. Rev. Lett.*, 94:103201, 2005.

[9] F. Bloch and A. Siegert. Magnetic resonance for nonrotating fields. *Phys. Rev.*, 57(6):522–527, Mar 1940.

[10] I. Bloch, T.W. Hänsch, and T. Esslinger. Measurement of the spatial coherence of a trapped bose gas at the phase transition. *Science*, 403:166, 2000.

[11] N. N. Bogoliubov. On the theory of superfluidity. *J. Phys. (USSR)*, 11:23, 1947.

[12] W.L. Bragg. The diffraction of short electromagnetic waves by a crystal. *Proceedings of the Cambridge Philosophical Society*, 17:43–57, 1914.

[13] Dmitry Budker, Derek F. Kimball, and David P. DeMille. *Atomic Physics: an exploration throughproblems and solutions.* Oxford University Press, 2004.

[14] S. Burger, F. S. Cataliotti, C. Fort, F. Minardi, M. Inguscio, M. L. Chiofalo, and M. P. Tosi. Superfluid and dissipative dynamics of a bose-einstein condensate in a periodic optical potential. *Phys. Rev. Lett.*, 86(20):4447–4450, May 2001.

[15] D. A. Butts and D. S. Rokhsar. Trapped fermi gases. *Phys. Rev. A*, 55(6):4346–4350, Jun 1997.

[16] Gretchen Campbel. ^{87} *Rubidium Bose-Einstein Condensates in Optical Lattices.* PhD thesis, M.I.T., 2006.

[17] Gretchen K. Campbell, Jongchul Mun, Micah Boyd, Erik W. Streed, Wolfgang Ketterle, and David E. Pritchard. Parametric amplification of scattered atom pairs. *Phys. Rev. Lett.*, 96:020406, 2006.

[18] P. Capuzzi, P. Vignolo, F. Federici, and M. P. Tosi. Sound propagation in elongated superfluid fermionic clouds. *Phys. Rev. A*, 73:021603, 2006.

[19] J. Carlson, S.-Y. Chang, V. R. Pandharipande, and K. E. Schmidt. Superfluid fermi gases with large scattering length. *Phys. Rev. Lett.*, 91(5):050401, Jul 2003.

[20] J. Carlson and Sanjay Reddy. Asymmetric two-component fermion systems in strong coupling. *Phys. Rev. Lett.*, 95:060401, 2005.

[21] C. Chin, M. Bartenstein, A. Altmeyer, S. Riedl, S. Jochim, J. Hecker Denschlag, and R. Grimm. Observation of the pairing gap in a strongly interacting fermi gas. *Science*, 305:1128, 2004.

[22] J. K. Chin, J. M. Vogels, and W. Ketterle. Amplification of local instabilities in a bose-einstein condensate with attractive interactions. *Phys. Rev. Lett.*, 90(16):160405, Apr 2003.

[23] Jit Kee Chin. *title T.B.A.* PhD thesis, M.I.T., 2007.

[24] J.K. Chin, D.E. Miller, Y. Liu, C. Stan, W. Setiawan, C. Sanner, K. Xu, and W. Ketterle. Evidence for superfluidity of ultracold fermions in an optical lattice. *Nature*, 443:961–964, 2006.

[25] Claude Cohen-Tannoudji, Bernard Diu, and Franck Laloë. *Quantum Mechanics.* John Wiley and Sons, Inc., 1977.

[26] R. Combescot, M. Y. Kagan, and S. Stringari. Collective mode of homogeneous superfluid fermi gases in the bec-bcs crossover. *Phys. Rev. A*, 74:042717, 2006.

[27] J. Cubizolles, T. Bourdel, S. J. J. M. F. Kokkelmans, G. V. Shlyapnikov, and C. Salomon. Production of long-lived ultracold li_2 molecules from a fermi gas. *Phys. Rev. Lett.*, 91(24):240401, Dec 2003.

[28] C. A. Stan Y. Liu W. Setiawan C. Sanner D. E. Miller, J. K. Chin and W. Ketterle. Critical velocity for superfluid flow across the bec-bcs crossover. *Phys. Rev. Lett.*, 99:070402, 2007.

[29] Franco Dalfovo, Stefano Giorgini, Lev P. Pitaevskii, and Sandro Stringari. Theory of bose-einstein condensation in trapped gases. *Rev. Mod. Phys.*, 71(3):463–512, Apr 1999.

[30] C. J. Davisson and L. H. Germer. Scattering of electrons by s single crystal of nickel. *Nature*, 119:558, 1927.

[31] P. G. de Gennes. *Superconductivity of Metals and Alloys.* Addison-Wesley, 1989.

[32] L. De Sarlo, L. Fallani, J. E. Lye, M. Modugno, R. Saers, C. Fort, and M. Inguscio. Unstable regimes for a bose-einstein condensate in an optical lattice. *Phys. Rev. A*, 72(1):013603, Jul 2005.

[33] L. Deng, E. W. Hagley, J. Wen, M. Trippenbach, Y. Band, P. S. Julienne, J. E. Simsarian, K. Helmerson, S. L. Rolston, and W. D. Phillips. Four-wave mixing with matter waves. *Nature*, 398:218–220, 1999.

[34] J. Denschlag, J. E. Simsarian, D. L. Feder, Charles W. Clark, L. A. Collins, J. Cubizolles, L. Deng, E. W. Hagley, K. Helmerson, W. P. Reinhardt, S. L. Rolston, B. I. Schneider, and W. D. Phillips. Generating solitons by phase engineering of a bose-einstein condensate. *Science*, 287:97–101, 2000.

[35] Roberto B. Diener, Qi Zhou, Hui Zhai, and Tin-Lun Ho. Criterion for bosonic superfluidity in an optical lattice. *Phys. Rev. Lett.*, 98:180404, 2007.

[36] Elizabeth A. Donley, Neil R. Claussen, Sarah T. Thompson, and Carl E. Wieman. Atommolecule coherence in a boseeinstein condensate. *Nature*, 417:529, 2002.

[37] Dallin Durfee. *Dynamic Properties of Dilute Bose-Einstein Condensates.* PhD thesis, M.I.T., 1999.

[38] Stephan Dürr, Thomas Volz, Andreas Marte, and Gerhard Rempe. Observation of molecules produced from a bose-einstein condensate. *Phys. Rev. Lett.*, 92:020406, 2004.

[39] C. Fort P. Maddaloni F. Minardi A. Trombettoni A. Smerzi F. S. Cataliotti, S. Burger and M. Inguscio. Josephson junction arrays with bose-einstein condensates. *Science*, 293:843–846, 2001.

[40] Francesca Ferlaino, Chiara D'Errico, Giacomo Roati, Matteo Zaccanti, Massimo Inguscio, Giovanni Modugno, and Andrea Simoni. Feshbach spectroscopy of a k-rb atomic mixture. *Phys. Rev. A*, 73:040702, 2006.

[41] T. Frisch, Y. Pomeau, and S. Rica. Transition to dissipation in a model of superflow. *Phys. Rev. Lett.*, 69(11):1644–1647, Sep 1992.

[42] Fabrice Gerbier, Artur Widera, Simon Flling, Olaf Mandel, Tatjana Gericke, and Immanuel Bloch. Interference pattern and visibility of a mott insulator. *Phys. Rev. A*, 72:053606, 2005.

[43] Jordan M. Gerton, Dmitry Strekalov, Ionut Prodan, and Randall G. Hulet. Direct observation of growth and collapse of a boseeinstein condensate with attractive interactions. *Nature*, 408:692–695, 2000.

[44] Stefano Giorgini, Lev P. Pitaevskii, and Sandro Stringari. Theory of ultracold fermi gases. *preprint condmat/0706.3360*, 2007.

[45] M. Greiner, O. Mandel, T. Esslinger, T.W. Hnsch, and I. Bloch. Quantum phase transition from a superfluid to a mott insulator in a gas of ultracold atoms. *Nature*, 415:39–44, 2002.

[46] Markus Greiner. *Ultracold quantum gases in three-dimensional optical lattice potentials.* PhD thesis, Ludwig-Maximilians-Universität München, 2003.

[47] Markus Greiner, Cindy A. Regal, and Deborah S. Jin. Emergence of a molecular bose-einstein condensate from a fermi gas. *Nature*, 426:537, 2003.

[48] David Griffiths. *Introduction to Elementary Particles.* John Wiley and Sons, 1987.

[49] Rudolph Grimm. Ultracold fermi gases in the bec-bcs crossover: a review from the innsbruck perspective. *Proceedings of the International School of Physics Varenna*, Course CLXIV, 2006. e-print: cond-mat/0703091.

[50] S. Gupta, K. Dieckmann, Z. Hadzibabic, and D. E. Pritchard. Contrast interferometry using bose-einstein condensates to measure h/m and α. *Phys. Rev. Lett.*, 89:140401, 2002.

[51] T. L. Gustavson, P. Bouyer, and M. A. Kasevich. Precision rotation measurements with an atom interferometer gyroscope. *Phys. Rev. Lett.*, 78:2046, 1997.

[52] E.W. Hagley, L. Deng, M. Kozuma, M. Trippenbach, Y.B. Band, M. Edwards, M. Doery, P.S. Julienne, K. Helmerson, S. L. Rolston, and W.D. Phillips. Measurement of the coherence of a bose-einstein condensate. *Phys. Rev. Lett.*, 83:3115, 1999.

[53] R. Haussmann, W. Rantner, S. Cerrito, and W. Zwerger. Thermodynamics of the bcs-bec crossover. *Phys. Rev. A*, 75(2):023610, Feb 2007.

[54] Jens Herbig, Tobias Kraemer, Michael Mark, Tino Weber, Cheng Chin, Hanns-Christoph Ngerl, and Rudolf Grimm. Preparation of a pure molecular quantum gas. *Science*, 301:1510, 2003.

[55] Tin-Lun Ho. Universal thermodynamics of degenerate quantum gases in the unitarity limit. *Phys. Rev. Lett. 92*, 92:090402, 2004.

[56] W. Hofstetter, J. I. Cirac, P. Zoller, E. Demler, and M. D. Lukin. High-temperature superfluidity of fermionic atoms in optical lattices. *Phys. Rev. Lett.*, 89(22):220407, Nov 2002.

[57] Kerson Huang. *Statistical Mechanics: Second Edition.* John Wiley and Sons, 1987.

[58] Sara Ianeselli, Chiara Menotti, and Augusto Smerzi. Beyond the landau criterion for superfluidity. *J. Phys. B*, 39:S135–S142, 2006.

[59] S. Inouye, M.R. Andrews, J. Stenger, H.-J. Miesner, D.M. Stamper-Kurn, and W. Ketterle. Observation of feshbach resonances in a bose-einstein condensate. *Nature*, 392:151, 1998.

[60] S. Inouye, J. Goldwin, M. L. Olsen, C. Ticknor, J. L. Bohn, , and D. S. Jin. Observation of heteronuclear feshbach resonances in a mixture of bosons and fermions. *Phys. Rev. Lett.*, 93:183201, 2004.

[61] B. Jackson, J. F. McCann, and C. S. Adams. Vortex formation in dilute inhomogeneous bose-einstein condensates. *Phys. Rev. Lett.*, 80(18):3903–3906, May 1998.

[62] B. Jackson, J. F. McCann, and C. S. Adams. Dissipation and vortex creation in bose-einstein condensed gases. *Phys. Rev. A*, 61(5):051603, Apr 2000.

[63] S. Jochim, M. Bartenstein, A. Altmeyer, G. Hendl, C. Chin, J. Hecker Denschlag, and R. Grimm. Pure gas of optically trapped molecules created from fermionic atoms. *Phys. Rev. Lett.*, 91:240402, 2003.

[64] S. Jochim, M. Bartenstein, A. Altmeyer, G. Hendl, S. Riedl, C. Chin, J. Hecker Denschlag, and R. Grimm. Bose-einstein condensation of molecules. *Science*, 302:2101, 2003.

[65] J. Joseph, B. Clancy, L. Luo, J. Kinast, A. Turlapov, and J. E. Thomas. Measurement of sound velocity in a fermi gas near a feshbach resonance. *Phys. Rev. Lett.*, 98:170401, 2007.

[66] W Ketterle, D S Durfee, and D M Stamper-Kurn. Making, probing and understanding bose-einstein condensates. *International School of Physics Enrico Fermi, Course CXL*, 1999. cond-mat/9904034.

[67] Wolfgang Ketterle, Kendall B. Davis, Michael A. Joffe, Alex Martin, and David E. Pritchard. High densities of cold atoms in a dark spontaneous-force optical trap. *Phys. Rev. Lett.*, 70(15):2253–2256, Apr 1993.

[68] Michael Khl, Henning Moritz, Thilo Stferle, Kenneth Gnter, and Tilman Esslinger. Fermionic atoms in a three dimensional optical lattice: Observing fermi surfaces, dynamics, and interactions. *Phys. Rev. Lett.*, 94:080403, 2005.

[69] Charles Kittel. *Introduction to Solid State Physics: 7th Edition.* John Wiley and Sons, 1996.

[70] Charles Kittel and Herber Kroemer. *Thermal Physics: 2nd Edition.* W. H. Freeman and Co., 1980.

[71] S. Konabe and T. Nikuni. Instability of a superfluid bose gas induced by a locked thermal gas in an optical lattice. *J. Phys. B*, 39:S101–S108, 2005.

[72] M. Kozuma, L. Deng, E. W. Hagley, J. Wen, R. Lutwak, K. Helmerson, S. L. Rolston, and W. D. Phillips. Coherent splitting of bose-einstein condensed atoms with optically induced bragg diffraction. *Phys. Rev. Lett.*, 82(5):871–875, Feb 1999.

[73] Meret Kraemer, Chiara Menotti, Lev Pitaevskii, and Sandro Stringari. Bose-einstein condensates in 1d optical lattices: compressibility, bloch bands and elementary excitations. *Eur. Phys. J. D*, 27:247, 2003.

[74] M. Krämer, L. Pitaevskii, and S. Stringari. Macroscopic dynamics of a trapped bose-einstein condensate in the presence of 1d and 2d optical lattices. *Phys. Rev. Lett.*, 88(18):180404, Apr 2002.

[75] Alan Lenef, Troy D. Hammond, Edward T. Smith, Michael S. Chapman, Richard A. Rubenstein, and David E. Pritchard. Rotation sensing with an atom interferometer. *Phys. Rev. Lett.*, 78:760, 1997.

[76] G. Lens, P. Meystre, and E. W. Wright. Nonlinear atom optics. *Phys. Rev. Lett.*, 71:3271, 1993.

[77] T. Loftus, C. A. Regal, C. Ticknor, J. L. Bohn, and D. S. Jin. Resonant control of elastic collisions in an optically trapped fermi gas of atoms. *Phys. Rev. Lett.*, 88(17):173201, Apr 2002.

[78] M. Machholm, C. J. Pethick, and H. Smith. Band structure, elementary excitations, and stability of a bose-einstein condensate in a periodic potential. *Phys. Rev. A*, 67(5):053613, May 2003.

[79] Peter J. Mar, Bruce G. Oldaker, Andrew H. Miklich, and David E. Pritchard. Bragg scattering of atoms from a standing light wave. *Phys. Rev. Lett.*, 60(6):515–518, Feb 1988.

[80] Jerry B. Marion and Stephen T. Thornton. *Classical Dynamics of Particles and Systems : 4th Edition.* Harcourt Brace and Company, 1995.

[81] C. Menotti, P. Pedri, and S. Stringari. Expansion of an interacting fermi gas. *Phys. Rev. Lett.*, 89(25):250402, Dec 2002.

[82] Harold J. Metcalf and Peter van der Straten. *Laser Coolin and Trapping.* Springer, 1999.

[83] D. E. Miller, J. R. Anglin, J. R. Abo-Shaeer, K. Xu, J. K. Chin, and W. Ketterle. High-contrast interference in a thermal cloud of atoms. *Phys. Rev. A*, 71:043615, 2005.

[84] S. A. Morgan, S. Choi, and K. Burnett. Nonlinear mixing of quasiparticles in an inhomogeneous bose condensate. *Phys. Rev. A*, 57:3818, 1998.

[85] Oliver Morsch and Markus Oberthaler. Dynamics of bose-einstein condensates in optical lattices. *Rev. Mod. Phys.*, 78:179, 2006.

[86] Jongchul Mun, Patrick Medley, Gretchen K. Campbell, Luis G. Marcassa, David E. Pritchard, and Wolfgang Ketterle. Phase diagram for a bose-einstein condensate moving in an optical lattice. *preprint condmat/0706.3946*, 2007.

[87] M. Naraschewski, H. Wallis, A. Schenzle, J. I. Cirac, and P. Zoller. Interference of bose condensates. *Phys. Rev. A*, 54:2185, 1996.

[88] John W. Negele and Henri Orland. *Quantum Many-Particle Systems.* Addison-Weseley, 1988.

[89] R. Onofrio, C. Raman, J. M. Vogels, J. R. Abo-Shaeer, A. P. Chikkatur, and W. Ketterle. Observation of superfluid flow in a bose-einstein condensed gas. *Phys. Rev. Lett.*, 85(11):2228–2231, Sep 2000.

[90] ACHIM Peters, KENG YEOW Chung, and STEVEN Chu. Measurement of gravitational acceleration by dropping atoms. *Nature*, 400:849, 1999.

[91] C. J. Pethick and H. Smith. *Bose-Einstein Condensation in Dilute Gases.* Cambridge University Press, 2002.

[92] C. Raman, M. Köhl, R. Onofrio, D. S. Durfee, C. E. Kuklewicz, Z. Hadzibabic, and W. Ketterle. Evidence for a critical velocity in a bose-einstein condensed gas. *Phys. Rev. Lett.*, 83(13):2502–2505, Sep 1999.

[93] C. Raman, R. Onofrio, J.M. Vogels, J.R. Abo-Shaeer, and W. Ketterle. Dissipationless flow and superfluidity in gaseous bose-einstein condensates. *J. Low Temp. Phys.*, 122:99–116, 2001.

[94] C. A. Regal, C. Ticknor, J. L. Bohn, and D. S. Jin. Tuning p-wave interactions in an ultracold fermi gas of atoms. *Phys. Rev. Lett.*, 90(5):053201, Feb 2003.

[95] Cindy A. Regal, Christopher Ticknor, John L. Bohn, and Deborah S. Jin. Creation of ultracold molecules from a fermi gas of atoms. *Nature*, 424:47, 2003.

[96] F. Reif. *Fundamentals of Statistical and Thermal Physics.* McGraw Hill, 1965.

[97] G. Roati, E. de Mirandes, F. Ferlaino, H. Ott, G. Modugno, and M. Inguscio. Atom interferometry with trapped fermi gases. *Phys. Rev. Lett.*, 92:230402, 2004.

[98] T. Rom, T. Best, D. van Oosten, U. Schneider, S. Flling, B. Paredes, and I. Bloch. Free fermion antibunching in a degenerate atomic fermi gas released from an optical lattice. *Nature*, 444:733, 2006.

[99] J. J. Sakurai. *Modern Quantum Mechanics.* Addison Wesely, 1994.

[100] C.H. Schunck, M.W. Zwierlein, C.A. Stan, S.M.F. Raupach, W. Ketterle, A. Simoni, E. Tiesinga, C.J. Williams, and P.S. Julienne. Feshbach resonances in fermionic ^{6}li. *Phys. Rev. A*, 71:045601, 2005.

[101] Widagdo Setiawan. *A New Degenerate Fermi Gas Apparatus.* M.I.T. Undergraduate Thesis, 2007.

[102] Y. Shin, M. W. Zwierlein, C. H. Schunck, A. Schirotzek, and W. Ketterle. Observation of phase separation in a strongly-interacting imbalanced fermi gas. *Phys. Rev. Lett.*, 97:030401, 2006.

[103] Andrea Spuntarelli, P Pieri, and G C Strinati. The josephson effect in the bcs-bec crossover. *pre-print /condmat/0705.2658*, 2007.

[104] C.A. Stan, M.W. Zwierlein, C.H. Schunck, S.M.F. Raupach, and W. Ketterle. Observation of feshbach resonances between two different atomic species. *Phys. Rev. Lett.*, 93:143001, 2004.

[105] Claudiu A. Stan. *Experiments with Interacting Bose and Fermi Gases.* PhD thesis, M.I.T., 2005.

[106] J. Stenger, S. Inouye, M. R. Andrews, H.-J. Miesner, D. M. Stamper-Kurn, and W. Ketterle. Strongly enhanced inelastic collisions in a bose-einstein condensate near feshbach resonances. *Phys. Rev. Lett.*, 82(12):2422–2425, Mar 1999.

[107] J. Stenger, S. Inouye, A. P. Chikkatur, D. M. Stamper-Kurn, D. E. Pritchard, and W. Ketterle. Bragg spectroscopy of a bose-einstein condensate. *Phys. Rev. Lett.*, 82(23):4569–4573, Jun 1999.

[108] Kevin E. Strecker, Guthrie B. Partridge, and Randall G. Hulet. Conversion of an atomic fermi gas to a long-lived molecular bose gas. *Phys. Rev. Lett.*, 91(8):080406, Aug 2003.

[109] S. Stringari. Collective excitations of a trapped bose-condensed gas. *Phys. Rev. Lett.*, 77(12):2360–2363, Sep 1996.

[110] Gregor Thalhammer, Matthias Theis, Klaus Winkler, Rudolf Grimm, and Johannes Hecker Denschlag. Inducing an optical feshbach resonance via stimulated raman coupling. *Phys. Rev. A*, 71:033403, 2005.

[111] F. Werner, O. Parcollet, A. Georges, and S. R. Hassan. Interaction-induced adiabatic cooling and antiferromagnetism of cold fermions in optical lattices. *Phys. Rev. Lett.*, 95:056401, 2005.

[112] Biao Wu and Qian Niu. Landau and dynamical instabilities of the superflow of bose-einstein condensates in optical lattices. *Phys. Rev. A*, 64(6):061603, Nov 2001.

[113] Biao Wu and Qian Niu. Superfluidity of boseeinstein condensate in an optical lattice: Landauzener tunnelling and dynamical instability. *New J. Phys.*, 5:104, 2003.

[114] K. Xu, Y. Liu, J. R. Abo-Shaeer, T. Mukaiyama, J. K. Chin, D. E. Miller, W. Ketterle, Kevin M. Jones, and Eite Tiesinga. Sodium bose-einstein condensates in an optical lattice. *Phys. Rev. A*, 72:043604, 2005.

[115] K. Xu, Y. Liu, D. E. Miller, J. K. Chin, W. Setiawan, and W. Ketterle. Observation of strong quantum depletion in a gaseous bose-einstein condensate. *Phys. Rev. Lett.*, 96:180405, 2006.

[116] K. Xu, T. Mukaiyama, J. R. Abo-Shaeer, J. K. Chin, D. E. Miller, and W. Ketterle. Formation of quantum-degenerate sodium molecules. *Phys. Rev. Lett.*, 91(21):210402, Nov 2003.

[117] Kaiwen Xu. *Effects of Interaction in Bose-Einstein Condensates.* PhD thesis, M.I.T., 2006.

[118] Alexander M. Zagoskin. *Quantum Theory of Many-Body Systems.* Springer, 1998.

[119] Hui Zhai and Tin-Lun Ho. Superfluid-insulator transition of strongly interacting fermi gases in optical lattices. *preprint condmat/0704.2957*, 2007.

[120] M. W. Zwierlein, C. A. Stan, C. H. Schunck, S. M. F. Raupach, S. Gupta, Z. Hadzibabic, and W. Ketterle. Observation of bose-einstein condensation of molecules. *Phys. Rev. Lett.*, 91(25):250401, Dec 2003.

[121] Martin Zwierlein. *High-Temperature Superfluidity in an Ultracold Fermi Gas.* PhD thesis, M.I.T., 2006.

[122] Martin W. Zwierlein, Zoran Hadzibabic, Subhadeep Gupta, and Wolfgang Ketterle. Spectroscopic insensitivity to cold collisions in a two-state mixture of fermions. *Phys. Rev. Lett.*, 91(25):250404, Dec 2003.